

# Optical Frequency Standard with a Single $^{171}\text{Yb}^+$ Ion

Von der  
Fakultät für Mathematik und Physik  
der Universität Hannover

zur Erlangung des Grades  
Doktor der Naturwissenschaften  
Dr. rer. nat.  
genehmigte Dissertation

von

Dipl.-Phys. Tobias Schneider

geboren am 5. September 1975 in München

(2005)

Referent: Dr. Ekkehard Peik

Korreferent: Prof. Dr. Wolfgang Ertmer

Tag der Promotion: 22.7.2005

For my parents

Sieglinde and Jakob



# Zusammenfassung

Mit der Entwicklung atomarer Frequenznormale wurden Frequenzen und Zeitdifferenzen zu den derzeit am genauesten messbaren physikalischen Grössen. Eine der vielversprechendsten Entwicklungen auf dem Weg zu immer genaueren Frequenznormalen basiert auf der Nutzung schmaler optischer Übergänge in laser-gekühlten und in elektrischen Hochfrequenzfallen gespeicherten Ionen als Frequenzreferenzen. Diese optischen Einzelionenfrequenznormale haben das Potential geringere Instabilitäten und systematische Unsicherheiten zu erreichen als die derzeit besten verfügbaren Mikrowellennormale.

Als möglicher Kandidat für ein solches optischen Frequenznormal wurde im Rahmen dieser Arbeit der  $^2S_{1/2}(F=0, m_F=0) \rightarrow ^2D_{3/2}(F=2, m_F=0)$  elektrische Quadrupolübergang in einem einzelnen, in einer Paul Falle gespeicherten, laser-gekühlten  $^{171}\text{Yb}^+$  Ion untersucht. Frequenzvergleiche zwischen zwei dieser Normale werden verwendet, um die Instabilitätseigenschaften und die systematischen Unsicherheiten des Frequenznormals zu untersuchen. Zu diesem Zweck wurde zusätzlich zu einem bereits existierenden Ionenfallensystem ein weiteres aufgebaut.

Eine Instabilität in Form einer Allan Standardabweichung von  $\sigma_y(t) \simeq 1.1 \cdot 10^{-14} t^{-\frac{1}{2}}$  der Frequenzdifferenz zwischen den beiden Frequenznormalen konnte demonstriert werden. Die gemessene Instabilität ist nahe an der Stabilitätsgrenze, die sich aus numerischen Simulationen ergibt, die als einzige Rauschquelle das Quantenprojektionsrauschen enthalten. Die mittlere relative Frequenzdifferenz zwischen den beiden Frequenznormalen von  $3.8(6.1) \cdot 10^{-16}$  ist vergleichbar mit den besten Ergebnissen, die bisher mit Cäsium Fontänen Uhren erreicht wurden.

Zwei systematische Effekte, der quadratische Stark Effekt und die Quadrupolverschiebung, wurden im Detail untersucht und die zugehörigen atomaren Parameter wurden erstmals experimentell bestimmt. Für den quadratischen Stark Effekts wurden die Werte der statischen atomaren elektrischen Skalar- und Tensorpolarisierbarkeiten  $\Delta\alpha_S = -6.9(1.4) \cdot 10^{-40} \text{ Jm}^2/\text{V}^2$  und  $\alpha_T(D_{3/2}) = -13.6(2.2) \cdot 10^{-40} \text{ Jm}^2/\text{V}^2$  gemessen. Der Wert des Quadrupolmoments  $\Theta(D_{3/2}) = 9.32(48) \cdot 10^{-40} \text{ Cm}^2$  des  $^2D_{3/2}$  Zustands wurde bestimmt, in guter Übereinstimmung mit theoretischen Berechnungen.

Aus Abschätzungen für alle bekannten systematischen Unsicherheiten des Frequenznormals ergibt sich für den gegenwärtigen Stand des Experimentes eine relative systematische Unsicherheit von  $1.0 \cdot 10^{-15}$ . Es werden experimentelle Methoden vorgestellt, die es ermöglichen werden die relative Unsicherheit im Lauf der nächsten Jahre bis in den  $10^{-17}$  Bereich zu reduzieren.

**Stichworte:** Optische Frequenznormale, Einzelionen, Ytterbium

# Abstract

With the development of atomic frequency standards, frequencies and time intervals became the physical quantities that can be measured with the highest precision. One of the most promising developments in the ongoing research for ever more accurate frequency standards are frequency standards based on narrow optical transitions in laser-cooled ions stored in radio-frequency traps. These single-ion optical frequency standards have the potential to reach instabilities and systematic uncertainties beyond the capabilities of the best microwave standards available at present.

In this work, the  ${}^2S_{1/2}(F = 0, m_F = 0) \rightarrow {}^2D_{3/2}(F = 2, m_F = 0)$  electric quadrupole transition in a single  ${}^{171}\text{Yb}^+$  laser cooled ion stored in a radio frequency Paul trap is investigated as a candidate for such an optical frequency standard. Frequency comparisons between two such frequency standards were used as a method to investigate the instability properties and systematic uncertainties of the frequency standard. For this purpose a new ion trap system was set up in addition to an existing one.

An instability measured by an Allan deviation of  $\sigma_y(t) \simeq 1.1 \cdot 10^{-14} t^{-\frac{1}{2}}$  of the frequency difference between the two standards was demonstrated. This is close to the stability limit derived from numerical simulations that include quantum projection noise as the only source of noise. A mean relative frequency difference between the two frequency standards of  $3.8(6.1) \cdot 10^{-16}$  was found, which is comparable to the best result achieved with cesium fountain clocks.

Two systematic effects, the quadratic Stark effect and the quadrupole shift, were studied in detail and the relevant atomic parameters were measured for the first time. For the quadratic Stark effect, the relevant static atomic scalar- and tensor electric polarizabilities were measured to be  $\Delta\alpha_S = -6.9(1.4) \cdot 10^{-40} \text{ Jm}^2/\text{V}^2$  and  $\alpha_T(D_{3/2}) = -13.6(2.2) \cdot 10^{-40} \text{ Jm}^2/\text{V}^2$  respectively. The quadrupole moment of the  ${}^2D_{3/2}$  state was determined to be  $\Theta(D_{3/2}) = 9.32(48) \cdot 10^{-40} \text{ Cm}^2$ , which is in good agreement with theoretical calculations.

Estimates for all known systematic uncertainties of the frequency standard were derived leading to a total systematic relative uncertainty of  $1.0 \cdot 10^{-15}$  for the present state of the experiment. Experimental strategies are discussed that will allow to improve the relative uncertainty to a few parts in  $10^{17}$  over the next years.

**Keywords:** Optical frequency standards, single ion, ytterbium

# Contents

<b>Abstract</b>	<b>ii</b>
<b>1 Introduction</b>	<b>1</b>
<b>2 Frequency Standards</b>	<b>5</b>
2.1 Instability, Reproducibility and Accuracy . . . . .	5
2.2 Concepts for Optical Frequency Standards . . . . .	8
2.3 Absolute Frequency Measurement . . . . .	10
<b>3 Trapping and Cooling of a Single <math>^{171}\text{Yb}^+</math> Ion</b>	<b>12</b>
3.1 The Paul Trap . . . . .	12
3.2 Level Structure of $^{171}\text{Yb}^+$ . . . . .	14
3.3 Laser Cooling of $^{171}\text{Yb}^+$ . . . . .	17
3.4 Compensation of the Electric Stray Field . . . . .	22
<b>4 Experimental Setup</b>	<b>25</b>
4.1 The Traps . . . . .	25
4.2 Lasers . . . . .	28
4.2.1 Cooling Laser . . . . .	29
4.2.2 Repumper Lasers . . . . .	29
4.2.3 Probe Laser . . . . .	30
4.3 Fluorescence Detection . . . . .	31

<b>5</b>	<b>Interrogation of the 436 nm Reference Transition</b>	<b>32</b>
5.1	Interrogation Sequence . . . . .	32
5.2	Quantum Projection Noise . . . . .	34
5.3	Spectra . . . . .	35
5.3.1	Secular and Micromotion Sidebands . . . . .	35
5.3.2	Zeeman Structure . . . . .	37
5.3.3	$\Delta m_F = 0$ Clock Transition . . . . .	39
5.4	Laser Frequency Lock . . . . .	40
5.5	Frequency Comparisons Between Two Trap Systems . . . . .	44
<b>6</b>	<b>Instability of the <math>^{171}\text{Yb}^+</math> Single-Ion Frequency Standard</b>	<b>46</b>
6.1	Theory . . . . .	46
6.2	Comparison with the Experiment . . . . .	48
6.3	Dick Effect . . . . .	51
<b>7</b>	<b>Systematic Frequency Shifts</b>	<b>52</b>
7.1	Doppler Effect . . . . .	52
7.2	Zeeman Effect . . . . .	53
7.3	Quadratic Stark Effect . . . . .	56
7.3.1	Measurement of the Scalar and Tensor Electric Polarizabilities . . . . .	57
7.3.2	Blackbody AC Stark Shift . . . . .	58
7.3.3	Light Shift . . . . .	60
7.4	Quadrupole Shift . . . . .	61
7.4.1	Measurement of the Quadrupole Moment of the $^2D_{3/2}$ State	63
7.4.2	Estimate for the Gradient of the Electric Stray Field . . .	65
7.4.3	Methods for Reducing the Quadrupole Shift . . . . .	66
7.5	Gravitational Time Dilation . . . . .	70
7.6	Collision Effects . . . . .	70
7.7	Cavity QED Effects . . . . .	71
7.8	Line Profile Asymmetry . . . . .	72
7.9	Uncertainty Budget . . . . .	73



---

8 Agreement Between the Two Trap Systems	77
9 Outlook	80
A Calculation of the Quadratic Stark Shift	83
B Calculation of the Quadrupole Shift	86
Bibliography	89
Acknowledgements	98
List of Publications	99
Curriculum Vitae	100



# Chapter 1

## Introduction

*Time is the moving imago of the unmoving eternity.*

- Plato [1]

*Time is what one reads off the clock.*

- A. Einstein [2]

*Time is an illusion. Lunchtime doubly so.*

- D. N. Adams [3]

The notion of time is one of the most important concepts in the history of mankind and science, yet to date no generally accepted physical theory or philosophical concept about the true nature of time has been put forth. This discrepancy between the familiar notion of time and the understanding of its deeper meaning is summarized in a famous dictum of the philosopher Augustinus [4]: “*What is time? As long as no one asks me I know it, but if someone asks me to explain it, I do not know it*”. Nevertheless remarkable success was achieved in the measurement of time defined in an operational sense as it is expressed by A. Einstein’s dictum quoted above. Among all physical quantities time intervals and frequencies are at present the ones that can be measured with the highest precision and with the assignment of a fixed value for the speed of light in vacuum in the SI system of units, also length measurements became essentially time measurements. From the calendar and the watch over high speed data transfer and satellite navigation systems to tests of fundamental physical theories like relativity [5–10], quantum electrodynamics [11] and the search for time variations of fundamental constants [12–14], time and frequency measurements are ubiquitous.

At the heart of any time measuring device is a stable periodic process whose cycles are counted. Historically, the rotations of celestial bodies provided the most stable clocks, and still, the rotation of the earth determines our everyday feeling

of time. The first man-made clocks that were superior to the astronomical ones were the quartz clocks invented around 1930 [15–17], but the greatest progress in accuracy came from the use of atomic resonance frequencies. The concept of an atomic clock was envisioned already by J. C. Maxwell in 1870 when he stated [18]: “*If, then, we wish to obtain standards of length, time, and mass which shall be absolutely permanent, we must seek them not in the dimensions, or the motion, or the mass of our planet, but in the wavelength, the period of vibration, and the absolute mass of these imperishable and unalterable and perfectly similar molecules*”. This idea found its realization in 1967, when the 13th General Conference on Weights and Measures led to the following definition of the SI second: “*The second is the duration of 9 192 631 770 periods of the radiation corresponding to the transition between the two hyperfine levels of the ground state of the caesium 133 atom*” [19]. Today cesium fountain clocks realize the second with relative uncertainties below  $10^{-15}$  [20, 21]. Further improvements are expected from the use of optical instead of microwave atomic transitions as frequency references because of the approximately  $10^5$  times higher frequencies.

Over the last decades techniques were developed that allow to confine and detect a single ion in a radiofrequency trap [22–26] and reduce its kinetic energy by laser cooling [27, 28]. The high level of control that can be achieved in such ion trap experiments has made them an important tool for experiments in many fields of fundamental as well as applied physics including mass spectrometry (their first application) [29], quantum computation [30–33], and quantum teleportation [34, 35].

With the development of frequency-stable tunable laser sources it became possible to investigate forbidden optical transitions in single ions as candidates for optical frequency standards, which was proposed first by H. Dehmelt [36]. Because a single particle at rest which is isolated from the environment is one of the most simple and well controlled physical systems, single-ion optical frequency standards are ultimately expected to reach relative uncertainties in the range of  $10^{-18}$  [24]. Several other concepts for optical frequency standards are currently investigated [37, 38], but the single ion standards are expected to eventually achieve the lowest uncertainties. With the development of femtosecond frequency combs [39, 40] as clockworks that can relate the frequency of an optical standard to any other frequency in the optical or microwave region with high precision, all the necessary experimental tools for an optical clock are now available. Several transitions in different ions have been investigated so far as candidates for an optical frequency standard [41–46] and relative uncertainty of a few parts in  $10^{15}$  recently have been demonstrated in frequency measurements relative to cesium fountain clocks of reference transitions in  $^{88}\text{Sr}^+$  [47] and  $^{199}\text{Hg}^+$  [48]. Similar measurements of optical transition frequencies in  $^{199}\text{Hg}^+$  [41, 49, 50],  $^{171}\text{Yb}^+$  [51, 52], and hydrogen [53] have been used recently to derive the so far most stringent limit on the present temporal variation of the fine structure constant [54], demonstrating the

potential of optical frequency standards.

In order to characterize the performance of a frequency standard it has to be compared to another frequency standard with an equal or better performance. Studies of the systematic frequency shifts of an optical frequency standard by measurements of its frequency relative to established microwave standards are inherently limited by the instabilities and uncertainties of the latter. These limitations can be overcome by comparing the optical frequency standard with a second one as is demonstrated in this work by comparing two single-ion frequency standards based on the  $^2S_{1/2}(F = 0, m_F = 0) \rightarrow ^2D_{3/2}(F = 2, m_F = 0)$  transition in  $^{171}\text{Yb}^+$ .

The outline of this thesis is the following:

Chapter 2 introduces the basic terminology and concepts used in the context of optical frequency standards and relates the single ion optical frequency standard to other concepts for optical frequency standards investigated at present by various research groups.

In Chapter 3 a short introduction is given to the atomic properties of  $^{171}\text{Yb}^+$  and the experimental techniques used to localize the ion in a Paul trap and to cool it. A good compensation of electric stray fields at the position of the ion is important to achieve low temperatures of the ion and to avoid systematic frequency shifts by the second order Doppler and the second order Stark effect. Section 3.4 therefore gives a detailed description of the method for the compensation of electric stray fields used in the experiment.

The important components of the experimental setup and the experimental realization of the methods discussed in Chapter 3 are described in Chapter 4.

The experimental scheme used for the spectroscopy of the  $^2S_{1/2}(F = 0) \rightarrow ^2D_{3/2}(F = 2)$  transition, its limitations and the information that can be gained from the various types of excitation spectra is the subject of Chapter 5. The last two sections contain a description of the methods used to stabilize the probe laser frequency to the atomic resonance and to compare the two ytterbium frequency standards.

One of the important figures of merit for a frequency standard is its instability. Chapter 6 discusses the theory of the instability of a single ion frequency standards and presents a comparison of numerical simulations with the experimental results of frequency comparisons between the two trap systems.

Chapter 7 presents estimates for all known relevant systematic frequency uncertainties of the  $^{171}\text{Yb}^+$  standard with an emphasis on the quadratic Stark and quadrupole shift which are the two most important systematics and which were investigated experimentally in detail.

Finally, in Chapter 8 an experiment is described that demonstrates an agreement between the two frequency standards which is already comparable to the one found in similar experiments with cesium fountain clocks.

# Chapter 2

## Frequency Standards

At the heart of any frequency standard is a stable periodic process whose frequency can be compared to other frequencies. The basic concept of a time measurement is to count the number of cycles of the stable periodic process that occur between two events whose time separation shall be measured. If the frequency of the process is determined not by the properties or interactions of macroscopic objects but solely by fundamental laws of physics, then according to Einstein's equivalence principle this frequency should be the same at any time or place and thus realize an ideal frequency standard. A good approximation to this ideal is the frequency  $\omega$  associated with the discrete energy difference  $\Delta E = \hbar\omega$  between two states of an atom. The most prominent example of such an atomic frequency standard is the frequency of the transition between the two hyperfine levels of the ground state in  $^{133}\text{Cs}$  which was used in 1967 for the definition of the SI second.

Most atomic frequency standards used today are operated as passive standards that do not produce the frequency output themselves but act as a reference for the stabilization of a local oscillator which, depending on the atomic transition frequency is typically a microwave source or a laser.

A detailed description of the various types of atomic frequency standards, their physics and their many applications can be found in [10, 37, 55–57], while a comprehensive overview over the long history of time measurement and time scales is given for example in [58–60]. The following sections will introduce the terminology and concepts used in the context of frequency standards.

### 2.1 Instability, Reproducibility and Accuracy

The three terms that are used to characterize the performance of a (frequency) standard are instability, reproducibility and accuracy.

Table 2.1: Basic noise types in time and frequency measurements

Noise type	Frequency dependence of the power spectral density
White phase noise	$f^2$
Flicker phase noise	$f$
White frequency noise	constant
Flicker frequency noise	$f^{-1}$
Random walk of frequency	$f^{-2}$

The instability is a measure of the confidence that one can have in the result of a (frequency) measurement with respect to the reference in the presence of random noise and is usually given by the “width” of the distribution of the results of a large number of measurements. Since in principle every observation of a physical process leads to noise in the observed quantity and most quantum processes are intrinsically probabilistic, the instability of a standard will always be limited at some level by noise. Contributions to the noise which are not random or have a nonzero mean value are usually accounted for in the accuracy and are not considered for the determination of the instability. Table 2.1 lists the five basic noise types and the frequency dependence of their power spectral density.

Information about the instability of a frequency standard can be obtained only from a series of successive measurements and the instability is thus often described as the statistical uncertainty of the frequency averaged over a given number of measurements. The most common time-domain measure for the instability of a frequency standard is the Allan variance [61, 62]. For a set of  $N$  frequency values averaged over a time  $t$  that are obtained from a total of  $M$  elementary measurements of duration  $t_0$  the Allan variance can be written as [10, 62]

$$\sigma_y^2(t) = \frac{1}{2(N-1)} \sum_{n=1}^{N-1} (y_{n+1}(t) - y_n(t))^2, \quad (2.1)$$

where  $y_n(t)$  is the  $n^{\text{th}}$  frequency average over the time  $t = Mt_0/N$  divided by the nominal frequency. Usually the instability is given as the Allan deviation  $\sigma_y(t)$ . The Allan variance coincides with the ordinary variance for white frequency noise. For divergent noise types like for example flicker frequency noise it has the advantage that it converges to a value that does not depend on the number of samples  $N$ , which is not always the case for the ordinary variance. If one of the noise contributions listed in Table 2.1 is dominant over a large enough range of averaging times  $t$ , the type of noise can be determined from the slope of the Allan deviation as is shown in Fig. 2.1. Aside from possibly avoidable technical sources of noise associated with the apparatus realizing an atomic frequency standard,



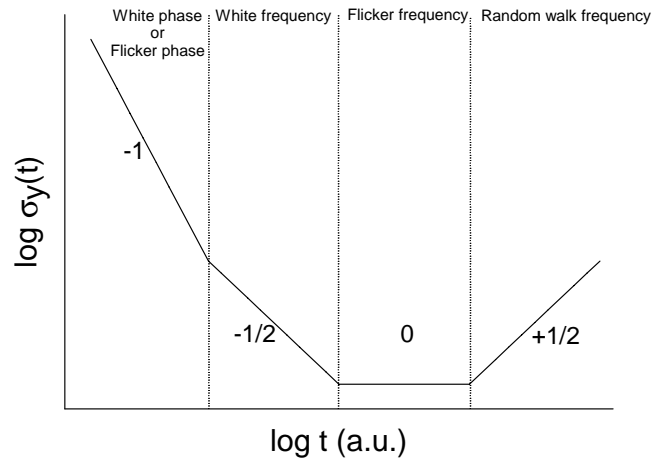


Figure 2.1: Allan deviation as a function of the averaging time  $t$  for the five basic noise types. The numbers are the slope of the Allan deviation for the given noise type.

there is also noise associated with the interrogation of the atom(s) that is inherent to the quantum mechanical nature of the measurement process. This so-called quantum projection noise will be discussed in more detail in Sec. 5.2. Here it is only important that it corresponds to white frequency noise and thus the Allan deviation of an atomic frequency standard is expected to decrease as  $t^{-\frac{1}{2}}$  for long averaging times  $t$ . For a frequency standard which uses an ensemble of  $m$  indistinguishable and independent atoms that are interrogated simultaneously, it follows from the equivalence between time and ensemble average that the effective averaging time is  $t' = mt$  and the instability decreases therefore as  $m^{-\frac{1}{2}}$  with the number of atoms. This is equivalent to stating that the signal-to-noise ratio of a single measurement of time  $t$  increases as  $m^{\frac{1}{2}}$ .

The reproducibility of a frequency standard is a measure of how well two realizations of the same frequency standard agree with each other. The reproducibility can be regarded as a measure of the control over the measurement procedure and the apparatus realizing the standard. The reproducibility is limited by the instability of the standard for the employed measurement time.

The accuracy is an estimate of the difference between a measured value and the true value of the quantity that was measured. In most cases the true value of the measured quantity, like an unperturbed atomic transition frequency, can not be known and the accuracy is therefore more a qualitative than a quantitative concept that represents a best estimate for the relation between the measured and the true value. As in the case of the reproducibility, the accuracy that can be achieved for a given measurement time is limited by the instability of the standard. A low instability is therefore required for an accurate standard.

The concepts of instability and accuracy are often combined in the term “uncertainty”. The uncertainty of the frequency standard characterizes the dispersion of the frequency values that could reasonably be expected in measurements. The uncertainty is usually divided into two parts. The systematic uncertainty contains the estimates on all effects that lead to a difference between the frequency realized by the standard and the true frequency even in the case of negligible instability. The statistical uncertainty is the minimum instability that is achieved by the standard.

## 2.2 Concepts for Optical Frequency Standards

The most accurate frequency standards available at present are cesium fountain standards based on the microwave transition near 9.2 GHz between the two hyperfine levels of the ground state in  $^{133}\text{Cs}$ . Instabilities  $\sigma_y = 1.6 \cdot 10^{-14} t^{-\frac{1}{2}}$  and relative uncertainties of  $7 \cdot 10^{-16}$  have been demonstrated in comparisons between cesium fountain standards [21]. A way to even lower relative instabilities and relative uncertainties are frequency standards that use optical transitions in atoms as frequency references, because of the approximately  $10^5$  times higher transition frequencies. Several concepts for optical frequency standards were proposed [37,38]. The three most promising concepts investigated at present are single ions stored in radio frequency traps, free falling neutral atom ensembles prepared in magneto optical traps and neutral atoms stored in optical lattices.

A single two-level atom at rest which is isolated from the environment is one of the most simple quantum mechanical systems that can be imagined. The frequency corresponding to the energy difference between the two levels will be determined solely by the fundamental interactions between the constituents of the atom and might therefore be the ideal reference for a frequency standard. In fact, the whole concept of atomic frequency standards is motivated by this idealized picture. The closest approximation to this ideal of an isolated two level system that has been realized so far is a single laser cooled ion stored in a radio frequency trap. Because of its good localization it can be treated as a point-like particle in the interaction with the local oscillator and the interaction time can in principle be arbitrarily long. According to the Fourier relation between the time and the frequency domain, a long interaction time corresponds to a high frequency resolution which allows to achieve a low instability for the frequency standard. With respect to accuracy, a single ion has the advantage of being a well-controlled and conceptually simple system. It is therefore expected that relative uncertainties of  $10^{-18}$  can be achieved with optical single-ion frequency standards [24]. The drawback of using a single particle is that the signal-to-noise ratio of the interrogation will be much smaller than for an ensemble of atoms. Nevertheless the instability that can be achieved for an optical single-ion

frequency standard is a few parts in  $10^{15} t^{-\frac{1}{2}}$ , which is still superior compared to microwave standards like the cesium clock because of the much higher transition frequency. Aside from the  $^2S_{1/2}(F=0) \rightarrow ^2D_{3/2}(F=2)$  transition in  $^{171}\text{Yb}^+$  [45, 51, 63] which is investigated in this work also other transitions in  $^{171}\text{Yb}^+$  [44],  $^{199}\text{Hg}^+$  [49, 64, 65],  $^{88}\text{Sr}^+$  [46, 47],  $^{115}\text{In}^+$  [42],  $^{138}\text{Ba}^+$  [66–68],  $^{40}\text{Ca}^+$  [69, 70], and  $^{27}\text{Al}^+$  [71] are investigated at present.

The problem of the low signal-to-noise ratio of single-ion standards can be overcome by using a large ensemble of atoms. Ions are not well suited for this purpose because of their strong mutual Coulomb interactions that would give rise to large systematic uncertainties. Instead, as in the case of cesium fountain clocks, ensembles of about  $10^7$  neutral atoms are prepared and laser cooled in a magneto-optical trap (MOT). Because the interactions of the atoms with the MOT will disturb the interrogation of the atoms by the local oscillator, the MOT has to be switched off before the interrogation. Due to the finite temperature of the ensemble and the influence of gravity, the atoms will leave the interrogation zone in a finite time which sets a limit for the interrogation time. Concerning the uncertainty, ensembles of atoms have the disadvantage that they are always extended systems with internal interactions like collisions between atoms. It will therefore be much more difficult to obtain the same level of control over the system as for single ions and thus to obtain a similarly low systematic uncertainty. It is therefore expected that ensembles of neutral atoms will be the basis for frequency standards with supreme stabilities of only a few parts in  $10^{17} t^{-\frac{1}{2}}$ , while single ions will probably achieve the lowest systematic uncertainties. Optical transitions in neutral atoms are presently investigated for  $^{40}\text{Ca}$  [72, 73],  $^{24}\text{Mg}$  [74] and hydrogen [49, 53].

In 2001, H. Katori proposed a concept for an optical frequency standard which he named “optical lattice clock”. It has the potential to combine the advantages of single-ion and neutral-atom optical frequency standards [75, 76]. The idea is that a large number of neutral atoms stored in an optical lattice at an average atom density of less than one atom per lattice site is in principle similar to a large ensemble of traps for single ions concentrated in a very small volume. The main problem is that the dipole forces associated with the lattice lead to large systematic shifts of the energy levels of the atoms by the Stark effect. However, it can be shown that for a specific wavelength of the laser generating the lattice, the energy shifts of two states can be exactly the same and the frequency corresponding to their energy difference is therefore not affected by the presence of the lattice. The system described in the proposal by Katori is the  $^1S_0 \rightarrow ^3P_0$  transition in  $^{87}\text{Sr}$  which is currently investigated by several groups [77–81]. Also experiments with the equivalent transition in neutral ytterbium are being developed [82].

Another interesting new development is the idea to use an optical nuclear transition in  $^{229}\text{Th}$  at an energy of about 3.5(1.0) eV [83] as a frequency reference [84].

Because it is a nuclear transition several systematic effects that will limit the uncertainty of single-ion standards are expected to be much reduced [84]. So far no direct observation of the transition could be demonstrated in a number of experiments [85–88]. Investigations in this direction were recently started in the time and frequency department at PTB.

## 2.3 Absolute Frequency Measurement

One of the reasons why the first atomic frequency standards were based on microwave transitions is that the local oscillator frequency can be generated and processed electronically. The direct counting of the cycles of an optical frequency with electronic equipment is not possible. This made it difficult to measure the absolute value of optical frequencies with respect to the cesium standard defining the SI second and limited the applicability of optical frequency standards for a long time. The first absolute measurements of optical frequencies required huge and complicated frequency chains that related the microwave frequency of a cesium standard to the optical frequencies [89,90]. Also for the direct comparison of two optical frequencies with relative uncertainties in the range of  $10^{-15}$ , new measurement techniques were needed because the best interferometric wavelength comparisons have relative uncertainties of about  $10^{-11}$ . The situation changed around 1999 with the advent of the so-called femtosecond laser frequency combs [39,40]: A train of phase coherent laser pulses in the time domain corresponds in the frequency domain to a spectrum of equidistant narrow resonances that are spaced at the pulse repetition frequency, while the total frequency width of the spectrum is given by the inverse length of a single pulse. The frequency of the  $n^{\text{th}}$  comb mode can be written as  $f_n = f_{\text{ceo}} + n f_{\text{rep}}$ , where  $n$  is an integer number and  $f_{\text{rep}}$  is the pulse repetition rate which can easily be measured with a fast photodiode. Due to dispersion effects, the frequency origin of the comb at  $n = 0$  is shifted from zero frequency by the so called carrier envelope offset (ceo) frequency  $f_{\text{ceo}} < f_{\text{rep}}$ . If the comb spectrum spans one octave that contains frequencies  $f_n$  as well as  $f_{2n}$  the ceo frequency can be determined in the following way: The frequency  $f_n$  is frequency doubled and compared with the frequency  $f_{2n}$  from the other side of the comb spectrum. The frequency difference is then  $2f_n - f_{2n} = 2(n f_{\text{rep}} + f_{\text{ceo}}) - 2n f_{\text{rep}} - f_{\text{ceo}} = f_{\text{ceo}}$ . Stabilizing both the ceo frequency and the pulse repetition rate by comparison to a microwave frequency standard, the frequencies of all comb modes are known within the instability of the microwave reference.

A frequency comb can be used as a “ruler” to measure optical frequencies as  $f_{\text{opt}} = f_{\text{ceo}} + n f_{\text{rep}} + \Delta f$ , where  $n$  is the integer number of the comb mode closest to  $f_{\text{opt}}$  and  $\Delta f$  is the beat frequency between the  $n^{\text{th}}$  comb mode and the measured optical frequency. For a suitable spacing of the comb modes, the mode number  $n$

can be determined with a conventional wavemeter. The instability properties of femtosecond frequency combs have been studied in detail [40,91,92] and it can be expected that their contribution to the uncertainty of frequency measurements can be negligible. Femtosecond frequency combs can thus in the future provide the “clockwork” for optical clocks. Many absolute frequency measurements of optical frequencies were performed over the last years. The absolute frequency of the reference transition of the  $^{171}\text{Yb}^+$  single-ion optical frequency standard was measured twice with a frequency comb relative to a cesium fountain standard. The weighted mean  $f_{\text{Yb}} = 688\,358\,979\,309\,311(6)$  Hz has a relative uncertainty of  $1 \cdot 10^{-14}$  [51, 52]. Recently absolute frequency measurements were performed for reference transitions in  $^{88}\text{Sr}^+$  with a relative uncertainty of  $3.4 \cdot 10^{-15}$  [47] and in  $^{199}\text{Hg}^+$  with a relative uncertainty of  $1.5 \cdot 10^{-15}$  [48], which is the lowest uncertainty reported for an absolute frequency measurement so far.

# Chapter 3

## Trapping and Cooling of a Single $^{171}\text{Yb}^+$ Ion

### 3.1 The Paul Trap

In order to study the properties of a single atom and its interactions with external fields with high precision, it is advantageous to confine the atom for an extended time in a small volume of space. In the case of ions it is most convenient to use electric fields to generate a three dimensional attractive potential. Because of the Laplace equation such a potential can not be realized using only static electric fields. A dynamic trapping of the ion can however be achieved with a time dependent quadrupole potential of the form

$$\phi(\mathbf{r}, t) = (U_{DC} + U_{AC} \cos \Omega t) \frac{(1 + \epsilon)x^2 + (1 - \epsilon)y^2 - 2z^2}{\kappa r_0^2}, \quad (3.1)$$

as was first proposed by W. Paul [22, 93]. The parameter  $r_0$  is a characteristic dimension of the trap and  $\epsilon$  describes the deviation of the potential from cylindrical symmetry. The parameter  $\kappa$  depends on the shapes of the electrodes that generate the trap potential. For an ideal quadrupole trap whose electrodes perfectly conform to hyperbolic equipotential surfaces,  $\kappa = 2$ . Fig. 3.1 illustrates the geometry of the trap electrodes and the potential for an ideal quadrupole trap ( $\epsilon = 0$ ,  $\kappa = 2$ ). The properties of the trap used in the experiments are discussed in Sec. 4.1. The motion of an ion of mass  $m$  and charge  $Q$  in the potential  $\phi(\mathbf{r}, t)$  is described by a set of Mathieu differential equations:

$$\frac{d^2 r_i}{d\tau^2} + (a_i - 2q_i \cos 2\tau)r_i = 0, \quad (3.2)$$

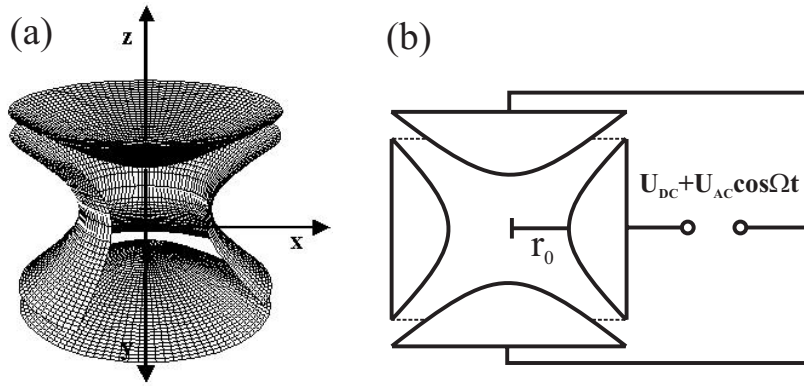


Figure 3.1: Ideal quadrupole trap. (a) Geometry of the equipotential surfaces  $x^2 + y^2 - 2z^2 = \pm r_0^2$  of the ideal quadrupole potential. (b) Section along the  $(x, z)$ -plane through the electrode configuration that generates the ideal quadrupole field.

with

$$a_i = \frac{8\gamma_i Q U_{DC}}{m\Omega^2 \kappa r_0^2}, \quad q_i = \frac{4\gamma_i Q U_{AC}}{m\Omega^2 \kappa r_0^2}, \quad \tau = \frac{\Omega}{2} t, \quad \gamma_i = \begin{cases} (1 + \epsilon) & i = x \\ (1 - \epsilon) & i = y \\ -2 & i = z. \end{cases} \quad (3.3)$$

A detailed discussion of properties of the Mathieu equations can be found in [94]. Here it is only important that for  $a_i, q_i \ll 1$  and  $U_{DC} < U_{AC}$  Eq. (3.2) has stable solutions that can be written as

$$R_i(\tau) = R_i \cos \frac{2\omega_i}{\Omega} \tau \left( 1 + \frac{q_i}{2} \cos 2\tau \right), \quad i = x, y, z. \quad (3.4)$$

The part proportional to  $q_i$  is an oscillation at the trap frequency  $\Omega$ , the so-called micromotion. For times  $\tau > 1/\Omega$  the mean kinetic energy of the micromotion, which is proportional to  $E_i^2$  and thus to the square of the distance from the trap center, acts on the ion as a static pseudo-potential

$$\Phi(R_i) = \frac{m}{4Q} \omega_i^2 R_i^2. \quad (3.5)$$

A measure for the depth of the potential is the quantity

$$D_i \simeq \frac{e\Phi(r_0)}{2}. \quad (3.6)$$

The harmonic motion at the frequency  $\omega_i$  in this pseudo potential is called the secular motion of the ion. From [94, 95] one finds

$$\omega_i \simeq \frac{\Omega}{2} \sqrt{\gamma_i a_i - \frac{(\gamma_i a_i - 1)\gamma_i^2 q_i^2}{2(\gamma_i a_i - 1)^2 - \gamma_i^2 q_i^2} - \frac{(5\gamma_i a_i + 7)\gamma_i^4 q_i^4}{32(\gamma_i a_i - 1)^3(\gamma_i a_i - 4)}}. \quad (3.7)$$

where  $\omega_i$  is given up to order  $q^4$ . In a not perfectly ideal quadrupole potential generated by a real trap, the description of the motion of the ion in the trap given above is nevertheless a good approximation if the ion stays close to the trap center. If the ion is far from the trap center, depending on the actual trap design effects of higher-order multipole terms of the trap potential can become important.

According to the above equations, the ion in the trap oscillates around the field-free trap center and the motions along the three  $R_i$ -directions are independent. For a given potential the amplitudes of the secular and micromotion depend on the initial velocity of the ion and any further interactions with its environment, like collisions with the background gas. In order to achieve a good localization of the ion it is necessary to remove as much of the ion's kinetic energy as possible. In the experiment this is done by laser Doppler cooling, which will be described in Sec. 3.3. Since the amplitude of the micromotion depends on the mean distance of the ion from the trap center, cooling of the secular motion also reduces micromotion as long as the motion is symmetric around the trap center. The situation is usually different if additional electric fields are present that do not have the same symmetry as the trap field (see Sec. 3.4).

It is obvious that without a rapid cooling process in the trap region, ions brought into the trap from the outside will not be trapped due to conservation of energy. In order to store an ion in the trap, a neutral atom is therefore ionized in the trap region either by electron impact or photoionization (see Sec. 4.1).

## 3.2 Level Structure of $^{171}\text{Yb}^+$

Ytterbium is a rare earth metal first discovered in 1878 by Jean de Marignac and named after the swedish village Ytterby. It belongs to the lanthanide group of the periodic table of elements. Table 3.2 at the end of this section lists the seven stable isotopes. Singly ionized ytterbium has a strong alkali-like  $^2S_{1/2} \rightarrow ^2P_{1/2}$  resonance transition that can be used for laser Doppler cooling and detection of the ion by resonance fluorescence. For the realization of a single-ion optical frequency standard,  $^{171}\text{Yb}^+$  is especially well suited. It has a nuclear spin  $I = 1/2$ , so that  $m_F = 0 \rightarrow m_{F'} = 0$  transitions which are not subject to the linear Zeeman effect in low magnetic fields (see Sec. 7.2) are available in a level system with relatively simple hyperfine and magnetic-sublevel structure. Fig. 3.2 shows the relevant energy levels of  $^{171}\text{Yb}^+$  and Table 3.1 gives their lifetimes and hyperfine splittings. A detailed overview of the properties of different transitions in  $^{171}\text{Yb}^+$  and  $^{172}\text{Yb}^+$  and their application in frequency metrology is given in [96, 97].

The quasicycling  $^2S_{1/2}(F = 1) \rightarrow ^2P_{1/2}(F = 0)$  electric dipole transition at 369.5 nm is excited by a linearly polarized laser beam for Doppler cooling and



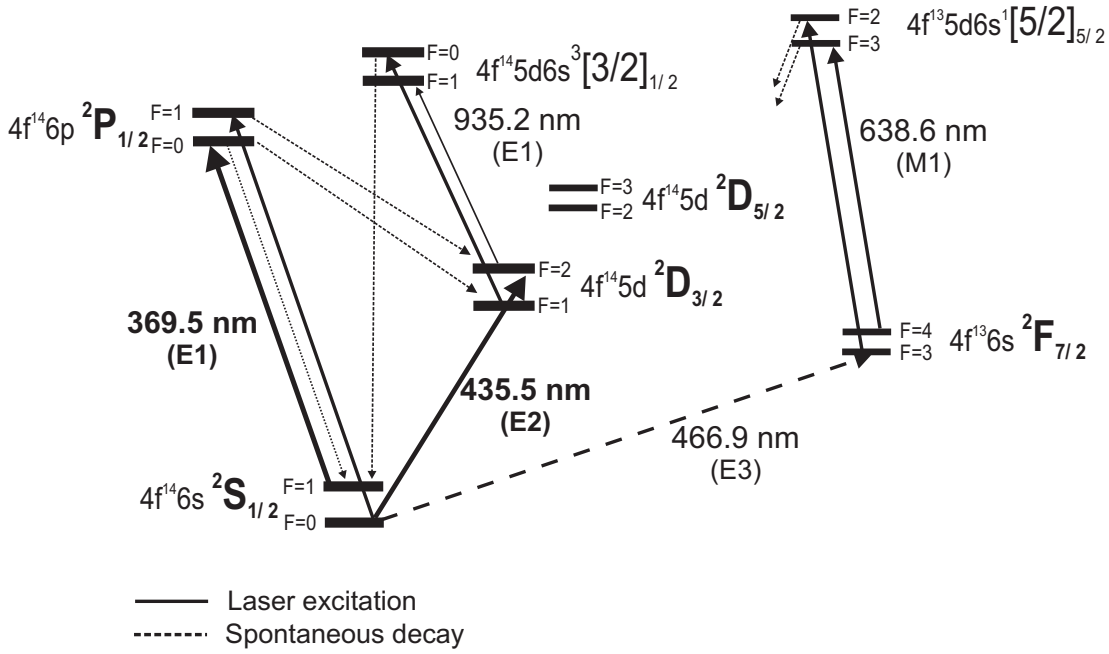


Figure 3.2: Level scheme of the  $^{171}\text{Yb}^+$  ion. The expressions in round brackets label the type (E: electric, M: magnetic) and multipole order of the atomic transition

detection of the ion. The natural linewidth of the cooling transition is  $\gamma_P = \Gamma_P/(2\pi) \simeq 23$  MHz. In the experiment the fluorescence rate on resonance is  $R \simeq 1 \cdot 10^7 \text{ s}^{-1}$ , well below the saturation limit  $R_{max} = \Gamma_P/2 \simeq 7.2 \cdot 10^7 \text{ s}^{-1}$ . For optimum laser cooling the laser is usually detuned by  $\Delta_L = -\gamma_P/2$  from resonance. In order to avoid optical pumping to nonabsorbing superpositions of magnetic sublevels in the  $^2S_{1/2}(F=1)$  manifold, a Larmor precession frequency of order  $R/(2\pi)$  is introduced by a static magnetic field  $|\mathbf{B}| \simeq 400 \mu\text{T}$  oriented at an oblique angle with the polarization of the cooling laser field. The optimum value for  $|\mathbf{B}|$  and the orientation of the laser polarization are adjusted by maximizing the fluorescence rate  $R$ .

By nonresonant excitation the cooling laser can populate the  $^2P_{1/2}(F=1)$  state with a rate  $R_{NR} \simeq R(\Gamma_P/(2\Delta_{P_{1/2}}))^2 \simeq 3 \cdot 10^2 \text{ s}^{-1}$ , where  $\Delta_{P_{1/2}}$  is the hyperfine splitting of the  $^2P_{1/2}$  state. Spontaneous decay from the  $^2S_{1/2}(F=1)$  state is predominantly to the  $^2S_{1/2}(F=0)$  state, which is not excited by the cooling laser. In order to ensure a continuous scattering of photons from the cooling laser, the  $^2S_{1/2}(F=0)$  state is depopulated by a repumper sideband of the cooling laser that is in resonance with the  $^2S_{1/2}(F=0) \rightarrow ^2P_{1/2}(F=1)$  transition.

The  $^2P_{1/2}$  state can also decay with probability of approximately  $7 \cdot 10^{-3}$  to the  $^2D_{3/2}$  state which decays to the  $^2S_{1/2}$  state after a natural lifetime of about

Table 3.1: Properties of the atomic levels in  $^{171}\text{Yb}^+$  relevant for laser cooling and detection

State	Measured lifetime	Hyperfine splitting	Reference
$^2S_{1/2}$	-	$\Delta_{S_{1/2}} = 2\pi \cdot 12.6 \text{ GHz}$	[98]
$^2P_{1/2}$	8.1(1) ns	$\Delta_{P_{1/2}} = 2\pi \cdot 2.1 \text{ GHz}$	[99, 100]
$^2D_{3/2}$	52(1) ms	$\Delta_{D_{3/2}} = 2\pi \cdot 0.86 \text{ GHz}$	[101, 102]
$^2D_{5/2}$	20(5) ms	$\Delta_{D_{5/2}} = 2\pi \cdot 0.82 \text{ GHz}$	[96, 103]
$^3[3/2]_{1/2}$	37.7(5) ns	$\Delta_{[3/2]} = 2\pi \cdot 2.5 \text{ GHz}$	[98]
$^1[5/2]_{5/2}$	<160 ms	$\Delta_{[5/2]} = 2\pi \cdot 0.191 \text{ GHz}$	[97, 103]
$^2F_{7/2}$	$\leq 10 \text{ yr}$	$\Delta_{F_{7/2}} = 2\pi \cdot 3.6 \text{ GHz}$	[104, 105]

52 ms and thus causes extended dark periods in the fluorescence of the ion. An additional repumper laser at  $\lambda = 935.2 \text{ nm}$  is therefore used to excite the ion resonantly from the  $^2D_{3/2}(F = 1)$  state to the  $^3[3/2]_{1/2}(F = 0)$  state from where the ion decays rapidly to the  $^2S_{1/2}(F = 1)$  ground state. Due to the rather small hyperfine splittings  $\Delta_{D_{3/2}} = 2\pi \cdot 0.86 \text{ GHz}$  of the  $^2D_{3/2}$  state and  $\Delta_{[3/2]} = 2\pi \cdot 2.5 \text{ GHz}$  of the  $^3[3/2]_{1/2}$  state this laser can also nonresonantly excite the  $^2D_{3/2}(F = 2) \rightarrow ^3[3/2]_{1/2}(F = 1)$  transition. This effectively reduces the lifetime of the  $^2D_{3/2}(F = 2)$  state, which has to be accounted for in the interrogation of the 435.5 nm transition (see Sec. 4.2.2).

Collisions with the background gas can also lead to a population of the  $^2D_{5/2}$  state which can decay to the extremely long-lived  $^2F_{7/2}$  state. This can happen several times per hour, depending on the pressure of the background gas. A laser at  $\lambda = 638.6 \text{ nm}$  transfers the atom to the  $^3[5/2]_{5/2}$  state, reducing the average dwell times in the  $^2F_{7/2}$  state from  $\sim 1 \text{ h}$  to  $\sim 1 \text{ s}$ .

Several transitions in  $^{171}\text{Yb}^+$  can be used for the realization of an atomic frequency standard. The transition studied in this work is the  $^2S_{1/2}(F = 0, m_F = 0) \rightarrow ^2D_{3/2}(F = 2, m_F = 0)$  electric quadrupole transition with a natural linewidth of 3.1 Hz at 435.5 nm, which will be simply called clock transition in the following. Other transitions that are currently investigated are the  $^2S_{1/2}(F = 0) \rightarrow ^2F_{7/2}(F = 3)$  electric octupole transition [43, 44, 47] and the  $^2S_{1/2}(F = 0) \rightarrow ^2S_{1/2}(F = 1)$  microwave hyperfine transition [106].

Table 3.2: Stable isotopes of ytterbium

Isotope	Atomic mass	Nuclear spin	Abundance [%]
168	167.934	0	0.135
170	169.935	0	3.03
171	170.937	1/2	14.31
172	171.937	0	21.82
173	172.938	5/2	16.13
174	173.939	0	31.84
176	175.943	0	12.73

### 3.3 Laser Cooling of $^{171}\text{Yb}^+$

After a ytterbium atom is ionized in the trap region, the ion has a mean kinetic energy which is at least one half of the value of the pseudo-potential at the point of ionization. In order to achieve a good localization of the ion, its velocity is reduced by laser cooling on the  $^2\text{S}_{1/2}(F = 1) \rightarrow ^2\text{P}_{1/2}(F = 0)$  transition. A detailed description the theory of laser cooling is given in [107–109].

In a semi-classical picture laser cooling of a free atom can be understood qualitatively as follows: The atom will predominantly absorb photons from the laser if the Doppler shift due to its velocity brings the laser frequency  $\omega_L$  and the atomic transition frequency  $\omega_0$  into resonance. The emission of photons by spontaneous decay is isotropic and therefore on average no momentum is transferred to the atom by the emission process. After  $N \gg 1$  cycles of absorption and emission the kinetic energy of the atom has therefore in the rest frame of the laser changed by  $N\hbar(\omega_L - \omega_0) + 2E_R$ , where  $E_R = (\hbar\mathbf{k}_L)^2/(2M)$  is the energy of the photon recoil. For  $\omega_L < \omega_0 + 2E_R$  the velocity of the atom is reduced. If only one laser is used, only the velocity of the motion towards the laser beam will be reduced, while in the opposite direction and in the plane perpendicular to the laser beam heating will occur due to the photon recoil. Thus in general for every direction of motion laserlight fulfilling  $\omega_L < \omega_0 + 2E_R$  is necessary, in order to cool all directions of motion of a free atom.

The situation is different if the atom is bound by a potential with discrete energy eigenstates, like the harmonic potential of a Paul trap. If the energy difference between the eigenstates of the potential is large compared to the photon recoil energy, the photon recoil can only with small probability excite the atom to a higher motional state. Most of the time, the photon recoil instead increases the kinetic energy of the center of mass motion of the atom-trap-system. However, the corresponding velocity change of the center of mass is zero because the trap is treated as having infinite mass, which is equivalent to the assumption that

the trap potential itself is unaffected by the dynamics of the atom. For an atom trapped in a harmonic potential, one laser beam is sufficient to cool the motion of the atom in the potential in three dimensions as long as the secular frequencies for the three directions of motions are not degenerate and the laser beam has a finite projection on all three directions of motion. Then no stationary oscillation of the atom perpendicular to the laser beam exists.

At the beginning of the cooling process in a harmonic potential the kinetic energy of the atom is so large that the quantum nature of its motion can be neglected and the motion of the atom can be treated as a classical harmonic oscillator. The cooling process in this regime is discussed in detail for example in [107, 108]. In the following the discussion of laser cooling of an atom in a harmonic trap potential will concentrate on the final stage of the process when the atom has reached the so called Lamb-Dicke regime where it is localized on a scale smaller than the laser wavelength and the quantum mechanical description of the motion is simplified. The internal degrees of freedom of the atom are described as a two-level system, while the laser field is treated as a classical plane wave. The saturation parameter  $s = 2\Omega_R^2/\Gamma^2$  is assumed to be much smaller than one. Here  $\Omega_R$  is the resonant Rabi frequency for the interaction of the laser with the two level system and  $\Gamma$  is the decay rate of the excited state. This means that the intensity of the laser light is assumed to be small enough that a motional state  $n$  of the harmonic oscillator is coupled only to adjacent states  $n - 1, n + 1$  by the interaction with the laser field. Further it is assumed that the cooling process is slow compared to the internal dynamics of the atom so that the interaction of the internal degrees of freedom with the light field is determined by the steady-state solution of the Bloch equations for a two-level atom at rest. The time evolution is then described by the Hamiltonian [109]

$$H = H_0 + H_{cm} + H_{dipole}, \quad (3.8)$$

$$H_0 = -\hbar \frac{\Delta_L}{2} \sigma_z, \quad (3.9)$$

$$H_{cm} = \frac{\mathbf{p}^2}{2m} + \frac{1}{2}m(\omega_x^2 x^2 + \omega_y^2 y^2 + \omega_z^2 z^2), \quad (3.10)$$

$$H_{dipole}(\mathbf{r}) = \hbar \frac{\Omega_R}{2} (\sigma^+ e^{-i\mathbf{k}_L \mathbf{r}} + \sigma^- e^{i\mathbf{k}_L \mathbf{r}}), \quad (3.11)$$

where  $H_0$  is the Hamiltonian of the free two-level atom,  $H_{dipole}$  describes the dipole interaction of the laser with the atom and  $H_{cm}$  describes the center of mass motion of the atom in the trap. The following quantities were introduced:  $\sigma^\pm$  are the pseudospin operators of the two level system, the components of the Bloch vector are  $\sigma_x = \sigma^+ + \sigma^-$ ,  $\sigma_y = (\sigma^+ - \sigma^-)/i$ , and  $\sigma_z$ ,  $\Delta_L$  is the detuning of the laser from resonance,  $\mathbf{k}_L$  is the wave vector of the laser,  $\mathbf{r}$ ,  $\mathbf{p}$  are the position and momentum operators of the atom, and  $m$  is the mass of the atom.

In the Lamb-Dicke regime  $H_{dipole}$  can be expanded in powers of  $\mathbf{k}_L \mathbf{r} \sim 2\pi r/\lambda \ll 1$ .

Up to first order, one finds

$$H_{dipole}(\mathbf{r}) = H_{dipole}(0) - \mathbf{F}(0) \cdot \mathbf{r} + \dots = \frac{\Omega_R}{2} \sigma_x - \frac{\Omega_R}{2} \mathbf{k}_L \cdot \mathbf{r} \sigma_y + \dots \quad (3.12)$$

The second term is the dipole force of the laser field acting on an atom at rest. The steady-state solution of the Bloch equations for the atomic polarization  $\sigma_y$  averaged over the internal degrees of freedom of the atom is [109]

$$\langle \sigma_y \rangle_{SS} = \frac{\Gamma \Omega_R}{\Gamma^2/2 + 2\Delta_L^2 + \Omega_R^2} \quad (3.13)$$

The dipole force on the atom at rest is then given by

$$\mathbf{F}(0) = \hbar \mathbf{k}_L \frac{\Gamma \Omega_R^2}{\Gamma^2 + 4\Delta_L^2 + 2\Omega_R^2}. \quad (3.14)$$

The time evolution of the mean vibrational quantum number of the atom is described by a master equation that can be written as [109]

$$\frac{d}{dt} \langle n_i \rangle = -(A_i^- - A_i^+) \langle n_i \rangle + A_i^+, \quad i = x, y, z. \quad (3.15)$$

The functions  $A_i^-$ ,  $A_i^+$  describe the rates at which the atom is transferred from a given vibrational state  $n$  to the nearest lower vibrational state ( $n - 1$ ) or excited to the next higher one ( $n + 1$ ) by the absorption of a photon from the laser field. The rates are given by

$$A_i^- = 2\text{Re}[S(\omega_i) + D_i], \quad (3.16)$$

$$A_i^+ = 2\text{Re}[S(-\omega_i) + D_i], \quad (3.17)$$

where

$$S(\omega_i) = \eta_i^2 \left( \frac{\Omega_R}{2} \right)^2 \int_0^\infty e^{i\omega_i t} \langle \sigma_y(t) \sigma_y(0) \rangle_{SS} dt \quad (3.18)$$

is the fluctuation spectrum of the dipole force. Because of the motion of the atom it is phase modulated in the rest frame of the atom. The diffusion term

$$D_i = \alpha \frac{\eta_i^2 \Gamma \Omega_R^2}{(\Gamma^2 + 4\Delta_L^2 + 2\Omega_R^2)} \quad (3.19)$$

describes a random walk of the center of mass in momentum space due to spontaneous emission. The parameter  $\alpha$  depends on the angular pattern of the spontaneous emission. For isotropic emission it is equal to  $1/3$ . The  $\eta_i$  are the Lamb-Dicke parameters defined as

$$\eta_i = \frac{2\pi \cos \theta_i}{\lambda_L} \sqrt{\frac{\hbar}{2m\omega_i}}, \quad (3.20)$$

where the  $\theta_i$  are the angles between the laser and the three directions of motion. All the equations involving the Lamb-Dicke parameters are valid up to order  $\eta_i^2$ .

If  $W_i = A_i^- - A_i^+ > 0$  in Eq. (3.15), the motion of the atom in the trap is cooled and  $W_i$  is therefore called the cooling rate. The dynamics described by Eq. (3.15) is similar to that of a damped harmonic oscillator coupled to a finite temperature reservoir. Here the reservoir is the phase modulated dipole field of the laser and the damping is the spontaneous emission. The end of the cooling process is reached when  $\frac{d}{dt} \langle n_i \rangle = 0$  and the steady state energy above the motional ground state is

$$E_i = \hbar\omega_i \frac{A_i^+}{A_i^- - A_i^+} = \hbar\omega_i \frac{A_i^+}{W_i}. \quad (3.21)$$

Two regimes for laser cooling of bound atoms can be distinguished depending on the ratio of the secular frequencies  $\omega_i$  relative to the spontaneous decay rate  $\Gamma$  on the cooling transition:

For  $\omega_i \gg \Gamma$ , the atom is in the regime of “strong” binding. Here the motion of the atom leads to discrete sidebands in the spectrum of the atom at multiples of the secular frequencies  $\omega_i$ . It can be shown [108] that in this case the atom can be transferred to the motional ground state of the potential by selectively exciting it on the first red detuned secular sideband (assuming that the laser linewidth is small compared to the secular frequencies). This process can be viewed as optical pumping between motional states via the excited state of the atom or as anti-Stokes Raman scattering by the bound atom in the trap.

If  $\omega_i \ll \Gamma$ , the atom is in the regime of “weak” binding also called the “heavy particle limit” [107], where the motion of the atom is slow compared to the time for the absorption and emission of one photon. The cooling process can then be regarded as instantaneous and the situation is similar to the one for Doppler cooling of a free atom.

For the case of the  $^2S_{1/2}(F=1) \rightarrow ^2P_{1/2}(F=0)$  cooling transition in  $^{171}\text{Yb}^+$  one has  $\omega_i/\Gamma < 5 \cdot 10^{-3} \ll 1$  so that the condition for the weak binding regime is fulfilled. The real part of the fluctuation spectrum of the dipole force in the weak binding regime calculated from Eq. (3.14) is given by [110]:

$$S(\pm\omega_i) = \frac{\eta_i^2 \Gamma \Omega_R^2}{\Gamma^2 + 4(\Delta_L \mp \omega_i)^2 + 2\Omega_R^2}, \quad (3.22)$$

which leads up to zero order in  $\omega_i/\Gamma$  to a cooling rate

$$W_i \simeq -\frac{8\eta_i^2 s}{\Gamma} \frac{\omega_i \Delta_L}{(1 + s + 4\Delta_L^2/\Gamma^2)^2}. \quad (3.23)$$

The steady state energy is then also up to zero order in  $\omega_i/\Gamma$  given by

$$E_i \simeq -\frac{\hbar\Gamma}{8} (1 + \alpha) \left( (1 + s) \frac{\Gamma}{2\Delta_L} + \frac{2\Delta_L}{\Gamma} \right). \quad (3.24)$$

This energy has a minimum for  $\Delta_L = -\sqrt{1+s}\Gamma/2$ . In the limit  $s \rightarrow 0$  this leads to the so-called Doppler limit

$$E_D = \hbar \frac{\Gamma(1+\alpha)}{4} = \frac{1}{2} k_B T_D, \quad (3.25)$$

where  $k_B$  is Boltzmann's constant. The effective temperature  $T_D$  is called the Doppler temperature. For  $\alpha = 1/3$ ,  $T_D \simeq 0.37$  mK in the experiment. In the limit  $\omega_i/\Gamma \rightarrow 0$ , used to derive the Doppler limit, the final temperature is independent of the secular frequency  $\omega_i$  and the Lamb-Dicke Parameters  $\eta_i$  and therefore the same for all three directions of motion. This reflects the fact that Doppler cooling is ultimately limited by the diffusion in momentum space due to spontaneous emission. For  $\alpha = 1/3$ , the mean vibrational quantum numbers  $\langle n_i \rangle_D$  at the Doppler limit are

$$\langle n_i \rangle_D = \frac{\Gamma}{3\omega_i} - \frac{1}{2} \simeq \begin{cases} 11 & i = x, y \\ 5 & i = z \end{cases}. \quad (3.26)$$

For the cooling transition of  $^{171}\text{Yb}^+$  used in the experiments the harmonic motion of the ion does not lead to resolved sidebands in the fluorescence spectrum because  $\omega_i \ll \Gamma$ . However, the width and relative intensity of the motional sidebands can still be studied by optical heterodyne methods [110].

For the clock transition one has  $\omega_i \gg \Gamma$ . The motional sidebands are well resolved and their intensities relative to the central resonance at the Doppler limit are given by [107]

$$\frac{I_i^\pm}{I_0} \simeq \eta_i^2 \begin{pmatrix} \langle n_i \rangle_D + 0 \\ 1 \end{pmatrix} = \cos^2 \theta_i \begin{cases} 0.14(-), 0.15(+) & i = x, y \\ 0.03(-), 0.04(+) & i = z \end{cases} \quad (3.27)$$

Here  $(-)$ ,  $(+)$  denote the respective first sideband below (above) the resonance and the Lamb-Dicke parameters in the experiment are  $\eta_{x,y} \simeq 0.11 \cos \theta_{x,y}$ ,  $\eta_z \simeq 0.08 \cos \theta_z$ . Eq. (3.27) presents another way of stating the condition for the Lamb-Dicke regime. The modulation indices that determine the intensities of the sidebands are  $\beta_i = k_L \cos \theta_i r_i$ , where  $r_i$  is the amplitude of the ion motion in the  $i$ -direction. Going back to the definition of the Lamb-Dicke Parameters one finds that for  $\langle n_i \rangle_D = 0$ ,  $\beta_i = \eta_i$ . The condition  $\eta_i \ll 1$  for the Lamb-Dicke regime is therefore equivalent to stating that the spectrum of the ion consists only of a carrier and two sidebands which are weak compared to the carrier. The values for the  $I_i^\pm$  given above thus justify the previous assumption that the final stage of the cooling process takes place in the Lamb-Dicke regime. Since the Lamb-Dicke parameters depend on the inverse of the secular frequencies  $\omega_i$ , it is obvious that in order to reach the Lamb-Dicke regime the trap has to be designed such that the secular frequencies are high enough to obtain  $\eta_i \ll 1$ . The calculated values  $I_i^\pm$  can be compared with measurements in order to verify that the cooling process brings the ion close to the Doppler limit in the experiment (see Sec. 5.3.1).

As has been discussed in Sec. 3.2, the cooling scheme for the ytterbium ion involves not only the  $^2S_{1/2}(F=1)$ ,  $^2P_{1/2}(F=0)$  four-level system but also other atomic states. However, a detailed theoretical and experimental investigation of the fluorescence spectrum of the cooling transition has shown [110] that the formalism for the two-level system is a good description for the ytterbium system. The main modification with respect of the two-level system is that for the ytterbium case the total elastic scattering rate on the cooling transition is about six times lower than for a two-level system with the same natural decay rate  $\Gamma$ . This modifies the saturation condition, but plays no role for an excitation far below saturation.

### 3.4 Compensation of the Electric Stray Field

The considerations in the previous sections assumed that aside from the trap potential (3.1) no other external electric fields are present. The effect of an additional static electric stray field  $\mathbf{E}$  on the motion of the ion is especially important, because it leads to a force  $\mathbf{F} = Q\mathbf{E}$  that shifts the mean position of the ion away from the otherwise field free trap center to a new equilibrium position [111]

$$R'_i = \frac{8QE_i}{m(2a_i + q_i^2)\Omega^2} \simeq \frac{QE_i}{m\omega_i^2}, \quad i = x, y, z. \quad (3.28)$$

The ion oscillates around the new position  $\mathbf{R}'$  and as a result micromotion is no longer cooled effectively, because it is now driven motion. This driven micromotion is also called “excess” micromotion [111], to distinguish it from the one caused by the secular motion. The mean square of the trap field at the position  $\mathbf{R}'$  is [111]

$$\langle E_{trap}^2(\mathbf{R}') \rangle_i = \frac{m\Omega^2 k_B T_i}{2Q^2} \frac{a_i^2 + 2q_i^2}{2a_i + q_i^2} + 8 \left( \frac{q_i E_i}{2a_i + q_i^2} \right)^2, \quad (3.29)$$

where  $T_i$  is the effective kinetic temperature of the secular motion along the  $R_i$ -direction. The first term is the mean square field due to the secular motion, while the second term is the contribution from the electric stray field. As will be seen in Sec. 7.3, this second term can lead to significant quadratic Stark shifts of the atomic levels, while the excess micromotion is the main source of the second order Doppler shift discussed in Sec. 7.1. A good compensation of the electric stray field is therefore necessary in order to attain small systematic uncertainties for a frequency standard based on trapped ions. If the excess micromotion is large, the ion can also leave the Lamb-Dicke regime. The fluorescence spectrum of the ion would then contain many strong sidebands at multiples of the secular frequencies, which would also complicate laser cooling.



Several schemes for the detection and the reduction of excess micromotion caused by an electric stray field were demonstrated in the past [111–113]. The one used in the experiments described in this work exploits the fact that the shift in the position of the ion due to the electric stray field is according to Eq. (3.28) inversely proportional to the depth of the pseudo-potential, which is again determined by the  $a$ - and  $q$ -parameters. The  $a$ -parameters are proportional to the dc voltage  $U_{DC}$  applied to the trap. If an electric stray field is present, then decreasing (or increasing) the depth of the potential by changing the dc voltage will increase (decrease) the distance of the ion from the trap center, while if no stray field is present the position of the ion will remain the same. Because the  $a$ -parameter for the  $r = (x, y)$  direction is opposite in sign to the one for the  $z$ -direction, the potential can be selectively lowered in either the  $r$ - or the  $z$ -direction by choosing the appropriate sign for  $U_{DC}$ . In the experiment the fluorescence of the ion induced by the cooling laser is imaged with a magnification  $M$  onto an intensified CCD camera, that allows to detect changes in the position of the ion with a resolution  $\delta$ . The resolution of the imaging system is  $\Delta = \delta/M$ . From Eq. (3.28) one finds then for the minimum electric stray field  $\mathbf{E}_{min}$  that can be detected

$$(E_{min})_i = \frac{m\omega_i^2}{N_i Q} \frac{\Delta}{\cos \vartheta_i}, \quad (3.30)$$

where  $N_i$  is the factor by which the potential is lowered and  $\vartheta_i$  is the angle between the direction of motion and its projection on the plane of observation. For the compensation of the electric stray field, additional dc voltages can be applied to compensation electrodes such that the ion does not change its position by more than  $\delta$  in any direction when the depth of the potential is changed. Note that this procedure only leads to a compensation of the electric stray field if the dc and ac quadrupole potentials of the trap have the same reference potential. Therefore  $U_{DC}$  and  $U_{AC}$  are both applied either to the ring or the trap endcaps.

The mean square of the trap field at the position  $\mathbf{R}_{min}$  of the ion after the stray field compensation is according to equations Eq. (3.30) and Eq. (3.29)

$$\langle E_{trap}^2(\mathbf{R}_{min}) \rangle_i \simeq \frac{m\Omega^2 k_B T_i}{2Q^2} \frac{a_i^2 + 2q_i^2}{2a_i + q_i^2} + \frac{1}{8} \left( \frac{q_i m \Omega^2}{Q} \frac{\Delta}{N_i \cos \vartheta_i} \right)^2 \quad (3.31)$$

and the corresponding mean kinetic energy of the excess micromotion after compensation is given by [111]

$$E_{kin,i} \simeq \frac{1}{2} m \left( \frac{q_i \Omega}{\sqrt{8}} \frac{\Delta}{N_i \cos \vartheta_i} \right)^2 = \frac{1}{2} m \langle v_i^2 \rangle \equiv \frac{1}{2} k_B T'_i, \quad (3.32)$$

where  $\langle v_i^2 \rangle$  is the effective mean square velocity of the excess micromotion and  $T'_i$  denotes the effective kinetic temperature of the excess micromotion. In the experiment typical values for the parameters are  $\Omega \simeq 2\pi \cdot 16$  MHz,

$a_x = a_y = a_z = 0$ ,  $q_r \equiv q_x \simeq q_y = 0.11$ ,  $q_z = -0.22$ ,  $\omega_r \equiv \omega_x \simeq \omega_y = 2\pi \cdot 660$  kHz,  $\omega_z \simeq 2\pi \cdot 1.34$  MHz,  $\Delta = 1.6$   $\mu\text{m}$ , and  $\vartheta_i < \pi/3$ . The trap potential is typically lowered to about 0.25 eV in the  $r$ - as well as the  $z$ -direction, corresponding to  $N_z = 64 = 2N_r$ . If the secular motion is at the Doppler limit  $T_r = T_z = T_D \simeq 0.37$  mK, one finds:

$$(E_{min})_z \simeq 2(E_{min})_r < 6 \frac{\text{V}}{\text{m}}, \quad (3.33)$$

$$|\mathbf{R}_{min}| \simeq 100 \text{ nm}, \quad (3.34)$$

$$\langle E_{trap}^2(\mathbf{R}_{min}) \rangle_z \simeq \langle E_{trap}^2(\mathbf{R}_{min}) \rangle_r < 6000 \frac{\text{V}^2}{\text{m}^2}, \quad (3.35)$$

$$T'_r \simeq T'_z < 5 \text{ mK}. \quad (3.36)$$

So far only the effects of a static stray field was discussed. The influence of a time dependent electric stray field depends on the time scale of its variation. A Stray field that varies slowly compared to the time needed for the compensation procedure can be detected by repeating the compensation several times and the rate of change in the compensation voltages yields information about the time scale of the stray field variation. Such a drift of the compensation voltages can pose a problem, because it limits the length of continuous time intervals available for measurements. For the experimental setup described in this work it was found that the compensation voltages normally do not change detectably over several hours and only slight changes are typically observed from one day to another, except for the time directly after an ion was loaded into the trap. In this case it takes approximately one day until the compensation voltages are again stable enough to do precision measurements. This effect is probably due to the large amount of charges deposited on the trap electrodes during the loading process. Part of these charges might become trapped for long times in areas where due to impurities on the surface of the trap electrodes their mobility is hampered. A Stray field that varies on short timescales would lead either to observable oscillations or distortions of the ion's image on the CCD camera, both of which are not observed in the experiment.

Another effect that can lead to excess micromotion is a phase difference between the potentials applied to the trap electrodes [111]. Tests in which the fluorescence rate on the cooling transition was observed as a function of an applied variable phase difference suggest that no significant phase shifts are present in the experiment under normal operating conditions [114].

# Chapter 4

## Experimental Setup

### 4.1 The Traps

Two Paul traps of identical design are used in the experiments. Fig. 4.1 shows a schematic drawing of the electrode configuration and Fig. 4.2 shows a photograph of one of the traps. Instead of using electrodes with hyperbolic surfaces as shown in Fig. 3.1, the inner side of the ring electrode and the ends of the endcap electrodes have conical shapes that were designed to generate a potential which is close to the ideal quadrupole potential [115,116]. The trap electrodes are made of molybdenum and the inner diameter of the ring electrode is  $2r_0 = 1.4$  mm. The theoretical geometry parameter for this trap design is  $\kappa \simeq 2.16^1$ . The conical trap electrodes are much more easy to manufacture than the hyperbolic ones and offer the additional advantage of a larger accessible solid angle for fluorescence detection and positioning of laser beams.

The traps are typically operated at a radiofrequency trap drive voltage of  $U_{AC} \simeq 600$  V at a frequency  $\Omega \simeq 2\pi \cdot 16$  MHz, leading for zero dc trap voltage  $U_{DC}$  to a potential depth of about 17 eV in the axial direction and secular frequencies  $\omega_z \simeq \omega_x + \omega_y \simeq 2\pi \cdot 1.3$  MHz. The  $q$ -parameters obtained from these values are  $q_z \simeq -0.22$  and  $q_x \simeq q_y \simeq 0.11$ . The potential is to a good approximation cylindrically symmetric. The relative splitting of the radial secular frequencies  $2(\omega_x - \omega_y)/(\omega_x + \omega_y)$  is only about 1% (see Sec. 5.3.1). The values of the parameters  $\kappa/r_0^2$  and  $U_{AC}$  are difficult to measure directly, but they can be determined from measurements of the secular frequencies with high accuracy using the formulas from Sec. 3.1. The results obtained agree with the values derived from the assumed trap geometry and with numerical simulations of the trap potential to within 5%. Both the radiofrequency voltage  $U_{AC}$  and the static voltage  $U_{DC}$  are applied to the ring electrode. An additional differential voltage

---

<sup>1</sup>The trap design corresponds to the configuration No. 4 in [115].

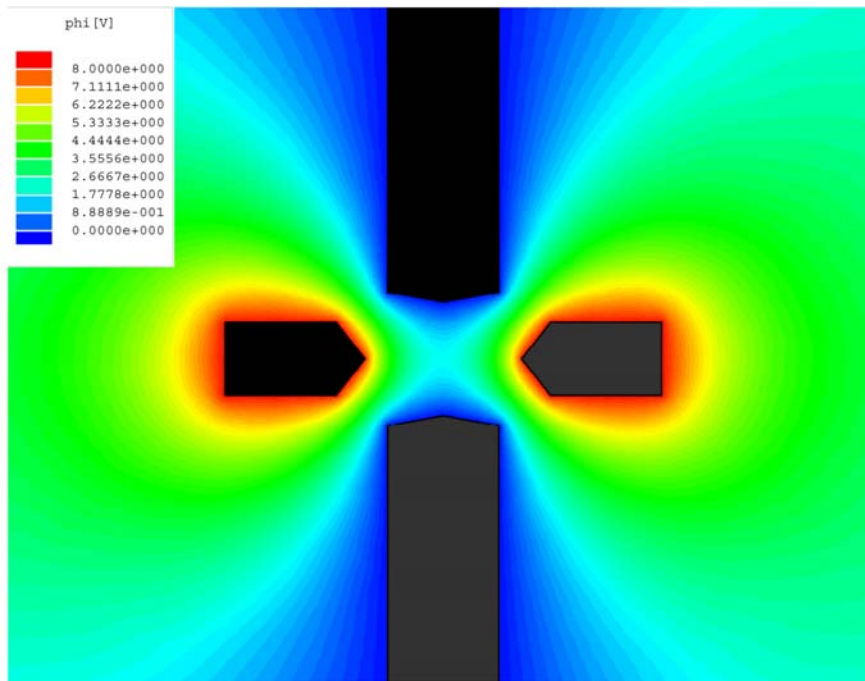


Figure 4.1: Section along the  $(x, z)$ -plane through the trap electrode configuration (black) used in the experiment. A numerical simulation of the electric potential  $\Phi$  outside the electrodes is shown for voltages  $U_{AC} = 0$  V,  $U_{DC} = 8$  V applied to the ring electrode relative to the endcap electrodes.

can be applied between the endcap electrodes for compensation of the electric stray field along the trap axis.

The traps are mounted in the centers of cubic quartz glass vacuum chambers with a size of about  $50 \times 50 \times 50$  mm<sup>3</sup> pumped by ion getter pumps. The pressure of the residual gas is below  $10^{-7}$  Pa, except for hydrogen that has an estimated partial pressure of  $\leq 10^{-6}$  Pa. Optical access to the trap is provided through one flat side of the quartz cube for fluorescence detection and four Brewster windows for laser excitation mounted on the cube faces perpendicular to the observation window. The connection to the getter pump and the mechanical mounting of the trap are on the opposite side of the of the observation window. The maximum aperture angle of the trap is about  $38^\circ$ . The vacuum chamber is held by a metal mount that rests on an optical table. Pieces of silicon rubber between the mount and the vacuum chamber and below the mount provide vibration isolation against the optical table. A separate metal box around the vacuum chamber protects the trap from electric stray fields and ambient light.

Ions are loaded into the trap by ionizing neutral ytterbium atoms in the trap region by electron impact. For this purpose a tantalum tube filled with metal-



Figure 4.2: Picture of one of the traps used in the experiments. 1: ring electrode ( $\text{\O}1.4$  mm), 2: endcap electrode, 3: ytterbium oven, 4: electron source.

lic ytterbium<sup>2</sup> and an electron source realized by a thoriated-wolfram wire are mounted at distances of about 5 mm from the trap. The tantalum tube is heated electrically until a sufficiently large amount of neutral ytterbium starts to evaporate, then the heating is switched off and a current  $I_e$  through the electron source is switched on for a short time  $t_e$ . Some of the electrons emitted from the wire collide with the ytterbium atoms and produce positive ions. Some of these will get trapped in the electrical potential of the trap. The final temperature of the tube and the total charge emitted by the wire which is proportional to  $I_e t_e$  are normally chosen such that on average at most one ion is stored in the trap during one loading cycle. Additional static voltages applied to the electron source and the oven are used in conjunction with the differential voltage between the trap endcaps for the compensation of the electric stray field (see Sec. 3.4). For this purpose the electron source and the oven are mounted at a mutual angle of approximately  $90^\circ$ .

A problem of the loading process described above is its low efficiency. Over time this leads to a noticeable inhomogeneous coating of the trap electrodes with ytterbium. The contact potentials at the interface of these patches with the electrode material is believed to be one source of the electric stray field leading to excess micromotion. Over time there may form also thin layers of

---

<sup>2</sup>Both traps have ovens for  $^{171}\text{Yb}$  and one has an additional oven for  $^{172}\text{Yb}$ .

oxides or other insulating materials on some parts of the trap electrodes. Because electrons deposited on such patches can be trapped there for long times, the use of an electron source for ionization tends to increase the problem of electric stray fields even further. A better method for ionizing the ytterbium atoms would be photoionization by resonant two-photon absorption which has already been demonstrated in various experiments for different atoms [117–120]. Due to the much higher efficiency considerably smaller amounts of ytterbium have to be evaporated from the oven and the number of ions that can be loaded into the trap in a given time can be controlled much more precisely, reducing the number of loading cycles. Moreover, the ionization process can be isotope-selective by choosing a suitable frequency of the ionization laser. Aside from being thus more convenient, the main advantages of photoionization are that it reduces the amount of ytterbium deposited on the trap electrodes during loading and requires no electron source.

The storage time for single ytterbium ions in the traps is extremely long even without laser cooling and up to now, no limiting mechanism for the storage time has been identified. The longest observed storage time was 16 months. The typical storage time is several months, limited by accidental ion loss during the stray field compensation procedure when the trap potential is lowered.

The strength and direction of the magnetic field in the trap is adjusted by three sets of coils. The first set consisting of three single rectangular coils is located outside the light shield box and is used to compensate the earth's magnetic field. A pair of coils mounted close to the vacuum chamber at an angle of  $45^\circ$  to the Brewster windows provides the bias magnetic field of about  $400 \mu\text{T}$  needed for laser cooling of the ions (see Sec. 3.2). During excitation of the clock transition by the probe laser the bias field is switched to a lower value of  $\leq 1 \mu\text{T}$ . Two additional single coils are mounted close to the trap at a mutual angle of  $90^\circ$  in the plane perpendicular to the direction of the bias field. Together with the bias field coils, these coils realize an approximately orthogonal set of magnetic field orientations that is used to adjust the magnetic field for spectroscopy of the clock transition.

## 4.2 Lasers

Three laser systems at the wavelengths 369.5 nm [121], 935.2 nm [110], and 638.6 nm [110] are employed for laser cooling and detection of the ion, and one at 435.5 nm [63] is used for the spectroscopy of the clock transition. One of the advantages of the ytterbium system is that all the necessary wavelengths can be produced from diode lasers, either directly or by frequency doubling. Except for the 935 nm sources all lasers are shared between the two trap systems.

The properties of the individual laser systems are summarized in the following sections.

### 4.2.1 Cooling Laser

Laser Doppler cooling of  $^{171}\text{Yb}^+$  is done on the quasicycling  $^2S_{1/2}(F = 1) \rightarrow ^2P_{1/2}(F = 0)$  dipole transition at 369.5 nm by a frequency-doubled extended-cavity diode laser at 739 nm. The frequency doubling is done with a  $\text{LiIO}_3$  crystal in a ring resonator of finesse  $\sim 400$  and with a free spectral range of  $\sim 750$  MHz which acts also as a reference resonator for the short term frequency stabilization of the laser. The output power of the laser at 369.5 nm is about  $10 \mu\text{W}$  in a bandwidth of less than 0.5 MHz, which is much smaller than the natural linewidth of the cooling transition. The typical drift of the laser frequency is  $\sim 1$  MHz/min. The output beam of the laser is split into two beams in order to allow simultaneous laser cooling in both available trap systems. Typical laser powers used for driving the cooling transition below saturation are about  $2 \mu\text{W}$  for a beam waist in the trap of about  $50 \mu\text{m}$ . By modulation of the injection current of the 739 nm diode laser at 14.7 GHz, a sideband is generated that excites the  $^2S_{1/2}(F = 0) \rightarrow ^2P_{1/2}(F = 1)$  repumper transition (see Sec. 3.2). The free spectral ranges of the extended cavity and of the ring resonator are chosen such that the sidebands are resonant with both cavities and therefore imparted also on the output at 369.5 nm. The relative strength of the sidebands is a few percent, which is sufficient to reduce the average dwell time of ions in the  $^2S_{1/2}(F = 0)$  state to less than  $10^{-4}$  s.

The linear polarization of the laser is oriented such that the polarization vector lies in the plane defined by the wave vector of the laser and the orientation of the bias magnetic field. For an angle of  $45^\circ$  between the wave vector and the magnetic field this configuration maximizes the fluorescence rate on the cooling transition [110].

### 4.2.2 Repumper Lasers

There are two repumper lasers at 935.2 nm available for the two trap systems. Both are extended-cavity diode lasers, which are frequency stabilized to temperature stabilized Fabry-Perot etalons. By changing the temperature of the etalons, the lasers are tuned to the  $^2D_{3/2}(F = 1) \rightarrow ^3[3/2]_{1/2}(F = 0)$  resonance. The output powers of the two lasers are  $\sim 2$  mW and  $\sim 40$  mW in bandwidths of about 10 MHz. The frequency drift of the Fabry-Perot reference cavities is small enough to keep the laser frequency on the atomic resonance for several hours. Because the lasers also non resonantly excite the  $^2D_{3/2}(F = 2) \rightarrow ^3[3/2]_{1/2}(F = 1)$

transition and thereby reduce the effective lifetime of the upper state of the clock transition, the output power of the lasers is attenuated to about  $100 \mu\text{W}$  for a beam waist of the laser in the trap of about  $50 \mu\text{m}$ . This power is sufficient to efficiently deplete the  $^2D_{3/2}(F = 1)$  level without significantly reducing the lifetime of the  $^2D_{3/2}(F = 2)$  state.

The repumper laser at  $638.6 \text{ nm}$  for depletion of the long-lived  $^2F_{7/2}$  state via the  $^3[5/2]_{5/2}$  state is also an extended-cavity diode laser, but without additional stabilization to an external reference cavity. In order to deplete both hyperfine sublevels of the  $^2F_{7/2}$  state, the linewidth of the laser is intentionally broadened to about  $100 \text{ MHz}$  by a frequency sweep and the center frequency is periodically switched by about  $4.8 \text{ GHz}$ . The output power of the laser is about  $0.7 \text{ mW}$  and as in the case of the cooling laser, the output is divided between the two trap systems.

### 4.2.3 Probe Laser

The light for the excitation of the clock transition is generated from a frequency-doubled extended-cavity diode laser at a wavelength of  $871 \text{ nm}$ . The linewidth of the free-running laser is about  $20 \text{ kHz}$ . In order to achieve a frequency stability of the laser which allows a frequency resolution close to the natural linewidth of the clock transition, the laser frequency is stabilized by the Pound-Drever-Hall method to an external high-finesse reference resonator made out of ultralow expansion (ULE) glass. The finesse of the resonator is approximately  $10^5$  and the free spectral range is  $1.5 \text{ GHz}$ . The resonator is mounted in a vacuum chamber on a commercially available passive vibration isolation platform. Additional isolation against air currents is provided by a box around the platform. About  $10 \mu\text{W}$  of the laser output are used for the stabilization. This light is first passed through an acousto-optical modulator (AOM) and then coupled to the resonator by an optical fiber. The remaining laser output is used to injection lock two other extended cavity diode lasers that are separately frequency doubled with  $\text{KNbO}_3$ -crystals to provide the  $435.5 \text{ nm}$  light for the excitation of the clock transition in the two trap systems. Two additional AOMs allow independent frequency tuning of the probe laser frequencies for the two trap systems. For the clock transition, Fourier limited linewidths of the excitation spectra down to  $10 \text{ Hz}$  were so far demonstrated in the experiment with this setup for both trap systems [54] (see also Sec. 5.3.3). The long-term linear frequency drift of the laser is about  $-0.16 \text{ Hz/s}$  at  $435.5 \text{ nm}$ .



## 4.3 Fluorescence Detection

The fluorescence light of the ion induced by the cooling laser is imaged by a combination of a doublet lens, a single lens, and a pivoting mirror onto either a photomultiplier or an intensified CCD camera. The image on the CCD camera is used to monitor the position of the ion during the compensation of the electric stray field (see Sec. 3.4). The spatial resolution of the imaging system is about  $2 \mu\text{m}$  and is about the same for both trap setups. The photomultiplier signal allows an efficient determination of the total fluorescence rate with a high time resolution. For a laser cooled ion the observed count rates are about 30 kHz on resonance for a saturation parameter of  $s = 1$ . Typical count rates for spectroscopy are about 18 kHz on resonance. The stray light from the lasers contributes about 100 Hz to the count rate, while the ambient light plus the dark counts of the photomultiplier contribute about 30 Hz.

# Chapter 5

## Interrogation of the 436 nm Reference Transition

### 5.1 Interrogation Sequence

Fig. 5.1 shows the experimental sequence that is employed to obtain an excitation spectrum of the  ${}^2S_{1/2}(F=0) \rightarrow {}^2D_{3/2}(F=2)$  resonance by an optical double resonance scheme. During steps (1) and (2), the ion is laser cooled for typically  $t_d + t_c = 20$  ms and the induced fluorescence light is detected by a photomultiplier. Typical fluorescence count rates at the halfpoint of the cooling resonance are 9 kHz, with a background count rate of 130 Hz. Then, the repumper sideband of the cooling laser is switched off. Within a time  $t_{hf} = 20$  ms, the ion will be transferred with high probability to the  ${}^2S_{1/2}(F=0)$  ground state via nonresonant excitation to the  ${}^2P_{1/2}(F=1)$  state and the fluorescence signal will disappear (step (3)). The cooling and repumper lasers are then blocked by mechanical shutters and the magnetic field is switched from the high bias field  $B_c \sim 400 \mu\text{T}$  needed for cooling to a field  $B_p \sim 1 \mu\text{T}$  for spectroscopy. After a waiting time of about 10 ms which ensures that the magnetic field has settled to its new value, a pulse of length  $t_p$  from the probe laser is applied (step (4)). As long as  $1/t_p$  is larger than the natural linewidth of the atomic transition,  $t_p$  determines via the Fourier transformation the frequency resolution of the resonance signal, while the laser intensity and the detuning from resonance determine the effective Rabi frequency for the excitation. The cooling and repumper lasers are switched on again about 3 ms after the end of the probe pulse, ensuring that the interrogation is not disturbed by stray light. The state of the ion is detected by the so-called electron shelving method proposed by H. Dehmelt [23, 24]. If the ion is still in the ground state after the excitation attempt, the fluorescence signal will reappear immediately, while if no significant signal is detected for a time  $t_d = 4$  ms in step (1), the ion was with high probability excited to the

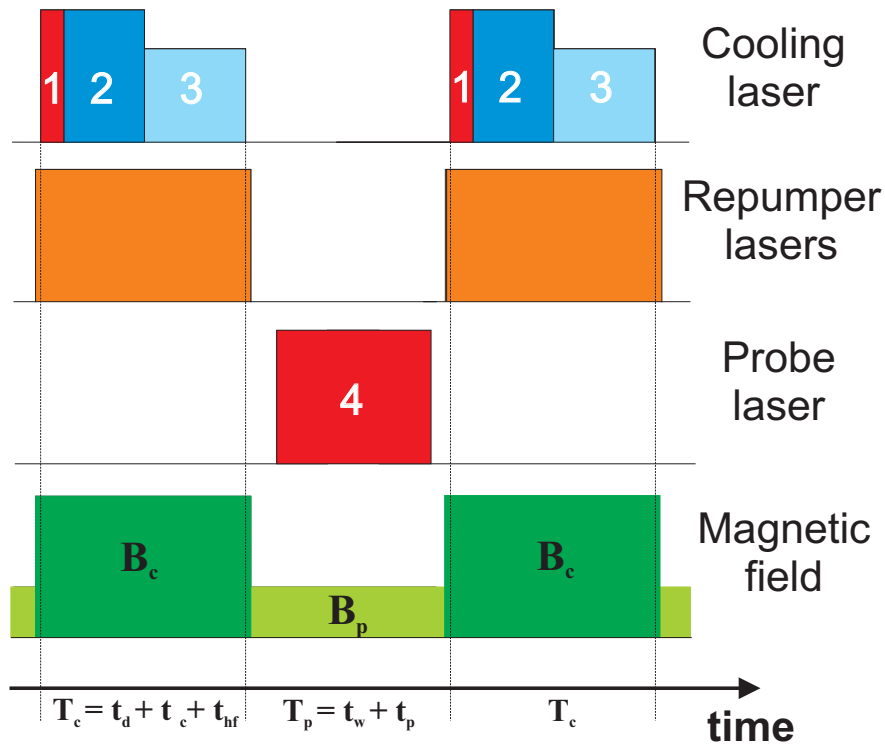


Figure 5.1: Time sequence for the interrogation of the clock transition. The individual steps are: (1) State detection of the ion by the electron shelving method during time  $t_d$ , (2) laser cooling for time  $t_c$ , (3) preparation of the ion in the  $^2S_{1/2}(F = 0)$  state by switching off the repumper sideband of the cooling laser and waiting for a time  $t_{hf}$ , and (4) excitation of the clock transition by a probe laser pulse of length  $t_p$ .

$^2D_{3/2}(F = 2)$  state. The sequence of steps (1) to (4) is repeated several times at a given frequency of the probe laser. The excitation probability at this frequency is then given by the ratio of the detected excitations to the total number of valid excitation attempts. In order to qualify as valid, the sequence (1) to (3) prior to the probe pulse has to fulfill three requirements: (i) the average fluorescence rate during step (2) has to be above a threshold of 6 kHz, (ii) the average fluorescence rate during step (3) has to be below the threshold of 6 kHz and (iii) no significant fluorescence rate is detected during the last 2 ms of  $t_{hf}$ . Condition (i) ensures that the ion was in the  $F = 1$  ground state during the cooling step and was cooled to low temperatures, while conditions (ii) and (iii) make sure that the ion was in the  $F = 0$  ground state when the probe laser pulse was applied. As can be seen from Fig. 5.1, the repumper lasers and the magnetic field are switched off (on) a little bit later (earlier) than the cooling laser. This ensures that any dark times observed at the beginning of step (1) are due to an excitation to the

$^2D_{3/2}$  state while dark times at the end of step (3) are not due to an excitation of the ion from the ground state to states that do not interact with the probe laser. If an excitation attempt is found to be invalid, it is repeated. To record an excitation spectrum, steps (1) to (4) are typically repeated until a number of 20 valid excitations is reached. The number of invalid excitations depends on the detuning of the probe laser, the probe pulse duration, and the maximum excitation probability. The main reason for invalid excitations is that the ion remains in the excited state during the whole cooling interval  $t_c$  with some probability. The ratio of invalid to valid excitations ranges from about 0.05 far from the resonance to 0.5 in the center of a 1 kHz resonance. The excitation spectrum of the atomic transition is obtained by repeating the procedure described above for different probe laser frequencies. Spectra taken for different frequency resolutions and ranges of probe laser frequencies will be discussed in the following section.

Excitation spectra of the atomic transition can also be obtained using Ramsey’s method of separated oscillatory fields [122] instead of the single-pulse excitation scheme described above. For the single-ion experiments described in this work it offers no distinct advantage compared to the single-pulse scheme (with one exception that will be discussed in Sec. 6.1), so no description of Ramsey’s method is given here. A detailed description of the method is given in [122] and a typical Ramsey spectrum for the clock transition is shown in Sec. 5.3.3.

## 5.2 Quantum Projection Noise

The use of a single ion instead of an ensemble of ions limits the signal-to-noise ratio of the spectroscopic signal. While the electron shelving method allows to detect the state of the ion after an interrogation by the probe laser with near 100% efficiency, still only one “bit” of information is gained from each interrogation and therefore the ion has to be interrogated many times in order to obtain reliable information about the excitation probability. During a probe pulse the ion is prepared in a superposition  $|\psi\rangle = \alpha|g\rangle + \beta|e\rangle$  of the ground state  $|g\rangle$  and the excited state  $|e\rangle$  ( $|\alpha|^2 + |\beta|^2 = 1$ ). The following state detection is described by a projection operator  $\hat{P} = |e\rangle\langle e|$ , with eigenvalues 0 (ion in the ground state) and 1 (ion in the excited state). With the relation  $\hat{P}\hat{P}^T = \hat{P}$  and the definition  $p \equiv |\beta|^2$  for the probability the ion being in the excited state, one finds that the variance of the projection operator in the state  $|\psi\rangle$  is given by

$$(\Delta\hat{P})^2 = \langle\hat{P}^2\rangle - \langle\hat{P}\rangle^2 = p(1-p). \quad (5.1)$$

The observed population fluctuations described by Eq. (5.1) and their relevance in atomic frequency standards were first discussed by W. Itano et al., who named the phenomenon quantum projection noise (QPN) [123]. The signal-to-noise ratio

for the interrogation of a single ion can be defined as

$$SNR = \frac{\langle \hat{P} \rangle}{\Delta \hat{P}} = \frac{p}{\sqrt{p(1-p)}}. \quad (5.2)$$

From Eq. (5.1) one finds that the QPN is zero if the ion is in an eigenstate of  $\hat{P}$ , that is for  $p \in \{0, 1\}$ . The signal-to-noise ratio is in these cases no meaningful quantity. For a symmetric superposition of ground and excited state,  $p = 0.5$  and the QPN has its maximum. The result of a sequence of interrogations is then a random sequence of zeros and ones and the corresponding signal-to-noise ratio is  $SNR = 1$ . The signal-to-noise ratio of the average over a sequence of  $N$  independent interrogations is  $\sqrt{N} \cdot SNR$ . This means that for the interrogation of both single particles as well as of ensembles of particles, the signal-to-noise ratio increases proportionally to the square root of the averaging time and that the signal-to-noise ratio in the ensemble case increases also with the square root of the number of particles (see also Sec. 2.1).

## 5.3 Spectra

The excitation spectra of the  ${}^2S_{1/2}(F=0) \rightarrow {}^2D_{3/2}(F=2)$  transition obtained by the methods discussed in the previous section consist of several resonances that contain information not only about the internal state of the trapped ion, but also about its motion and interactions with the environment. In the following sections the individual components of the excitation spectrum and their relevance for the experiment will be discussed.

### 5.3.1 Secular and Micromotion Sidebands

The secular motion and micromotion of the ion in the trap potential lead to sidebands in the excitation spectrum at the secular frequencies and at the trap drive frequency. The relative intensities of these sidebands with respect to the carrier contain information on the amount of excess micromotion and on the temperature of the secular motion. Moreover, the frequency splitting of the radial secular sidebands is a measure for the deviation of the trap potential from cylindrical symmetry.

Fig. 5.2 shows a spectrum of the carrier frequency and of the low-frequency secular sidebands for one of the traps. The angle between the  $\mathbf{k}$ -vector of the probe laser and the trap axis was  $\theta \simeq 55^\circ$ . The relative intensities of the sidebands are  $I_x^-/I_0 = I_y^-/I_0 \simeq 0.14(3)$  and  $I_z^-/I_0 \simeq 0.015(3)$ , which is within the uncertainty

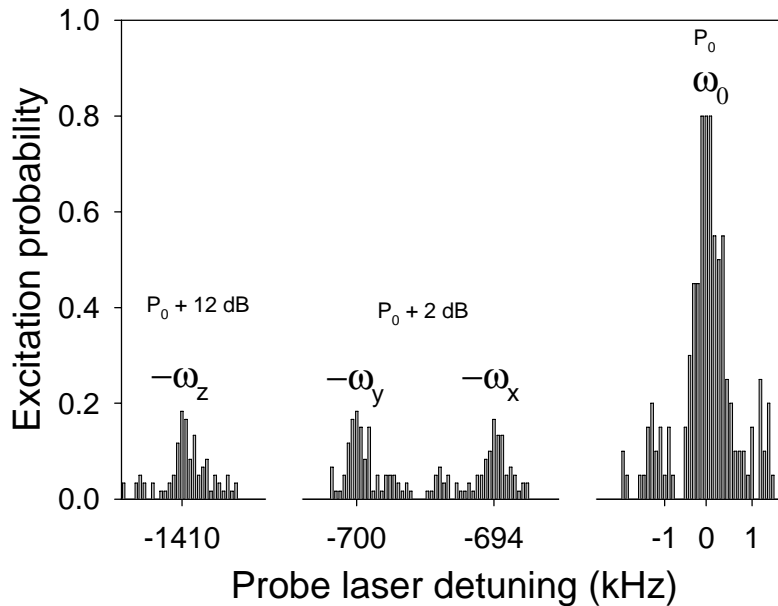


Figure 5.2: Secular sidebands of the clock transition at the Doppler limit. The duration of the probe laser pulses was 1 ms and every data point is the average over 20 interrogations. For better visibility the laser power for the excitation of the sidebands was increased by 2 dB for  $\omega_x$ ,  $\omega_y$  and by 12 dB for  $\omega_z$  with respect to the carrier.

in good agreement with the expected relative intensities of the sidebands at the Doppler cooling limit calculated from Eq. (3.27).

From the splitting of the radial secular frequencies one finds that the deviation of the trap potential from cylindrical symmetry is less than 1%. Aside from an intrinsic asymmetry of the trap potential due to the finite precision in the manufacturing of the electrodes, also the gradient of an electric stray field would lift the degeneracy of the radial secular frequencies. In Sec. 7.4.2 this will be used to estimate the magnitude of the electric stray field gradient at the position of the ion.

Fig. 5.3 shows the first low-frequency sideband in the spectrum of the clock transition due to the micromotion of the ion in the trap. The relative intensity of the sideband with respect to the carrier is only about 1%, indicating a good compensation of the electric stray field.

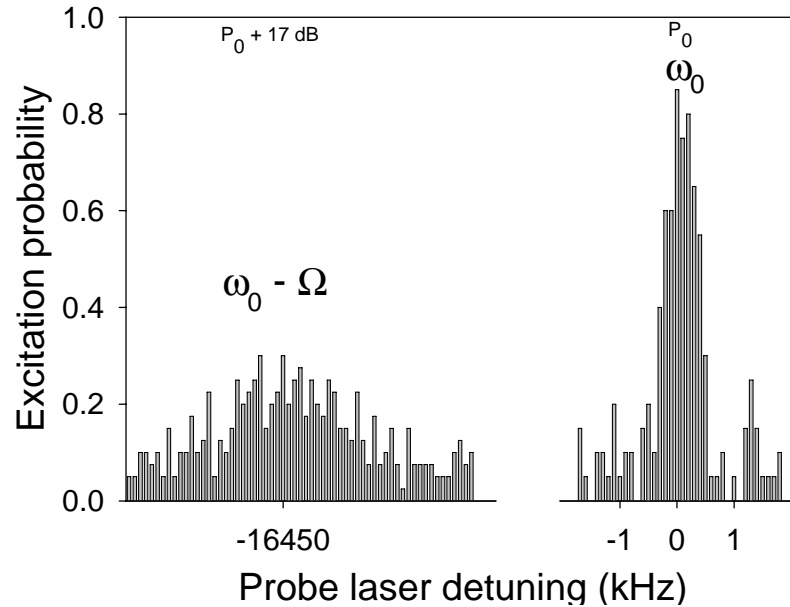


Figure 5.3: First low-frequency micromotion sideband of the clock transition at the trap frequency  $\Omega$  for a good compensation of the electric stray field. The duration of the probe laser pulses was 1 ms and every data point is the average over 20 interrogations for the carrier and 40 interrogations for the sideband. The laser power for the excitation of the sideband was increased by 17 dB with respect to the carrier.

### 5.3.2 Zeeman Structure

The static magnetic field applied during the excitation of the  $^2S_{1/2}(F=0) \rightarrow ^2D_{3/2}(F=2)$  transition leads to a frequency splitting of the five  $m_F$  sublevels of the  $^2D_{3/2}(F=2)$  state by the linear Zeeman effect (see Sec. 7.2). Fig. 5.4 shows an example of a Zeeman spectrum for  $|\mathbf{B}| \simeq 1 \mu\text{T}$ . From the frequency splitting of the Zeeman components, one can according to Eq. (7.7) determine the absolute value of the magnetic field, while the relative intensities of the individual Zeeman components provide information about the orientation of the magnetic field with respect to the probe laser beam. The relative intensities of the Zeeman components are given by [97, 124]

$$\begin{aligned}
 I_{\pm\Delta m_F} &\propto R_{|\Delta m_F|} \begin{pmatrix} 2 & 2 & 0 \\ \Delta m_F & -\Delta m_F & 0 \end{pmatrix}^2, \quad m_F = -2, \dots, 2 \quad (5.3) \\
 R_0 &= 6 \sin^2 \theta \cos^2 \theta \cos^2 \phi, \\
 R_1 &= \cos^2 \phi (\sin^2 \theta - \cos^2 \theta)^2 + \sin^2 \phi \cos^2 \theta, \\
 R_2 &= \sin^2 \theta (\cos^2 \theta \cos^2 \phi + \sin^2 \phi),
 \end{aligned}$$

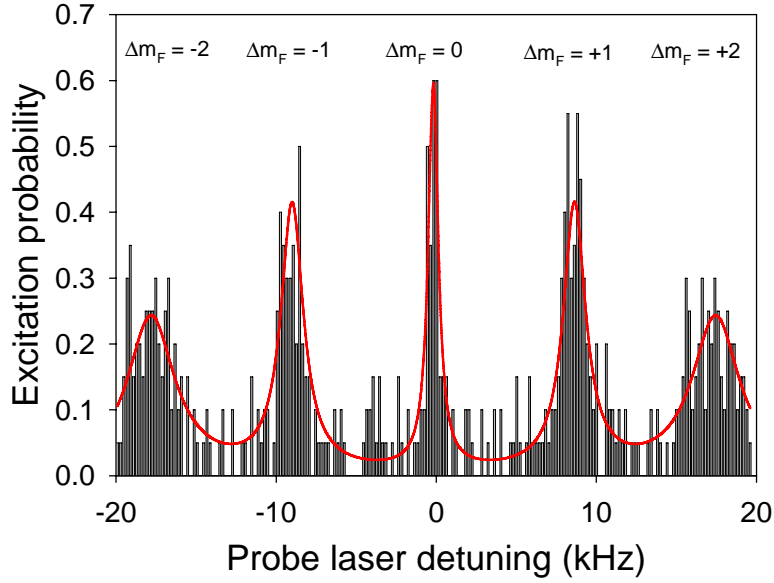


Figure 5.4: Zeeman pattern of the  ${}^2S_{1/2}(F=0) \rightarrow {}^2D_{3/2}(F=2)$  transition for  $|\mathbf{B}| \simeq 1 \mu\text{T}$  and a linear polarization of the probe laser that achieves nonvanishing excitation rates for all  $\Delta m_F$  components. The length of the probe laser pulses was 1 ms and every data point is the average over 20 interrogations. The red line is a fit of five Lorentz profiles to the data. The  $\Delta m_F = \pm 1$  and  $\Delta m_F = \pm 2$  are broadened due to 50 Hz magnetic stray fields

where  $\theta$  is the angle between the  $\mathbf{k}$ -vector of the probe laser beam and the magnetic field  $\mathbf{B}$  and  $\phi$  is the angle between the polarization vector and its projection onto the  $(\mathbf{k}, \mathbf{B})$ -plane. Because there is only the  $m_{F'} = 0$  Zeeman sublevel in the ground state,  $\Delta m_F = m_F - m_{F'} = m_F$ .

The angles  $\theta$ ,  $\phi$  can be determined (up to the ambiguities due to the  $\cos^2$  dependence) by comparing Zeeman spectra for different orientations of the laser polarization with the theory given by Eq. (5.3). The angle  $\phi$  is most easily determined from the intensity of the carrier  $R_0$ , while the ratio  $R_1/R_2$  is well suited to determine  $\theta$ . The precision of this method depends on the signal-to-noise ratio of the Zeeman spectra, on the quality of the fits to the line profiles of the Zeeman components, and on the number of spectra used. Uncertainties below  $\pm 1^\circ$  are easily achievable for  $\phi$  since only the minimum of  $R_0$  has to be identified. For  $\theta$  it is very time consuming to achieve similar uncertainties due to the low signal-to-noise ratio of the signal from the single ion. Typical uncertainties are about  $\pm 5^\circ$  for  $\theta$ . Especially for the investigation of the quadrupole shift described in Sec. 7.4, one wants to implement a set of three mutually orthogonal magnetic field axes. This was also done by the method described above. Because the



procedure of determining the orientations of the magnetic field axes takes very long, the axes were aligned approximately once every month with a  $\pm 5^\circ$  precision. Since no magnetic shielding was used, the orientations of the magnetic field axes can change by a few degrees between alignments. Thus for the experiments described in Sec. 7.4 the uncertainty in the orientation of the magnetic field was conservatively estimated as  $\pm 10^\circ$  for one trap system and  $\pm 20^\circ$  for the other trap system, where only less precise measurements of the magnetic field orientations were performed.

The  $\Delta m_F \neq 0$  resonances in Fig. 5.4 are significantly broadened due to 50 Hz magnetic stray fields. From the broadening it is estimated that the mean amplitude of the total stray field is smaller than  $0.3 \mu\text{T}$ . The  $\Delta m_F = 0$  Zeeman component is subject only to the second-order Zeeman shift and is therefore well suited as a reference transition for an atomic frequency standard.

### 5.3.3 $\Delta m_F = 0$ Clock Transition

Fig. 5.5 shows three excitation spectra of the  $^2S_{1/2}(F=0, m_F=0) \rightarrow ^2D_{3/2}(F=2, m_F=0)$  clock transition which in this work is used as the reference transition for the  $^{171}\text{Yb}^+$  single-ion optical frequency standard.

For 1 ms excitation pulses, excitation probabilities of 0.9 are typically achieved and the linewidth is Fourier limited. Here, the probe pulse duration  $t_p$  is small compared to the waiting time  $t$  between the end of the probe pulse and the state detection. The maximum excitation probability  $p_{max}$  is limited by the natural lifetime  $\tau$  of the excited state and by the waiting time  $t$  according to  $p_{max} \propto e^{-t/\tau}$ . Due to the finite lifetime of the  $^2D_{3/2}$  state, the maximum excitation probability decreases further for longer excitation pulses as can be seen in Fig. 5.5(b) and Fig. 5.5(c). The corresponding reduction in the signal-to-noise ratio of the resonance is a limiting factor for the stability of the frequency standard. In Sec. 6.1 it will be shown that therefore the optimum stability for the single pulse excitation is obtained for approximately 10 Hz resonances, and not for 3.1 Hz which is for the single-pulse excitation the limit set by the natural linewidth of the clock transition. The present resolution limit is about 10 Hz (Fig. 5.5(c)). The linewidth is still essentially Fourier limited, but contributions of laser noise to the line profile are no longer negligible, which can indirectly be seen also from the stability measurements shown in Sec. 6.2. Because of the low signal-to-noise ratio and the decreasing excitation probability, the averaging time needed to obtain good spectra increases for longer probe times. Since higher resolutions also offer no advantages for the operation of the frequency standard, no efforts were made so far to increase the frequency resolution beyond 10 Hz.

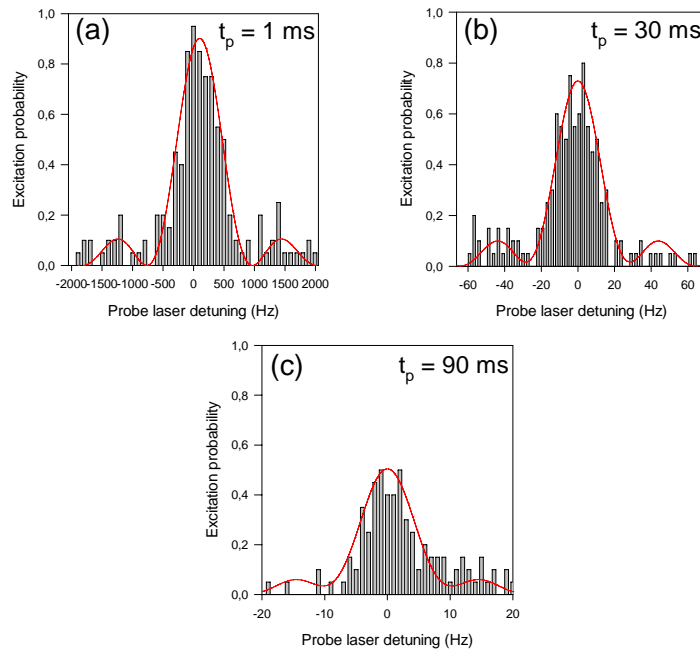


Figure 5.5: Excitation spectra of the clock transition for different durations  $t_p$  of the probe laser pulse. Every data point is the average over 20 interrogations. The laser power was adjusted for maximum excitation probability on resonance. (a)  $t_p = 1$  ms, maximum excitation probability close to one. (b)  $t_p = 30$  ms, typical resolution used for trap comparison experiments. (c)  $t_p = 90$  ms, present resolution limit. The red curves are numerical solutions of the Bloch equations for the experimental parameters.

Fig. 5.6 shows an excitation spectrum of the clock transition obtained by Ramsey's method of separated oscillatory fields. The two pulses had a length of 5 ms and were separated by 30 ms. The spectral width of the envelope of the Ramsey pattern is determined by the duration of the single pulses, while the width of the individual fringes is determined by the pulse separation. Because of the more detailed structure it takes significantly more time to record a full spectrum of the clock transition with a good signal-to-noise ratio than with the single-pulse excitation.

## 5.4 Laser Frequency Lock

In order to realize an atomic frequency standard based on the  $^2S_{1/2}(F=0, m_F=0) \rightarrow ^2D_{3/2}(F=2, m_F=0)$  clock transition as a frequency reference, the probe laser frequency has to be stabilized by a servo

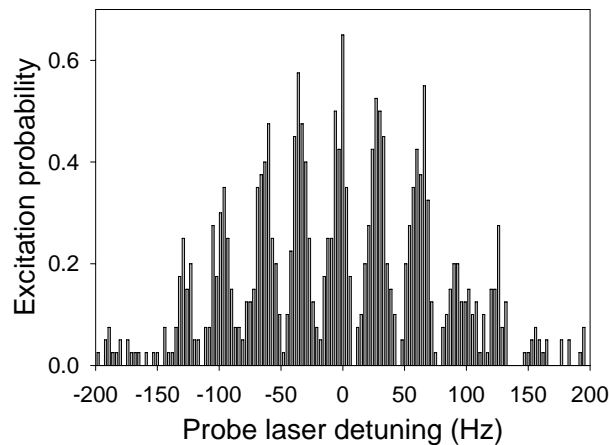


Figure 5.6: Ramsey spectrum of the clock transition for two 5 ms probe laser pulses separated by 30 ms. Every data point is the average over 40 interrogations.

system to the atomic transition frequency. The servo algorithm used in the experiment and its dynamic properties are described in the following.

Before the laser frequency  $\omega_L$  is stabilized to the atomic resonance frequency  $\omega_0$ , an excitation spectrum of the resonance is recorded, and the laser frequency is set close to the center of the resonance. In order to obtain an error signal for the frequency servo, a series of interrogations of the ion at frequencies  $f_+ = \omega_L + \delta$  and  $f_- = \omega_L - \delta$  is performed and the number of successful excitations  $n_+$  at  $f_+$  and  $n_-$  at  $f_-$  is counted. After  $z$  pairs of interrogations, a frequency correction is calculated as

$$e = g \cdot \delta \cdot \frac{n_+ - n_-}{z} \equiv g \cdot \delta \cdot s, \quad (5.4)$$

where  $g$  is a numerical factor that determines the dynamical response of the servo system which will be named gain for short and  $s$  will be referred to as the cycle error. The laser frequency is shifted from  $\omega_L$  to  $\omega_L + e$  and a new sequence of  $z$  interrogation pairs is started. Since the frequency corrections calculated for subsequent excitation pairs are added up, this scheme realizes an integrating servo loop.

Due to invalid excitation attempts during the sequence, the valid excitation attempts at  $f_+$  and  $f_-$  do not always form pairs. Unpaired excitations do not contribute to the error signal, even if they were successful. Fig. 5.7 shows schematically the interrogation sequence for  $z = 4$ .

It can be shown that the best value for  $\delta$  is close to  $\Gamma/2$  which corresponds to the half linewidth of the atomic resonance [125]. There the slope of the resonance and thus the sensitivity to frequency fluctuations is close to its maximum. The time constant and the stability of the servo system are determined by the parameters

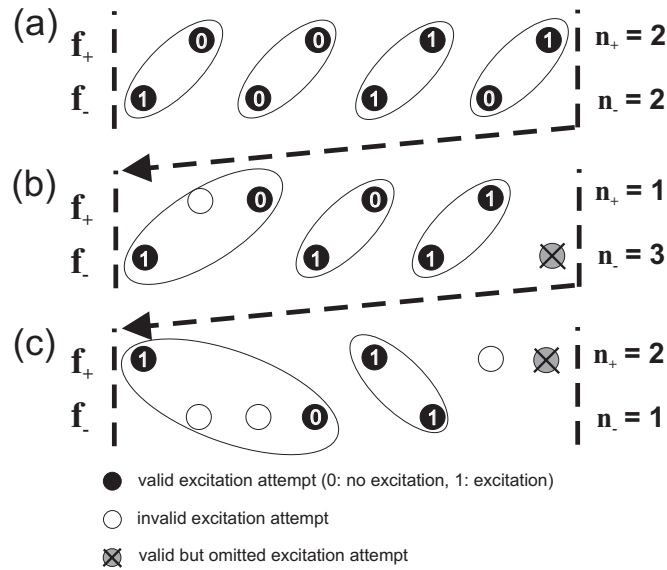


Figure 5.7: Interrogation scheme for the laser frequency lock to the clock transition. The probe laser frequency is periodically switched between the half points of the atomic resonance  $f_-$  and  $f_+$  unless an invalid excitation attempt occurs. After typically eight excitation attempts an error signal that is proportional to  $n_+ - n_-$  is calculated from the valid pairs of excitation attempts. (a) All excitation attempts are valid. (b) One invalid excitation attempt. Although valid, the last excitation attempt does not contribute to the error signal because it can not form a pair. (c) Three invalid excitation attempts. The error signal is calculated from only two pairs and again one valid excitation attempt has to be omitted.

$g$  and  $z$  and by the time  $T = T_c + T_p$  required for one interrogation of the ion (see Fig. 5.1). If the laser frequency is initially  $\omega_L = \omega_0 - \Gamma/2$ , and if the maximum excitation probability is unity, the resulting value of  $s$  will be close to  $\Gamma/2$ . The appropriate frequency correction  $e$  for the correction of the laser frequency in one step will be obtained for  $g \simeq 1$ . If  $g \ll 1$ , many correction steps will be required to bring  $\omega_L$  close to  $\omega_0$ . If  $g \geq 2$ , the servo may cause the value of  $e$  to jump irregularly between large positive and negative values and the laser frequency  $\omega_L$  will not settle at a value close to resonance. For a high number of interrogation pairs  $z$  the time constant of the servo is increased and its ability to cope with fast frequency fluctuations will be reduced. On the other hand, if  $z$  is small the short-term stability of the system may be degraded by strong fluctuations in  $s$  due to quantum projection noise. In order to find the optimum servo parameters for a given frequency resolution of the clock transition numerical Monte Carlo simulations of the servo action were performed [125] (see also Sec. 6.1). For a 30 Hz resonance with a maximum excitation probability of 0.6 and a total interrogation time  $T = 90$  ms, the typical parameters chosen for the experiments

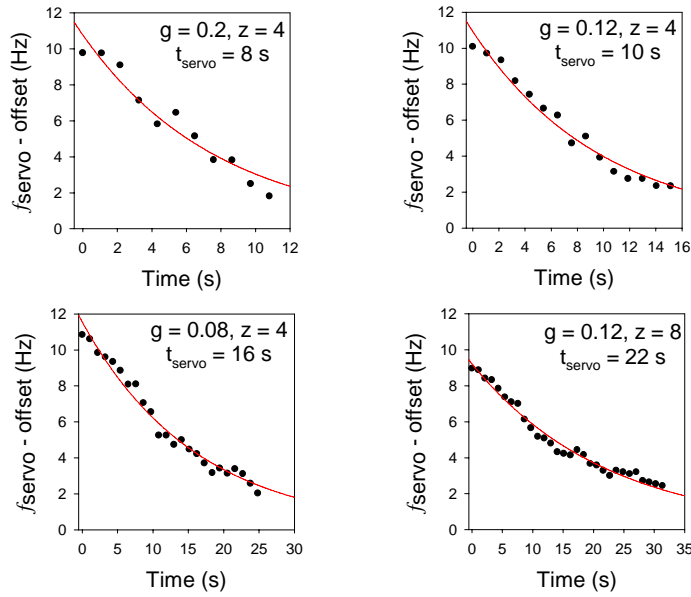


Figure 5.8: Response of the servo system to an applied 10 Hz frequency step for different values of the gain  $g$  and number of interrogation pairs  $z$ . The clock transition was interrogated with 30 ms pulses, the maximum excitation probability was about 0.6 and the frequency modulation was  $\delta = 13$  Hz. The total time for one interrogation of the ion was  $T = 90$  ms. The solid lines are exponential fits to the data.

are  $g \simeq 0.2$  and  $z = 4$ . Fig. 5.8 shows the response of the servo system to an externally applied frequency step for different values of  $g$  and  $z$ .

The relatively long time constant of the servo may lead to a significant servo error if the laser frequency is subject to drift. The linear long-term frequency drift of the probe laser is about  $-0.16$  Hz/s, but laser drift rates between  $0.1$  Hz/s and  $-0.3$  Hz/s were observed on the time scale of hours. From numerical simulations the resulting servo error was found to be equal to the product of the response time of the servo and the frequency drift rate. An efficient reduction of the drift induced servo error is obtained with the use of a second-order integrating servo. Periodically after a time  $t_{drift} = 1$  s a drift correction  $e_d$  is applied to the laser frequency:

$$\omega_L \mapsto \omega_L + e_d. \quad (5.5)$$

The drift correction  $e_d$  itself is adjusted after a time  $T_{drift} \simeq 10$  s via the integration

$$e_d \mapsto e_d + k \sum_{T_{drift}} s. \quad (5.6)$$

The sum is over the cycle errors  $s$  obtained during the drift update interval  $T_{drift}$ ,

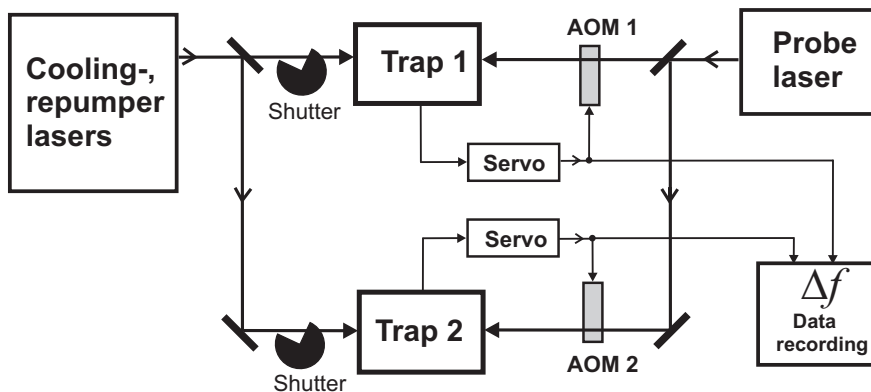


Figure 5.9: Schematic of the experimental setup used to compare two  $^{171}\text{Yb}^+$  optical frequency standards. Two acousto-optical modulators (AOM) are used to independently shift the frequencies of the two probe beams interacting with the ions. Mechanical shutters block the cooling and repumper lasers while the probe beams interrogate the ions.

which is large compared to the time  $t_{drift}$  between two drift corrections and the time required to obtain a single cycle error  $s$ . The parameter  $k$  determines the time constant for the response of the servo to changes of the laser frequency drift. A typical value in the experiment is  $k = 0.005$ , corresponding to a time constant of a few hundred seconds. The second-order integrating servo described above compensates a linear drift for long averaging times. This was confirmed by numerical simulations of the servo action including the second-order drift correction and a linear laser frequency drift. To within the statistical uncertainty of the simulations no residual frequency error of the servo was found in the long-term average.

## 5.5 Frequency Comparisons Between Two Trap Systems

Studies of the systematic frequency shifts of an optical frequency standard by measurements of its frequency relative to established microwave standards are inherently limited by the instabilities and uncertainties of the latter. These limitations can be overcome by comparing the optical frequency standard with a second one. In the experiments described in this work the two optical frequency standards that are compared are realized by the frequencies of two probe laser beams that are individually frequency stabilized to the clock transitions of two single ions stored in two separate traps. The schematic setup for the frequency comparison is shown in Fig. 5.9. Because both traps share the 369.5 nm cooling

laser, the time intervals for cooling and detection of the ions coincide for the two systems. Two independent frequency shift and servo systems are employed to stabilize the probe beam frequencies to the line centers of the clock transitions of the two trapped ions by the method described in Sec. 5.4. The length of the probe pulses interrogating the ions and the position of the pulses in the time interval between the cooling and detection intervals can be chosen independently for both trap systems. For times larger than the servo time constants, the optical frequencies probing the two ions can be regarded as independent and determined solely by the respective atomic transition frequencies. The frequencies of the two servos  $f(\text{AOM1})$  and  $f(\text{AOM2})$  are recorded separately for both trap systems and the frequency difference between the two servos  $\Delta f = f(\text{AOM2}) - f(\text{AOM1})$  is recorded once per second and averaged for typically 500 – 700 s. Trap comparison experiments were used to investigate the stability of the  $^{171}\text{Yb}^+$  single-ion optical frequency standard (Sec. 6.2) and some of the systematic frequency shifts (Sec. 7.3, Sec. 7.4, Sec. 7.8).

# Chapter 6

## Instability of the $^{171}\text{Yb}^+$ Single-Ion Frequency Standard

### 6.1 Theory

In Sec. 2.1, the Allan deviation was introduced as a measure for the instability of a frequency standard. In the case of a frequency standard that is operated in interrogation cycles of duration  $T$ , the Allan deviation  $\sigma_y(t)$  for an averaging time  $t$  can be written as [125]

$$\sigma_y(t) = \frac{C}{SNR} \frac{\Delta\omega}{\omega_0} \sqrt{\frac{T}{t}}, \quad (6.1)$$

where  $C$  is a numerical constant of order unity that depends on the interrogation scheme,  $\Delta\omega$  is the width of the resonance signal used as the reference for the standard and  $SNR$  is the signal-to-noise ratio for a single interrogation. Parameters that are obtainable with present single-ion optical frequency standards are on the order of  $\Delta\omega/\omega_0 \sim 10^{-15}$  [41, 47, 54]. The signal-to-noise ratio for a single particle is limited by quantum projection noise to  $SNR \simeq 1$  (see Sec.5.2). The potential relative systematic uncertainties of single-ion optical frequency standards are expected to be in the range of  $10^{-18}$  [24, 126]. For  $C/SNR = 1$ , a continuous averaging time of nearly 12 days would be necessary to complete one single frequency measurement at this accuracy. In order to be able to use the potential accuracies of single-ion standards, it is therefore important to find operation parameters that minimize the instability of the standard.

Theoretical studies of the instability properties of single-ion frequency standards were performed recently by several groups [125, 127, 128]. A detailed investigation of the instability of the  $^{171}\text{Yb}^+$  single-ion optical frequency standard and an



optimization of the locking algorithm introduced in Sec. 5.4 is discussed in [125]. The relevant results derived there are summarized in the following.

The optimization of the instability can be separated into two steps: (i) Determine the optimum interrogation scheme and the corresponding frequency modulation  $\delta$  for the locking algorithm and (ii) find the parameters  $g$  and  $z$  that minimize the instability for the optimum interrogation scheme. The two excitation schemes that were investigated are the single-pulse excitation described in Sec. 5.1 and the two-pulse Ramsey excitation. The Allan deviation for the two excitation schemes can be written as

$$\sigma_y(t) = S \frac{1}{\omega_0 \tau} \sqrt{\frac{\tau}{t}}, \quad (6.2)$$

where  $\tau = 1/\Gamma$  is the inverse of the natural decay rate of the atomic transition and  $S$  is a dimensionless instability parameter that depends on the excitation scheme.

For the single pulse excitation, numerical simulations showed that the optimum frequency modulation  $\delta$  is always close to the half linewidth of the transition and the instability parameter is in this case given by

$$S = S_1 = \sqrt{\frac{1}{2}p_{max}(1 - \frac{1}{2}p_{max})} \frac{\Delta\omega\tau}{p_{max}} \sqrt{\frac{T}{\tau}}. \quad (6.3)$$

Here  $p_{max}$  is the maximum excitation probability that can be obtained on resonance and  $\Delta\omega$  is the full linewidth at half maximum of the resonance signal, which depends on the probe pulse duration  $t_p$  and on the Rabi frequency  $\Omega_R$ . The time between two probe pulses  $t_0 = T - t_p$  is the so-called dead time of the interrogation sequence. For the case of negligible laser linewidth and  $t_0 \ll t_p$ , a numerical search for the minima of  $S_1$  with respect to  $t_p$  and  $\Omega_R$  yields  $S_1^{min} = 3.22$  for  $t_p = 1.88\tau$  and  $\Omega_R = 2.02\Gamma$ . The corresponding width of the resonance signal is about 10 Hz for the clock transition, which is larger than the natural linewidth of 3.1 Hz. This means that the loss in the signal-to-noise ratio due to the decrease of the maximum excitation probability  $p_{max}$  outweighs for long probe pulse durations the gain in frequency resolution  $\Delta\omega$ . The minimum instability according to Eq. (6.2) is  $\sigma_y(t) \simeq 3.3 \cdot 10^{-15} t^{-\frac{1}{2}}$  for averaging times longer than the servo time constant.

In the case of Ramsey excitation the optimum frequency modulation  $\delta$  is always exactly the half linewidth of the Ramsey fringes and the instability parameter is given by

$$S = S_2 = \sqrt{\bar{p}(1 - \bar{p})} \frac{\Delta\omega\tau}{p_{max} - p_{min}} \sqrt{\frac{T}{\tau}}, \quad (6.4)$$

where  $p_{max}$  and  $p_{min}$  are the maximum and minimum excitation probabilities of the Ramsey fringes,  $\bar{p} = (p_{max} + p_{min})/2$  is the average excitation probability, and

$\Delta\omega$  is here the full fringe width. The optimum obtained here is  $S_2^{\text{min}} = 2.59 \simeq 0.8S_1^{\text{min}}$  for  $t_p = 1.00\tau$ , where for Ramsey excitation  $\tau$  is the time separation of the two pulses. The optimum Rabi frequency for the two pulses is that which yields  $\pi/2$ -pulses. The corresponding minimum instability is  $\sigma_y(t) \simeq 2.7 \cdot 10^{-15} t^{-\frac{1}{2}}$ .

Comparing the two interrogation schemes one finds that the Ramsey excitation leads to an approximately 20% lower instability than the single-pulse excitation in the limit of negligible laser linewidth and dead time. The difference becomes less pronounced if a finite laser linewidth  $\gamma_L \leq \Gamma/(2\pi)$  and the typical cycle dead time  $t_0 \simeq 60$  ms are taken into account.

In both Eq. (6.3) and Eq. (6.4) a linear approximation for the slope of the resonance signal was used in order to derive a simple analytic expression for  $S$ . Numerical calculations show, that approximately 30% lower instabilities than predicted by the analytic expressions should be achievable with both excitation schemes. The occurrence of invalid interrogation attempts (see Sec. 5.1, Sec. 5.4) effectively reduces the information that is obtained in one sequence of  $z$  interrogation pairs. The instability as well as the response time of the servo increase proportionally to the ratio of invalid excitations to the total number of excitation attempts for both excitation schemes.

A general disadvantage of Ramsey excitation is that the servo system must be able to distinguish between the different Ramsey fringes because otherwise the servo system will stabilize the laser frequency to different fringes if frequency fluctuations larger than the fringe width occur. In the experiments, the single-pulse scheme described in Sec. 5.1 and Sec. 5.4 is used.

In the second step of the optimization, numerical Monte Carlo simulations of the servo action were performed. The result found in [125] is that small values of  $z$  should be chosen in order to achieve a short response time of the servo system and that values of the gain in the range  $0.1 < g < 1$  will provide the best overall stability, depending on the amount of laser frequency noise.

## 6.2 Comparison with the Experiment

Fig. 6.1 shows the Allan deviation for the difference frequency between the two ytterbium frequency standards obtained in two frequency comparisons. For the comparison in Fig. 6.1(a), the two standards were operated with probe pulses of duration  $t_p = 30$  ms, a modulation frequency  $\delta = 13$  Hz, and a servo gain  $g = 0.2$ . The number of excitation pairs was  $z = 4$  for one servo and  $z = 5$  for the other, and the maximum excitation probabilities were about 0.6. The red curves are the result of numerical Monte Carlo simulations of the servo action that assume a monochromatic laser excitation and include quantum projection

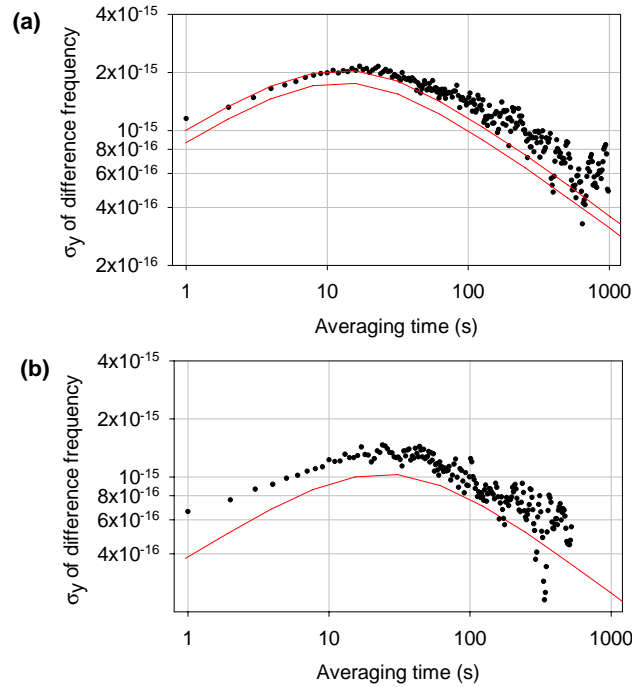


Figure 6.1: Allan deviation of the frequency difference between two ytterbium frequency standards. (a) Probe pulse duration 30 ms, maximum excitation probability 0.6,  $g = 0.2$ ,  $\delta = 13$  Hz and  $z = 4$  for one servo,  $z = 5$  for the other servo. The red lines are numerical simulation of the servo action that assume a monochromatic laser excitation and QPN as the only source of noise. The two curves represent the uncertainty range of the simulation due to the uncertainties of the experimental parameters. (b) Probe pulse duration 90 ms, maximum excitation probability 0.4,  $g = 0.4$ ,  $\delta = 4$  Hz and  $z = 5$ . The red curve is again a numerical simulation.

noise as the only source of noise. The simulations account for a dead time of 60 ms and an average percentage of invalid interrogations of 20%. Because some experimental parameters like the average excitation probability and the average number of invalid excitations are known only with a finite precision of a few percent, simulations were done for a worst case (upper curve) and best case (lower curve) estimate of the experimental parameters. The difference between the two curves is also a measure for the sensitivity of the simulation to the input parameters. For the worst case estimate, the maximum excitation probability and the number of invalid excitations was 10% lower than for the best case estimate. This leads to a difference between the simulated instabilities of about 10%.

The occurrence of invalid excitations effectively reduces the information that is obtained in one sequence of  $z$  interrogation pairs. Therefore the instabil-

ity as well as the response time of the servo increase proportionally to the ratio of invalid excitations to the total number of excitation attempts. For averaging times  $> 80$  s, the instability of the frequency difference scales approximately as  $\sigma_y(t) \simeq 1.1 \cdot 10^{-14} t^{-\frac{1}{2}}$ . Under the assumption that both standards contribute equally to the instability, this corresponds to an instability of  $\sigma_y(t) \simeq 7.8 \cdot 10^{-15} t^{-\frac{1}{2}}$  for the individual standards. This is less than a factor 3 above the instability limit derived for the single-pulse excitation in the previous section. The agreement with the simulation is good for short averaging times, while for the longest averaging times an excess instability of about 20% with respect to the lower curve is found.

Fig. 6.1(b) shows the Allan deviation for a similar comparison measurement with  $t_p = 90$  ms,  $\delta = 4$  Hz,  $g = 0.4$ ,  $z = 5$ , and a maximum excitation probability of about 0.4. Here an excess noise of about 50% above the simulation for the QPN limit is observed in the experimental data. Here, only a simulation for the nominal values of the experimental parameters is shown. At the frequency resolution of this measurement, frequency fluctuations of the laser not included in the simulation are probably no longer negligible and may degrade the stability of the standards. Also, the finite kinetic temperature of the ion may lead to small variations in the spectral lineshape and thus to uncorrelated fluctuations of the excitation rate for the two standards.

In further experiments it was found that the instability of the frequency difference does not depend on the temporal overlap of the probe pulses interrogating the two ions, which confirms the assumption that the two frequency standards can be regarded as independent even though the laser frequencies interrogating the two ions are derived from the same probe laser.

The instability of the standards can be improved further by reducing the dead time and the percentage of invalid excitations. In order to reduce the dead time, it would be useful to prepare the ion in the  $F=0$  ground state by an additional laser frequency that is resonant with the  $^2S_{1/2}(F=1) \rightarrow ^2P_{1/2}(F=1)$  transition rather than by waiting until non resonant excitation by the cooling laser transfers the ion to the  $F=0$  ground state. Also the time for the switching of the magnetic field can be reduced, so that dead times of 20-30 ms seem achievable. If an successful excitation to the metastable  $^2D_{3/2}(F=2)$  state is detected at the beginning of the cooling phase, the 935.2 nm repumper laser could be tuned to the  $^2D_{3/2}(F=2) \rightarrow ^3[3/2]_{1/2}(F=1)$  in order to rapidly deplete the metastable state which would reduce the percentage of invalid excitations.

## 6.3 Dick Effect

The time sequence for the interrogation of a single ion always includes dead times for laser cooling and state preparation. The interrogation is therefore always discontinuous and periodic. This can lead to a degradation of the stability by down-conversion of laser frequency noise around harmonics of the interrogation repetition frequency  $1/T$ . This effect was first described by G. J. Dick [129] and further investigations are presented in [130–132]. For a precise calculation of the effect, the noise spectrum of the laser would have to be known. Although this is not the case for the probe laser used in the experiment, an estimate of the limiting instability for the single-pulse excitation scheme can be obtained from [129]:

$$\sigma_y^{min} \simeq \frac{\sigma_y^{LO}}{2 \ln 2} \sqrt{\frac{T}{t}} \frac{1}{g_0^2} \sum_{n=1}^{\infty} \frac{g_n^2}{n} \equiv R \sigma_y^{LO} \sqrt{\frac{T}{t}}, \quad (6.5)$$

where  $\sigma_y^{LO}$  is the flicker-floor instability of the probe laser and the functions  $g_n$  defined as

$$g_n = \int_0^T g(\tau) \cos\left(\frac{2\pi n\tau}{T}\right) d\tau \quad (6.6)$$

are the Fourier coefficients of the function  $g(\tau)$  that describes the sensitivity of the excitation scheme to frequency fluctuations at the time  $\tau$  of the interrogation pulse of duration  $t_p$ . The ratio  $R$  is calculated in [129] for various duty cycles  $t_p/T$  of the interrogation. For the typical value in the experiment  $t_p/T \simeq 0.6$ , one finds  $R \simeq 0.6$ . Values for the flicker-floor instability of lasers used in other single ion experiments are  $\sigma_y^{LO} \simeq 5 \cdot 10^{-16}$  [133] leading to a limiting instability  $\sigma_y^{min} \simeq 3 \cdot 10^{-16} \sqrt{T/t}$ . This is about one order of magnitude below the QPN-limited instability calculated in Sec. 6.1 above. The situation is different for optical frequency standards using ensembles of atoms, for which QPN-limited instabilities on the order of  $\sigma_y = 10^{-17} \sqrt{T/t}$  are expected so that the Dick effect will become important.

# Chapter 7

## Systematic Frequency Shifts

### 7.1 Doppler Effect

The motion of the ion in the trap leads to a Doppler shift of the atomic transition frequency. The shift of the frequency  $\nu$  observed in the laboratory frame of reference relative to the frequency  $\nu_0$  in the rest frame of the ion is given by

$$\frac{\Delta\nu_D}{\nu_0} = \frac{\nu - \nu_0}{\nu_0} = -\cos\theta\frac{v}{c} - \frac{v^2}{2c^2} + O\left(\left(\frac{v}{c}\right)^3\right), \quad (7.1)$$

where  $v$  is the absolute value of the instantaneous velocity of the ion relative to the laboratory frame,  $c$  is the speed of light, and  $\theta$  is the angle of observation. The term linear in  $v/c$  is the classical linear Doppler effect, while the second-order term is due to relativistic time dilation. Eq. (7.1) accounts only for velocity-dependent relativistic effects. The influence of general relativistic effects due to gravity on the frequency of the clock transition are discussed in Sec.7.5. If the motion of the ion is cooled to the Lamb-Dicke regime, the first-order term leads to discrete sidebands in the excitation spectrum of the atomic transition, while the carrier frequency is subject only to the second-order Doppler shift. For the trapping parameters used in the experiment, the time needed to interrogate the clock transition is much larger than one oscillation period of either the secular motion or the micromotion of the ion. Thus one can replace  $v^2$  in the above equation by the mean square velocity of the ion. The properties of secular and micromotion are quite different and therefore their contributions to the second-order Doppler shift will be treated separately.

The secular motion is a thermal motion and the corresponding effective temperature  $T_D$  at the Doppler cooling limit is given by Eq. (3.25). Since the secular motion is thermal,  $T_D$  is the same for all directions of motion. For the clock

transition the fractional second order Doppler shift is then [111]

$$\frac{\Delta\nu_D}{\nu_0} = -3 \frac{k_B T_D}{2mc^2} \simeq -3 \cdot 10^{-19}, \quad (7.2)$$

where  $k_B$  is Boltzmann's constant and  $m$  is the restmass of the ion.

If the ion is displaced from the field-free saddle point of the trap potential, it undergoes excess micromotion as described in Sec. 3.4. Even in the absence of an electric stray field, micromotion does not completely vanish because the finite temperature of the secular motion leads to excursions of the ion from the trap center. In contrast to the secular motion, micromotion is a driven motion at the frequency of the rf trapping field. When the secular motion is cooled to the Doppler limit, the fractional second order Doppler shift of the clock transition due to micromotion is [111]

$$\frac{\Delta\nu_D}{\nu_0} \simeq -\frac{1}{mc^2} \sum_{i=x,y,z} \frac{k_B T_D (a_i + q_i^2)}{2a_i + q_i^2} + \frac{4}{m} \left( \frac{eq_i E_i}{(2a_i + q_i^2)\Omega} \right)^2, \quad (7.3)$$

where  $e$  is the elementary charge,  $\Omega \simeq 2\pi \cdot 16$  MHz is the trap drive frequency, and  $a_i, q_i$  are the  $a$ - and  $q$ -parameters defined in sec. 3.1. For normal operating conditions,  $a_i = 0$ . The  $E_i$  are the uncompensated components of the static electric stray field that were estimated in Sec. 3.4. The second-order Doppler shift due to micromotion is then  $\Delta\nu_D \simeq -2.6$  mHz, corresponding to a fractional frequency shift of about  $-3.8 \cdot 10^{-18}$ .

Combining the above estimates for the secular motion and micromotion, one finds that the second-order Doppler shift contributes about  $4.1 \cdot 10^{-18}$  to the relative systematic uncertainty of the frequency standard.

## 7.2 Zeeman Effect

The interaction of the ion with an external magnetic field splits the hyperfine states into several discrete sublevels. The energies of these sublevels are determined by the Zeeman Hamiltonian

$$H_Z = -\boldsymbol{\mu} \cdot \mathbf{H} = g_J \mu_B \mathbf{J} \cdot \mathbf{B} + g'_I \mu_B \mathbf{I} \cdot \mathbf{B}, \quad (7.4)$$

which depends on the electronic  $g$ -factor  $g_J$  of the atomic state, the nuclear  $g$ -factor  $g'_I$  which is the nuclear moment expressed in units of the Bohr magneton  $\mu_B$ , the total electronic angular momentum  $\mathbf{J}$ , the nuclear spin  $\mathbf{I}$ , and the external magnetic field  $\mathbf{B} = B\mathbf{e}_z$  that defines the  $z$ -axis of the laboratory frame of reference. Since for the magnetic fields applied in the experiment the Zeeman interaction is always weak compared to the hyperfine interaction,  $H_Z$  can

be diagonalized in the same basis of states  $|\gamma J F m\rangle$  as the hyperfine interaction. Here  $J$  is the total electronic angular momentum,  $F$  is the total atomic angular momentum including nuclear spin,  $m$  is the eigenvalue of  $F_z$ , and  $\gamma$  represents all other quantum numbers characterizing the atomic state. In order to find the Zeeman energy shift of the ytterbium clock transition, the matrix elements of  $H_Z$  have to be calculated for the  $^2S_{1/2}(F=0)$  and the  $^2D_{3/2}(F=2)$  state. The electronic  $g$ -factors for the two states are  $g_S = g_J(S_{1/2}) = 1.998$  and  $g_D = g_J(D_{3/2}) = 0.802^1$  [134]. Because the nuclear  $g$ -factor  $g_I' \simeq 0.9 \cdot 10^{-3}$  is small compared to the uncertainty of the electronic  $g$ -factors, the nuclear part of the Zeeman Hamiltonian can be neglected without increasing the uncertainty of the calculation. The matrix elements of  $J_z$  are [124]

$$\langle \gamma J F m | J_z | \gamma J F' m \rangle = (-1)^{F-m} (\gamma J F || J_z || \gamma J F') \begin{pmatrix} F & 1 & F' \\ -m & 0 & m \end{pmatrix}, \quad (7.5)$$

with the reduced matrix element

$$(\gamma J F || J_z || \gamma J F') = (-1)^{I+J+F+1} \sqrt{J(J+1)(2J+1)(2F+1)(2F'+1)} \times \begin{Bmatrix} F & 1 & F' \\ F' & J & 1 \end{Bmatrix}. \quad (7.6)$$

The frequency shift of the  $^2S_{1/2}(F=0, m=0) \rightarrow ^2D_{3/2}(F=2, m)$  transition depends on  $m$ . The  $m \neq 0$  transitions are subject to the linear Zeeman effect given by

$$\Delta\nu_Z^{(1)} = \frac{g_D \mu_B B}{h} \langle D 3/2 2 0 | J_z | D 3/2 2 0 \rangle \simeq m \cdot 8.4 \frac{\text{kHz}}{\mu\text{T}}, \quad (7.7)$$

while the  $m=0$  transition is affected by the quadratic Zeeman effect which is given by

$$\nu_Z^{(2)}(D, 3/2, 2, 0) - \nu_Z^{(2)}(S, 1/2, 0, 0) = \frac{\mu_B^2 B^2}{4h^2} \left( \frac{g_D^2}{\Delta_{D_{3/2}}} + \frac{g_S^2}{\Delta_{S_{1/2}}} \right) \simeq 52 \frac{\text{mHz}}{\mu\text{T}^2}, \quad (7.8)$$

$$\nu_Z^{(2)}(\gamma, J, F, m) = \frac{\mu_B B^2}{h} \sum_{F' \neq F} \frac{|\langle \gamma J F m | J_z | \gamma J F' m \rangle|^2}{E_F - E_{F'}}. \quad (7.9)$$

Here  $\Delta_{S_{1/2}} = 12.64$  GHz and  $\Delta_{D_{3/2}} = 0.86$  GHz are the hyperfine splitting frequencies of the ground state and of the excited state from Table 3.1. For the magnetic fields  $B < 10 \mu\text{T}$  that are typically applied in the experiments, higher order contributions to the Zeeman shift are negligible.

---

<sup>1</sup>In the case of  $g_D$ , the experimental value listed in [134] is 1.802, the calculated one is 0.800. Since the difference between theory and experiment for other states is typically only a few percent, Fawcett and Wilson suggest that the experimental value is almost certainly a missprint for the value 0.802.



The linear Zeeman shift of the clock transition is zero and the quadratic Zeeman shift can be calculated from Eq. (7.8), where  $B$  is determined from the frequency splitting of the  $m \neq 0$  linear Zeeman components of the  $^2S_{1/2}(F=0) \rightarrow ^2D_{3/2}(F=2)$  transition. This splitting can easily be measured with a relative uncertainty of 1% and the calculated second-order shift can then be applied as a correction to the frequency of the clock transition with a relative uncertainty of about 2%. Contributions to the uncertainty from the  $g$ -factors and hyperfine splittings can be neglected. At  $B = 1 \mu\text{T}$ , the contribution of the quadratic Zeeman effect to the systematic uncertainty of the frequency standard is about 1 mHz, corresponding to a relative frequency uncertainty of  $1.5 \cdot 10^{-18}$ . Static magnetic fields below  $0.3 \mu\text{T}$  can be achieved in the experiment, but since in the present state of the experiment no magnetic shielding around the trap is installed, these low static magnetic fields are not very stable in amplitude or direction. The latter is especially troublesome, because the optimum laser power for the excitation of the clock transition then varies unpredictably over time, which leads to a decrease of the maximum excitation probability. Also for the investigation and reduction of other systematic shifts like the quadratic Stark shift (Sec. 7.3) and the quadrupole shift (Sec. 7.4) a good pointing stability of the applied magnetic field is required. Thus, in the experiments magnetic fields with  $B = 1 - 3 \mu\text{T}$  were applied, for which the relative change of  $\mathbf{B}$  during the time of the experiments was found to be negligible.

Another source of a quadratic Zeeman shift is the time dependent magnetic field emitted by electronic devices near the trap which typically oscillates at a frequency of 50 Hz. These field leads to an observable broadening of the  $m \neq 0$  transitions from which one can estimate that the mean amplitude of the field is  $\bar{B} < 0.3 \mu\text{T}$  (see Sec. 5.3.2). This leads to a contribution to the systematic frequency uncertainty of about 5 mHz, which will be difficult to reduce without magnetic shielding. Similar values for  $\bar{B}$  were also measured with magnetic-field sensors placed close to the trap.

The magnetic field associated with the thermal radiation emitted by the experimental apparatus also gives rise to a quadratic Zeeman shift of the clock transition, which is the the magnetic counterpart of the blackbody AC Stark shift discussed below in Sec. 7.3.2. To account for the time and frequency dependence of the blackbody field, Eq. (7.9) is written as

$$\nu_Z^{(2)}(\gamma, J, F, m) = \frac{\mu_B}{h^2} \sum_{F' \neq F} |\langle \gamma J F m | J_z | \gamma J F' m \rangle|^2 \int_0^\infty \frac{B^2(\nu) \nu_{FF'}}{\nu_{FF'}^2 - \nu^2} d\nu, \quad (7.10)$$

where  $B^2(\nu)$  is the spectral distribution of  $B$  given by Planck's law and  $\nu_{FF'} = \nu_F - \nu_{F'}$  is the frequency difference between the states with energies  $E_F$  and  $E_{F'}$ . For  $B^2(\nu) = B^2 \delta(\nu_0)$  and  $\nu_0 \mapsto 0$  Eq. (7.10), is with identical Eq. (7.9). The magnetic blackbody field at  $T = 300$  K has its maximum at a frequency

$\nu_{max} \simeq 3.1 \cdot 10^{13}$  Hz and a mean amplitude  $\bar{B}^2 \simeq 2.8 \mu\text{T}$ . The frequency  $\nu_{max}$  is much larger than the relevant hyperfine splittings. In order to derive an estimate for the blackbody Zeeman shift it is therefore reasonable to make the approximations  $B^2(\nu) = \bar{B}^2 \delta(\nu - \nu_{max})$  and  $\nu_{FF'}/(\nu_{FF'}^2 - \nu_{max}^2) \simeq -\nu_{FF'}/\nu_{max}^2$  leading to

$$\nu_Z^{(2)}(\gamma, J, F, m) \simeq \frac{\mu_B \bar{B}^2}{h^2} \sum_{F' \neq F} \frac{|\langle \gamma J F m | J_z | \gamma J F' m \rangle|^2 \nu_{FF'}}{\nu_{max}^2}. \quad (7.11)$$

Comparing the above equation to Eq. (7.9) one sees, that the static quadratic Zeeman shift for  $B = 1 \mu\text{T}$  is larger than the blackbody Zeeman shift by approximately  $|(2.8)^2 \nu_{max}^2 / \nu_{FF'}^2| > 60$ . This means that the blackbody Zeeman shift does contribute less than 1 mHz to the systematic frequency uncertainty of the frequency standard.

### 7.3 Quadratic Stark Effect

In Sec. 3.4 it was shown that in the presence of a static electric stray field the ion in the trap no longer oscillates around the field free saddle point of the trap potential, which leads to the appearance of excess micromotion. The interaction of the atomic dipole moment with the square of the electric field at the position of the ion gives rise to a quadratic Stark shift of the atomic energy levels. The Stark Hamiltonian is

$$H_S = -\mathbf{d} \cdot \mathbf{E}, \quad (7.12)$$

where  $\mathbf{d}$  is the electric dipole moment operator and  $\mathbf{E}$  is the electric field, which in general will be time dependent. In the following the interaction with static or time-averaged electric fields is discussed. Further it is assumed that the Stark interaction is weak compared to the Zeeman interaction and therefore can be diagonalized separately in the same basis as the Zeeman Hamiltonian. Some aspects of the interaction with time-dependent fields are discussed in Sec. 7.3.2 and Sec. 7.3.3.

The theory of the quadratic Stark effect is described in detail in [135, 136] and the relevant formulas are summarized in Appendix A. For the clock transition Eq. (A.3) gives

$$h\Delta\nu_S = (2\Delta\alpha_S + \alpha_T (3 \cos^2 \beta - 1)) \frac{E^2}{4}, \quad (7.13)$$

where  $\Delta\alpha_S = \alpha_S(S, 1/2) - \alpha_S(D, 3/2)$  is the difference of the scalar electric polarizabilities of the ground state and of the  ${}^2D_{3/2}$  state,  $\alpha_T = \alpha_T(D, 3/2)$  is the tensor polarizability of the  ${}^2D_{3/2}$  state,  $E$  is the absolute value of the electric field, and  $\beta$  is the angle between the electric and the static magnetic field defining the quantization axis. The electric polarizabilities can be calculated using

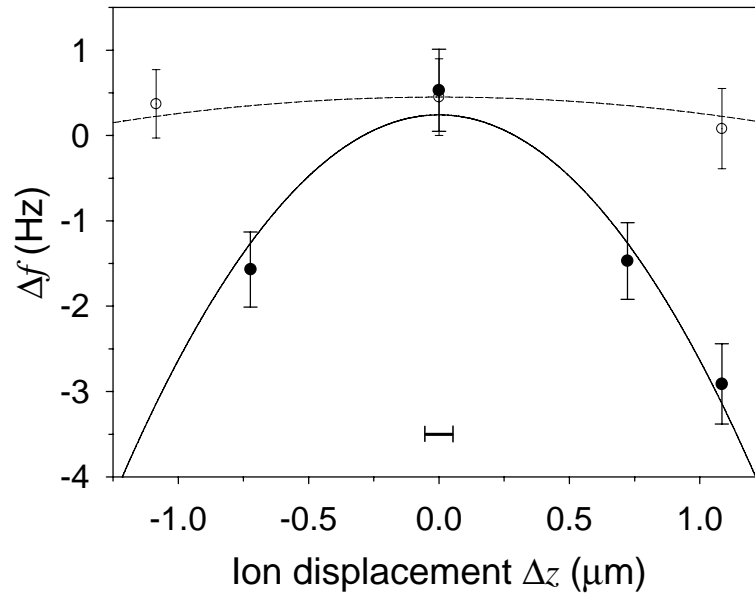


Figure 7.1: Quadratic Stark shift as a function of the displacement  $\Delta z$  of the ion from the saddle point of the quadrupole trap potential for  $\beta = 32^\circ$  (solid circles) and  $\beta = 90^\circ$  (open circles).  $\Delta z$  was calculated from the voltage applied between the trap endcaps. The lines are least-squares fits of parabolas centered at  $\Delta z = 0$ . The horizontal bar in the lower part represents the uncertainty range of the position  $\Delta z = 0$  which remains after the compensation of the electric stray field.

the formulas in Appendix A from oscillator strength data, but the precision of the calculation will be limited by the amount of available oscillator strengths so that the uncertainty of the obtained polarizabilities is difficult to estimate. It is therefore useful to determine the relevant polarizabilities also experimentally.

### 7.3.1 Measurement of the Scalar and Tensor Electric Polarizabilities

To measure the polarizabilities, one of the ions in the two traps was displaced by a distance  $\Delta z$  from the trap center by adding a variable offset to the compensation voltage applied between the endcap electrodes of the trap [67]. The ion is then subject to the quadratic Stark shift caused by the time average of the AC trapping field at the position  $\Delta z$ . The corresponding frequency shift of the clock transition is measured relative to the unperturbed ion in the other trap. The quantities  $\Delta\alpha_S$  and  $\alpha_T$  can be determined from at least two measurements with different angles  $\beta$ . Fig. 7.1 shows the dependence of  $\Delta f$  on the displacement  $\Delta z$  for a

magnetic field orientation with  $\beta = 32(3)^\circ$ . The angle  $\beta$  was determined using a measurement of an induced quadrupole shift as described later in Sec. 7.4. The data points taken at  $\Delta z = \pm 0.7 \mu\text{m}$  and  $\Delta z = 1.1 \mu\text{m}$  include corrections for the quadratic Zeeman effect as well as for the respective calculated second-order Doppler shifts of  $-0.16 \text{ Hz}$  and  $-0.35 \text{ Hz}$ , respectively that arises from the excess micromotion related to the displacements. The differential voltage between the endcap electrodes also leads to a small electric field gradient of about  $4.4 \cdot 10^{-4} \text{ V/mm}^2$  at the position of the ion. The corresponding quadrupole shift (see Sec. 7.4) of about  $1.2 \text{ mHz}$  is negligible for the Stark shift measurement. A second Stark shift measurement was done for a magnetic field orientation with  $\beta = 90(5)^\circ$ . Here no significant shifts were observed, indicating an accidental cancellation of the scalar and tensorial contributions to the Stark shift at this angle. Combining these measurements,  $\Delta\alpha_S = -6.9(1.4) \times 10^{-40} \text{ Jm}^2/\text{V}^2$  and  $\alpha_T(D_{3/2}) = -13.6(2.2) \times 10^{-40} \text{ Jm}^2/\text{V}^2$  is obtained. The uncertainties include contributions from the statistical uncertainty of the data, the uncertainties of the angles  $\beta$  and from a 5% uncertainty in the determination of  $E^2$ . The experimental result is close to values calculated from available oscillator strength data [99,137],  $\Delta\alpha_S = -4.4 \times 10^{-40} \text{ Jm}^2/\text{V}^2$  [138] and  $\alpha_T = -11.5 \times 10^{-40} \text{ Jm}^2/\text{V}^2$ .

For optimum compensation of the electric stray field, it was found in Sec. 3.4 that at the position of the ion the components of the time-averaged square of the trapping field including the contributions due to the secular motion are  $E_r^2 \simeq E_z^2 \leq 6000 \text{ V}^2/\text{m}^2$ . From Eq. (7.13) it follows that if  $E_r \leq E_z$ , the quadratic Stark shift of the clock transition is maximal for  $\beta \in \{0, \pi\}$ , that is for  $E_r = 0$  ( $\tan \beta = E_r/E_z$  since  $E_z$  is parallel to the trap axis). This yields an upper limit for the quadratic Stark shift of  $|\Delta\nu_S| \leq |(\Delta\alpha_S + \alpha_T)E_z^2/2h| \leq 7 \text{ mHz}$ , corresponding to a fractional frequency shift of about  $1 \cdot 10^{-17}$ .

### 7.3.2 Blackbody AC Stark Shift

The electric field associated with thermal radiation emitted by the experimental apparatus also gives rise to a quadratic Stark shift of the clock transition, the so-called blackbody AC Stark shift. To good approximation the thermal radiation is isotropic and its spectral energy density is given by Planck's law:

$$u_\lambda(T) = \frac{8\pi hc}{\lambda^5} \frac{1}{e^{\frac{hc}{\lambda k_B T}} - 1}. \quad (7.14)$$

At  $T = 300 \text{ K}$ , according to Wien's law the wavelength corresponding to the maximum of  $u_\lambda(T)$  is  $\lambda_0 \simeq 9.7 \mu\text{m}$ . This is large compared to the transition wavelengths in  $^{171}\text{Yb}^+$ , where the longest relevant transition wavelength is at about  $2.4 \mu\text{m}$  [138]. In a static approximation the blackbody AC Stark shift can therefore be calculated using the polarizabilities measured with the trap field

and replacing  $E$  by the RMS amplitude of the blackbody radiation electric field  $E_{BB}(T)$ , defined by

$$\epsilon_0 E_{BB}^2(T) = \int_0^\infty u_\lambda(T) d\lambda = \frac{8\pi^5(kT)^4}{15(ch)^3} = \epsilon_0 \cdot \left(831.95 \frac{\text{V}}{\text{m}}\right)^2 \left(\frac{T}{300 \text{ K}}\right)^4, \quad (7.15)$$

where  $\epsilon_0$  is the electric constant. As the blackbody radiation is isotropic, the tensor part of the blackbody AC Stark shift vanishes and the shift of the clock transition at the typical laboratory temperature  $T \simeq 297 \text{ K}$  is

$$\Delta\nu_{BB} \simeq \frac{\Delta\alpha_S}{2h} E_{BB}^2(297\text{K}) \simeq -0.35(0.07) \text{ Hz}. \quad (7.16)$$

The uncertainty is determined by the uncertainty of the experimental value of  $\Delta\alpha_S$ . The above calculation neglects the frequency dependence and also a possible anisotropy of the blackbody radiation field. The latter is expected to be negligible since the trap is surrounded by a closed metal box without internal heat sources. More rigorous calculations of the blackbody shift that take the wavelength dependence of  $u_\lambda(T)$  into account predict a frequency shift that is about 10% larger than the one calculated from Eq. (7.16) [138, 139] (see also Appendix A). The polarizabilities calculated there are different from the ones measured in the experiment described above. To avoid confusion, the polarizabilities for the static case discussed above will be referred to as static polarizabilities, while the ones accounting also for the any frequency dependence of  $E$  will be referred to as dynamic polarizabilities. The uncertainty in the measurement of the static polarizabilities (see Sec. 7.3.1 above) can easily be reduced below 10% by increasing the averaging time and the number of displacements for which the shift is measured. Assuming that the temperature of the environment can be controlled to within  $\pm 1 \text{ K}$ , which leads to an additional 5 mHz uncertainty in  $\Delta\nu_{BB}$ , the total uncertainty due to the blackbody AC Stark shift would then be about 40 mHz. This corresponds to a fractional frequency uncertainty of  $6 \cdot 10^{-17}$ , which would then be limited by the approximations that lead to Eq. (7.16). In order to reduce the uncertainty in the blackbody AC Stark shift below the 10% level, either more precise theoretical calculations or direct measurements of the blackbody AC Stark shift must be done. As far as the calculations are concerned, more precise measurements of the static polarizabilities will also help to get a better measure of the slight discrepancy between experiment and theory suggested by the measurement of the static polarizabilities. A direct measurement of the blackbody shift with the necessary precision by deterministically heating or cooling the apparatus would require major changes of the experimental setup. Another option would be to permanently cool the environment of the ion to lower temperatures. As  $\Delta\nu_{BB} \sim T^4$ , the shift will be greatly reduced even for moderate cooling. Going for example from room temperature ( $T \simeq 300 \text{ K}$ ) to the temperature of liquid nitrogen ( $T \simeq 80 \text{ K}$ ) would reduce the shift to about 2 mHz. With decreasing

temperature also the mean frequency of the electric blackbody field decreases and therefore the theoretical predictions made by Eq. (7.16) based on the measured static polarizabilities become more reliable.

### 7.3.3 Light Shift

Another electric field that may give rise to a quadratic Stark shift is the electric field of the probe laser interrogating the ion. This so called light shift is proportional to the intensity of the incident light  $I_L = c\epsilon_0\bar{E}^2$ . Here  $E^2$  is the square of the electric field of the laser averaged over one oscillation period. The light shift due to the dipole coupling of the ground state and of the  ${}^2D_{3/2}(F=2)$  state to other states by the probe laser can then be estimated from

$$\Delta\nu_L \leq (\Delta\alpha_S^{AC} + \alpha_T^{AC})\frac{I}{2hc\epsilon_0}. \quad (7.17)$$

this equation corresponds to Eq. (7.13), where the static polarizabilities are replaced by the dynamic polarizabilities calculated in Appendix A, and  $E^2$  is expressed in terms of the laser intensity  $I_L$ . Typical laser powers employed to obtain spectra with a 30 Hz linewidth are on the order of 1 nW and the waist diameter of the laser focus is about 50  $\mu\text{m}$ , leading to intensities of about 0.5 W/m<sup>2</sup>. The relative frequency shift of the clock transition is then calculated to be  $3.6 \cdot 10^{-19}$ , which is negligible.

Another contribution to the light shift could arise from nonresonant coupling of the  ${}^2S_{1/2}(F=1)$  state to the  ${}^2D_{3/2}(F=2)$  state by the probe laser. In the dressed-atom picture the corresponding frequency shift of the clock transition is approximately given by [140]

$$\Delta\nu \sim K \frac{\Omega_R^2}{2\Delta_L} \sim 1 \cdot 10^{-9} \text{ Hz}, \quad (7.18)$$

where  $\Omega_R$  is the resonant Rabi frequency for the  ${}^2S_{1/2}(F=1) \rightarrow {}^2D_{3/2}(F=2)$  transition,  $\Delta_L$  is the detuning of the probe laser from resonance, and  $K$  is a numerical factor of order unity that depends on the quantum numbers of the involved states.

The cooling and repumper lasers are blocked by mechanical shutters during the interrogation of the ion by the clock laser. A variation of the powers of the cooling and repumper lasers did not lead to any measurable frequency shift in the trap comparison experiments, confirming the correct operation of the mechanical shutters.

## 7.4 Quadrupole Shift

Aside from the interaction with the external electric field described in the previous section, there is also an interaction of the ion with the gradient of the electric field. While the electric field couples to lowest order to the atomic electric dipole moment, the gradient couples to the atomic electric quadrupole moment. The resulting energy shift is called quadrupole shift. It has so far been the limiting systematic uncertainty for most single-ion frequency standards. In the case of the ytterbium clock transition, only the  $^2D_{3/2}$  state is shifted since the  $^2S_{1/2}$  state has spherical symmetry and therefore no quadrupole moment.

The Hamilton operator describing the interaction of an external field gradient with the atomic quadrupole moment of a given state is [136]

$$H_Q = \nabla \mathbf{E}^{(2)} \cdot \Theta^{(2)} = \sum_{q=-2}^2 (-1)^q \nabla E_q^{(2)} \Theta_{-q}^{(2)}. \quad (7.19)$$

Here  $\nabla \mathbf{E}^{(2)}$  is a symmetric traceless second-rank tensor describing the electric field gradient at the position of the ion and  $\Theta^{(2)}$  is the electric-quadrupole operator for the atom. The definitions of the tensor components  $\nabla E_q^{(2)}$  and  $\Theta_q^{(2)}$  are given in Appendix B. In general  $\nabla \mathbf{E}^{(2)}$  has five independent components, but there exists always a coordinate transformation to a reference frame where  $\nabla \mathbf{E}^{(2)}$  is diagonal. In this so called principal axis frame denoted  $\{x', y', z'\}$ ,  $\nabla \mathbf{E}^{(2)}$  has only two independent components due to the constraint  $Tr(\nabla \mathbf{E}^{(2)}) = 0$ , which is the Laplace equation. If it is further assumed that the electric field gradient is constant over the area of motion of the ion, the electric field gradient in the principal axis frame can be written as

$$\nabla \mathbf{E}^{(2)'} = 2A \begin{pmatrix} 1 + \epsilon & 0 & 0 \\ 0 & 1 - \epsilon & 0 \\ 0 & 0 & -2 \end{pmatrix}, \quad (7.20)$$

and the corresponding electric potential in the vicinity of the ion has the simple form

$$\Phi = A \left( (1 + \epsilon)x'^2 + (1 - \epsilon)y'^2 - 2z'^2 \right). \quad (7.21)$$

The parameter  $A$  is a measure for the strength of the potential and  $\epsilon$  describes the deviation of the potential from cylindrical symmetry.

The general formulas for the first- and second-order quadrupole shift are derived in Appendix B. A general discussion of higher order quadrupole shifts can be found for example in [141]. For the  $^2D_{3/2}(F = 2, m_F = 0)$  state, one finds for the first-order quadrupole shift

$$h \cdot \Delta\nu_Q^{(1)} = \langle \gamma J F m | H_Q | \gamma J F m \rangle = A \Theta(D_{3/2}) g(\alpha, \beta), \quad (7.22)$$

$$g(\alpha, \beta) = 3 \cos^2 \beta - 1 - \epsilon \sin^2 \beta \cos 2\alpha, \quad (7.23)$$

where  $\Theta(D_{3/2})$  is the quadrupole moment of the  ${}^2D_{3/2}$  state, and  $\alpha, \beta$  are the first two of the Euler angles that relate the principal axis frame to the laboratory frame where the  $z$ -axis is parallel to the magnetic field. The electric field gradient at the position of the ion is the sum of the field gradients generated by the trap and the electric stray field. Since Eq. (7.19) is linear in  $\nabla \mathbf{E}^{(2)}$ , the contributions of the trap and stray field gradients can be analyzed separately.

For the trap potential the deviation from cylindrical symmetry is negligible as the radial secular frequencies  $\omega_x$  and  $\omega_y$  are degenerate to within 1% for the traps used in the experiments (see Sec. 3.1). The trap potential in its principal axis frame is therefore in good approximation given by

$$\Phi_{trap} = (A_{DC} + A_{AC} \cos \Omega t) (x'^2 + y'^2 - 2z'^2), \quad (7.24)$$

where  $A_{DC} = U_{DC}/(\kappa r_0^2)$  and  $A_{AC} = U_{AC}/(\kappa r_0^2)$ . The contribution of  $A_{AC}$  to the quadrupole shift averages to zero to first order, but could lead to a considerable contribution via the second-order quadrupole shift as has been pointed out in [67]. For the case  $\epsilon = 0$ , the second-order shift of the  ${}^2D_{3/2}(F = 2, m_F)$  state is according to Eq. (B.14):

$$\begin{aligned} h \cdot \Delta\nu_Q^{(2)} &= \sum_{n \neq m} \frac{|\langle \gamma J F n | H_Q | \gamma J F m \rangle|^2}{E_m - E_n} \\ &= \frac{A^2 \Theta^2(D_{3/2})}{3 \Delta E_z} m (f_1(\beta)(8m^2 - 23) + f_2(\beta)(-2m^2 + 11)), \end{aligned} \quad (7.25)$$

$$f_1(\beta) = \frac{3}{2} \sin^2 \beta \cos^2 \beta, \quad (7.26)$$

$$f_2(\beta) = \frac{3}{8} \sin^4 \beta, \quad (7.27)$$

where  $\Delta E_Z$  is the Zeeman energy difference between adjacent  $m_F$  sublevels. The second-order shift is proportional to  $m$  and therefore exactly zero for the clock transition. Thus, the trapping field only causes a quadrupole shift of the clock transition if  $A_{DC} \neq 0$ .

The strength and symmetry of the electric stray field gradient is usually unknown, and the stray field gradient is not compensated. The main reason for this is that there is no easy way to measure the electric field gradient at the position of the ion aside from measuring the corresponding quadrupole shift itself for different directions of the magnetic field. In contrast to the electric stray field, its gradient does not lead to a shift in the position of the ion, so that the methods developed for the detection and compensation of the electric stray field yield no information about the field gradient. The presence of the stray field gradient however modifies the secular frequencies and an estimate of its strength can therefore be made from measurements of the secular frequencies for different



trap voltages, as will be discussed in Sec. 7.4.2. Even if one would know the field gradient precisely, it would normally be inconvenient to compensate it. In general five extra compensation electrodes would be required and one would have to iterate the compensation procedure for the stray field gradient with the one for the stray field. A compensation would be easier for a so-called endcap trap [142] that has no ring electrode. In this case, a stray field gradient due to patch charges on the trap electrodes will to a good approximation be oriented along the trap axis and therefore can be compensated by a change of the dc trap voltage  $U_{DC}$  [43]. The voltage would in this case be adjusted such, that the ratio of the radial and axial secular frequencies matches the theoretical value calculated from Eq. (3.7).

There also exist methods that can reduce the quadrupole shift without measuring or compensating the stray field gradient. These methods will be discussed in Sec. 7.4.3.

### 7.4.1 Measurement of the Quadrupole Moment of the $^2D_{3/2}$ State

In order to quantitatively investigate the quadrupole shift and evaluate its contribution to the systematic uncertainty of the frequency standard, it is necessary to know the quadrupole moment of the  $^2D_{3/2}$  state, which describes the coupling between the atomic state and the external electric field gradient. Once the quadrupole moment is known, one can use Eq. (7.22) to investigate the influence of the electric stray field gradient by measuring the quadrupole shift for different orientations of the magnetic field.

The quadrupole moment is experimentally determined by applying a voltage  $U_{DC}$  to the ring electrode of one trap and by measuring the resulting frequency shift relative to the second trap, which is kept at  $U_{DC} = 0$ . If  $A_{DC}$  is much larger than the strength of the electric stray field gradient, one can replace  $A$  by  $A_{DC}$  in Eq. (7.22) and set  $g(\alpha, \beta) = 3 \cos^2 \beta - 1 \equiv g(\beta)$ . If also the angle  $\beta$  between the magnetic field and the trap axis is known, the quadrupole moment  $\Theta(D_{3/2})$  can be calculated from the observed frequency shift using Eq. (7.22). In order to achieve a low measurement uncertainty it is advantageous to do the measurement at angles  $\beta = \{0, \pi\}$  or  $\beta = \pi/2$  where  $g(\beta)$  has an extremum and the measurement is therefore least sensitive to the uncertainty of  $\beta$ . Because  $\beta = \pi/2$  for any magnetic field vector in the plane perpendicular to the trap axis, while the conditions  $\beta = \{0, \pi\}$  can be realized only with a two-dimensional control of the magnetic field orientation, it is convenient to work at  $\beta = \pi/2$ . Experimentally, the magnetic field orientation is adjusted such that the absolute value of the frequency difference between the two traps  $|\Delta f|$  is maximized to within the statistical uncertainty in the vicinity of  $\beta = \pi/2$  as is shown in Fig. 7.2. For  $\beta = \pi/2$  one has  $g(\beta) = -1$ , so that according to Eq. (7.22) the quadrupole shift

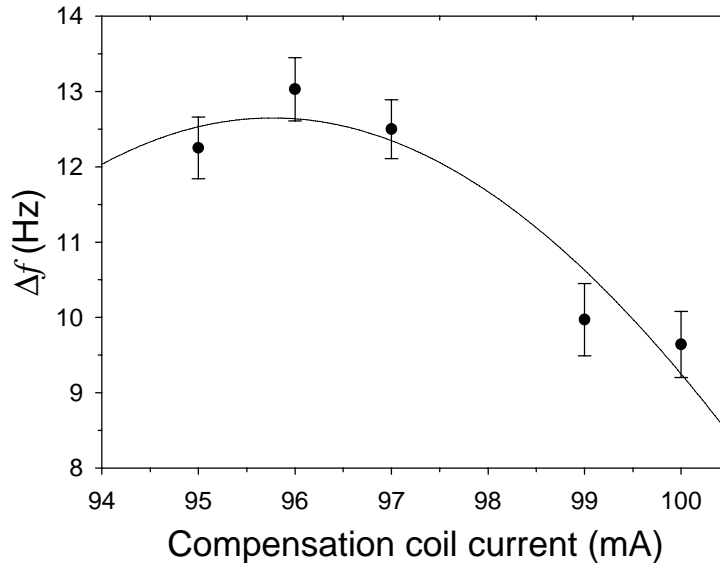


Figure 7.2: Quadrupole shift as a function of the orientation of the magnetic field. The orientation of the magnetic field was varied by changing the current in one of the coils used for the compensation of the ambient magnetic field. The data points include corrections for the quadratic Zeeman shift. The solid line is a sinusoidal fit to the data, the maximum corresponds to  $\beta = \pi/2$ .

is a linear function of the applied electric field gradient  $A_{DC}$  with a slope equal to  $-\Theta(D_{3/2})/h$ . From the slope of the linear regression to the experimental data shown in Fig. 7.3, one finds for the quadrupole moment:

$$\Theta(D_{3/2}) = 9.32(48) \cdot 10^{-40} \text{ Cm}^2 = 2.08(11)ea_0^2$$

where  $a_0$  is the Bohr radius. The given uncertainty consists of the statistical uncertainty of the measurement, a 3% uncertainty of the applied field gradient, and a  $5^\circ$  uncertainty in the adjustment of the angle  $\beta$ . The uncertainty of  $\beta$  leads to an asymmetry in the uncertainty of  $g(\beta)$  which was accounted for by applying a correction to  $g(\beta)$ , leading to  $g(\beta) = -0.983(0.017)$ . The experimental value given above is in good agreement with the result  $9.13 \cdot 10^{-40} \text{ Cm}^2$  of a multi-configuration Dirac-Hartree-Fock (MCDHF) calculation done by W. Itano [64]. With the experimental value for the quadrupole moment one can now determine the angle  $\beta$  (up to the ambiguities caused by the  $\cos^2 \beta$  dependence) between the magnetic field and the trap axis for arbitrary orientations of the magnetic field with high precision from the observed quadrupole shift. This method has been used to determine the relevant angle for the measurements of the scalar and tensor polarizabilities in Sec. 7.3.

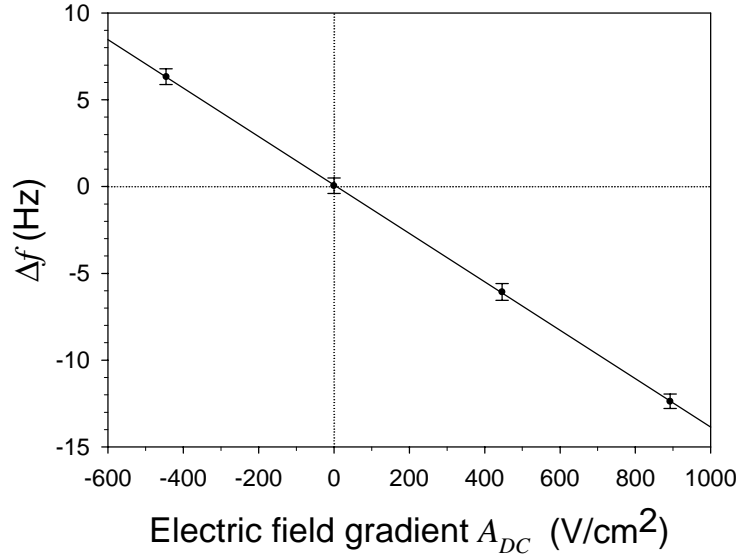


Figure 7.3: Measurement of the quadrupole shift as a function of the applied field gradient for  $\beta = \pi/2$ . The data points include corrections for the quadratic Zeeman shift. The solid line is the result of a linear regression to the data. The quadrupole moment  $\Theta(D_{3/2})$  is proportional to the slope of the linear regression.

### 7.4.2 Estimate for the Gradient of the Electric Stray Field

For a calculation of the contribution of the quadrupole shift to the systematic uncertainty of the  $^{171}\text{Yb}^+$  single-ion optical frequency standard, not only the quadrupole moment but also the gradient of the electric stray field has to be known. The total field gradient at the position of the ion is the sum of the trap field gradient and the stray field gradient. In its principal axis frame it is given by Eq. (7.20) and the corresponding quadrupole potential can be written as in Eq. (7.21). From the equation of motion Eq. (3.2) for the ion in the potential it can be seen that the presence of a static stray field gradient will change the  $a$ -parameters defined in Eq. (3.3) and therefore the secular frequencies. However, the secular frequencies in the absence of the stray field gradient are normally not known, because the asymmetry parameter  $\epsilon$  contains contributions from the imperfect shapes of the trap electrodes as well as from the stray field gradient and the two contributions can not easily be separated. An upper limit for the stray field gradient can be derived under the assumption that the electric stray field gradient is small compared to the amplitude of the ac field gradient of the trap potential. This is equivalent to the requirement that the frequency splitting of the radial frequencies  $\Delta\omega_r$  is small compared to the radial secular frequency defined as  $\omega_r = (\omega_x + \omega_y)/2$ . In this case the principal axis frame for the total electric field

gradient is given by the principal axis frame of the trap field gradient, and the influence of the stray field gradient can be described by modified  $a$ -parameters  $a'_i$ , defined as

$$a'_i \simeq \frac{8Q}{m\Omega^2\kappa r_0^2}(\gamma_i U_{DC} + \gamma'_i U_S), \quad \gamma'_x + \gamma'_y + \gamma'_z = 0, \quad (7.28)$$

where  $U_S/(\kappa r_0^2) \equiv A_S$  is the magnitude of the stray field gradient that one wants to estimate and the  $\gamma'_i$  are defined analogous to the  $\gamma_i$  in Eq. (3.3) with  $\epsilon \mapsto \epsilon'$ . Inserting the  $a'_i$  into Eq. (3.7) for the secular frequencies, the values of  $A_S$  and the  $\gamma'_i$  can be determined from the measured secular frequencies. This was done for several sets of secular frequencies measured for various trap parameters. As a result, it was found that  $A_S < 0.5 \text{ V/mm}^2$  and that the intrinsic asymmetry of the trap is  $\epsilon < 10^{-3}$ . Together with the experimental value for the quadrupole moment, this leads to an estimate for the systematic uncertainty of the frequency standard due to the quadrupole shift of  $\Delta\nu_Q \leq 1.4 \text{ Hz}$ . It is expected that part of the stray field gradient is due to the inhomogeneous electric field generated by the voltages applied for the compensation of micromotion to the ytterbium oven and electron source. Fig. 7.4 shows a measurement of the dependence of  $\Delta\omega_r$  and  $\omega_z/\omega_r$  on the voltages applied to the oven and the electron source. Extrapolating the quantities  $\Delta\omega_z/\omega_r$  and  $\Delta\omega_r$  to zero compensation voltage ( $U = 0$ ) and repeating the determination of the stray field gradient, one finds  $A_S \leq 1.0 \text{ V/mm}^2$ . This means, that the gradient produced by the compensation electrodes compensates part of the stray field gradient. Nevertheless it would be better to reduce the gradient produced by the compensation electrodes, because this field gradient will vary as the compensation voltages change over time. The contribution to the field gradient from the compensation electrodes could be significantly reduced by using pairs of plates as compensation electrodes, which would produce a more homogeneous electric field.

### 7.4.3 Methods for Reducing the Quadrupole Shift

Two methods have been proposed which in principle allow to eliminate the quadrupole shift without *a priori* knowledge of the electric field gradient. One method proposed by W. Itano [136] relies on the fact that  $g(\alpha, \beta)$  in Eq. (7.23) is a linear combination of spherical harmonics (see also Eq. (B.12)) and therefore the sum over  $g(\alpha, \beta)$  is equal to zero for any set of three mutually orthogonal directions of the magnetic field. This relation does not hold for the second-order quadrupole shift (Eq. (B.13)), which is a linear combination of the squared absolute values of spherical harmonics. For the case of the ytterbium clock transition, this is not a drawback since the second order quadrupole shift is equal to zero anyway. Comparing Eq. (7.23) with Eq. (7.13), one finds that the tensor part of the quadratic Stark shift is also proportional to a spherical harmonic

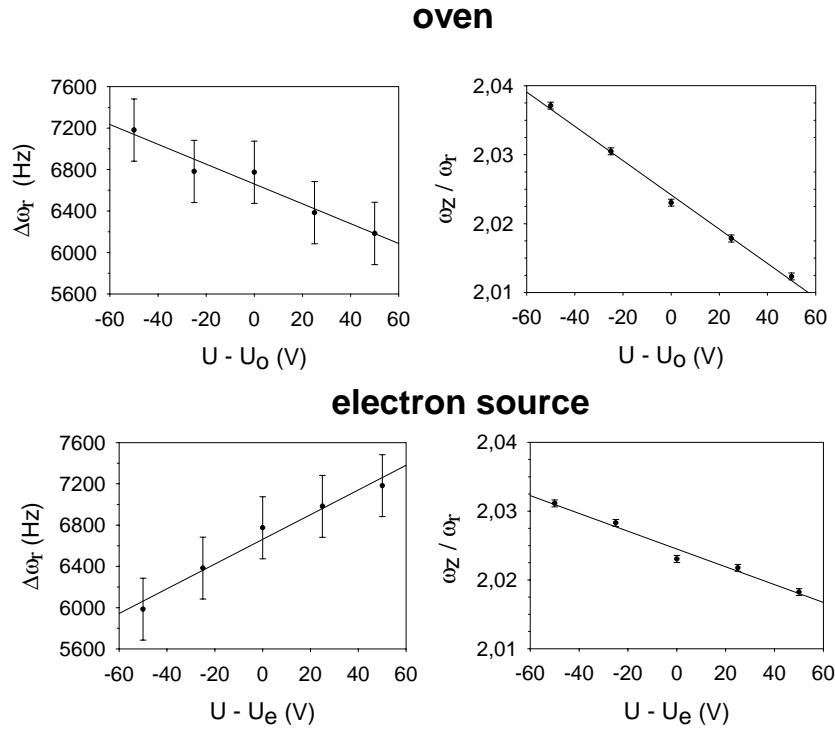


Figure 7.4: Dependence of the secular frequencies on the compensation voltages applied to the oven and the electron source. The applied voltages are given with respect to the voltages for optimum compensation of micromotion, which were  $U_o = 119.5$  V for the oven and  $U_e = 15.5$  V for the electron source, respectively. The solid lines are linear regressions to the data.

and thus will also average to zero for three mutually orthogonal magnetic fields. The suppression of the first-order quadrupole and tensor quadratic Stark shift that can be achieved depends on the precision to which the three magnetic field orientations are orthogonal. From numerical Monte Carlo simulations of the averaging process one finds that the uncertainty in the individual angles has to be about  $\pm 1^\circ$  to get a suppression of the orientation dependent shifts by a factor of 100. Such a precision usually requires the use of a magnetic shielding around the trap. Even then it will be a time-consuming effort to adjust the magnetic fields and prove that the necessary precision was achieved. One way to do this is to determine the individual orientations of the magnetic fields from series of Zeeman spectra for different polarizations of the clock laser as has been described in Sec. 5.3.2. Another way of checking the orthogonality of the three magnetic field orientations is to induce a large quadrupole shift and measure the suppression of the shift with sufficiently low statistical uncertainty. Since the degree of suppression also depends on the orientation of the electric field gradient relative to the

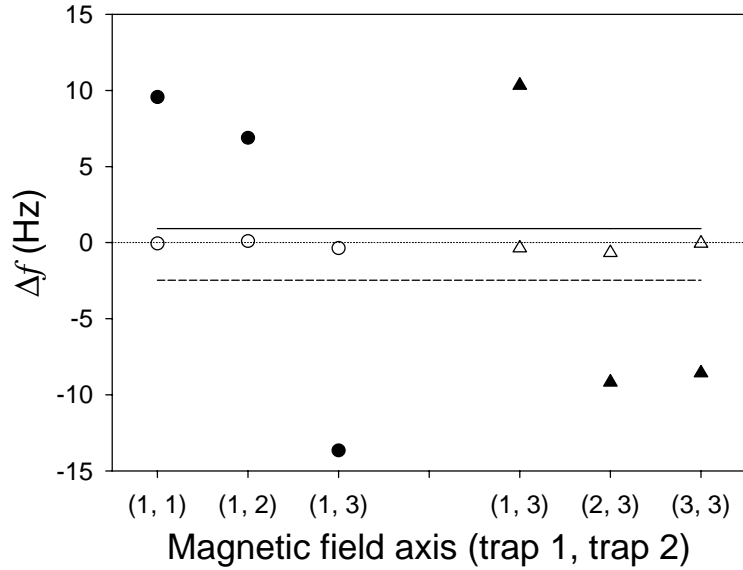


Figure 7.5: Averaging of the quadrupole shift induced by a voltage  $U_{DC} = +10$  V in trap 1 (solid triangles) and trap 2 (solid circles) over three approximately orthogonal magnetic field orientations. The lines mark the corresponding averages for trap 1 (dashed) and trap 2 (solid). The open symbols represent the frequency differences measured when both traps are at  $U_{DC} = 0$  V. The uncertainties of the individual data points are smaller than the size of their respective symbols.

three magnetic fields, the procedure should be repeated for at least one additional set of orthogonal magnetic fields to ensure, that the observed suppression is not accidental.

The experimentally realized sets of orthogonal magnetic field orientations so far are only approximately orthogonal with an estimated uncertainty of  $20^\circ$  for trap 1 and  $10^\circ$  for trap 2 derived from the analysis of series of Zeeman spectra. Fig. 7.5 shows a first experimental realization of the described averaging scheme. The frequency difference between the two trap systems was successively measured at  $U_{DC} = +10$  V for the three approximately orthogonal magnetic field orientations in each trap with respect to a fixed field orientation in the other trap which was kept at  $U_{DC} = 0$  V. The mean frequency differences obtained are  $-2.5$  Hz for trap 1 and  $0.9$  Hz for trap 2. The mean differences measured for the same combinations of magnetic field orientations, but with  $U_{DC} = 0$  in both traps were  $-0.4$  Hz for trap 1 and  $-0.1$  Hz for trap 2. For the data with an applied field gradient, the ratio of the averages to the respective measured maximum frequency differences can be taken as a measure for the suppression of the induced quadrupole shift. For trap 1 a suppression by about a factor 4 is found while for

trap 2 the corresponding factor is about 15. Due to the large uncertainties of the magnetic field orientations the suppression factors could vary widely if the orientation or symmetry of the electric field gradient would be changed. Thus the current implementation of the averaging scheme is not suited to reduce the contribution of the quadrupole shift to the systematic uncertainty of the frequency standard significantly. However, by installing magnetic shieldings around the traps it seems feasible to reduce the uncertainty in the magnetic field alignment to  $\sim 1^\circ$ , which would effectively reduce the quadrupole shift of the clock transition to about 10 mHz, corresponding to a fractional frequency uncertainty of  $1.5 \cdot 10^{-17}$ . In other ion trap experiments a significant suppression of the quadrupole and tensor Stark shift by averaging over three orthogonal magnetic field orientations has already been demonstrated for  $^{88}\text{Sr}^+$  [47] and  $^{199}\text{Hg}^+$  [64].

P. Dubé et al. proposed another method for eliminating the quadrupole shift that does not require precise control over the direction of the magnetic field [143]. This method uses the fact that the Hamiltonian for the quadrupole shift is traceless, which implies that the sum over the quadrupole shifts of all magnetic sublevels for a given transition is equal to zero up to any order of perturbation theory. Again, the same is true for the tensor part of the quadratic Stark shift, which can be seen for example by comparing Eq. (A.3) and Eq. (B.12) which both exhibit the same dependence on the magnetic quantum number  $m$ . The only requirement for this method to work is that the magnetic field is sufficiently stable during the measurement, so that all Zeeman components can be interrogated at the same magnetic field. As for the first method, this usually requires a magnetic shielding around the trap. The linear Zeeman shift also averages to zero, but not the quadratic Zeeman shift. Since the quadratic Zeeman shift can be calculated and corrected with low uncertainty, the contribution of the quadratic Zeeman shift to the total systematic uncertainty is not significantly increased by this method. In the operation of a frequency standard, one would alternately stabilize the probe laser to every  $m$  component of the transition. If the frequency fluctuations due to fluctuations of the magnetic field are small compared to the quantum projection noise, this procedure will not decrease the stability of the standard as long as the power of the probe laser and or its polarization are adjusted for maximum excitation probability every time the interrogation switches to another Zeeman component.

## 7.5 Gravitational Time Dilation

In Sec. 7.1 it was mentioned that the second-order Doppler effect is a manifestation of special relativistic time dilation. In the context of general relativity, the metric which defines how time and length intervals measured by two distant observers are related to each other contains also the action of the gravitational field. Time dilation effects can therefore appear even when the two observers are at rest with respect to each other. On earth, this gravitational time dilation leads to a relative shift of the frequency  $\nu$  observed in a reference frame at gravitational potential  $\phi$  with respect to the frequency  $\nu_0$  measured in the reference frame of the source at potential  $\phi_0$  of

$$\frac{\Delta\nu_G}{\nu_0} = \frac{\nu - \nu_0}{\nu_0} = -\frac{\phi - \phi_0}{c^2} \simeq -\frac{g\Delta r}{c^2} + O(\Delta r^2) \simeq -1 \cdot 10^{-16} \text{ m}^{-1}, \quad (7.29)$$

where  $g$  is the local acceleration of gravity at some reference potential surface and  $\Delta r = r - r_0$  is the difference of the heights of the two observers above the reference surface. If  $r > r_0$ , the frequency  $\nu$  is shifted to the red compared to  $\nu_0$ , while a clock located at  $r$  runs faster than its counterpart at  $r_0$ .

The local acceleration  $g$  can be measured using commercial equipment with a relative uncertainty of a few parts in  $10^9$  [144], which is negligible. For local frequency comparisons like the ones between the two ion traps it is sufficient to determine  $\Delta r$  with centimeter precision to reduce the relative uncertainty of  $\Delta\nu_G$  to  $1 \cdot 10^{-18}$ , but for long distance comparisons the accurate determination of  $\Delta r$  might pose a problem. In this case also higher-order terms in the expansion of the gravitational potential should be taken into account [10].

## 7.6 Collision Effects

Collisions with the background gas can lead to a frequency shift of the clock transition. No rigorous calculation of this effect was performed, but an estimate of the magnitude of the collisional shift was done on the basis of tabulated collisional shifts for a variety of neutral atoms and some light ions given in [145]. The typical frequency shifts are less than  $3 \cdot 10^{-12} \text{ Hz cm}^{-3}$ . The largest partial pressure of a background gas component in the experiment is estimated to be  $\leq 10^{-6} \text{ Pa}$  for molecular hydrogen. The corresponding density at room temperature is about  $2.4 \cdot 10^8 \text{ cm}^{-3}$ , leading to a frequency shift of  $7.2 \cdot 10^{-4} \text{ Hz}$ . The relative frequency shift is about  $1.1 \cdot 10^{-18}$ . Even though this estimate may not be very accurate, one can be confident that collision effects play at present no important role for the systematic uncertainty of the  $^{171}\text{Yb}^+$  single-ion optical frequency standard.



## 7.7 Cavity QED Effects

From cavity quantum electrodynamics (CQED) it is known that the presence of boundary conditions for electromagnetic fields in the vicinity of an atom can lead to shifts of its energy levels. According to [146] these level shifts can be divided into groups: Shifts caused by the modification of the vacuum fluctuations close to the surface imposing the boundary conditions and shifts arising from the interaction of the atom with the part of its own radiation that is reflected from the surface. The size and relative contribution of the individual shift mechanisms to the energy shift of a given atomic state depends on the geometry and the electrical properties of the boundary, the atomic state, and the typical distance of the atom from the boundary. For the simple case of an atom located between two parallel perfectly conducting plates, it was found that if the distance  $r_0$  of the atom to one of the plates is large compared to the transition wavelengths between the atomic states, the energy shift of the state  $|a\rangle$  is approximately given by [146, 147]

$$\Delta\nu_a \sim -\frac{c}{16\pi^3\epsilon_0} \left( \frac{\alpha}{r_0^4} + \frac{4}{r_0} \sum_{b < a} |\langle a|\mu|b\rangle|^2 \ln |\sin \omega_{ab}r_0| \right). \quad (7.30)$$

Here  $\alpha$  is the static polarizability of the state  $|a\rangle$ , and the sum is over all states  $|b\rangle$  with energies below the energy of the state  $|a\rangle$ . The first term is the Casimir interaction, while the second term appears only for excited states of the atom and describes the self-interaction of the excited state with its own radiation and the resonantly enhanced vacuum fluctuations. For the experimental setup described in Chapter 4 the relevant boundary conditions are imposed by the trap electrodes, which are at a distance  $r_0 \sim 1$  mm from the ion that is large compared to the wavelength of the clock transition. Neither the ring electrode nor the two endcap electrodes form a good resonator, because of their conical form and relatively low reflectivity. Moreover, for the  ${}^2D_{3/2}$  state there exist no electric dipole allowed transitions to lower energy states. It seems therefore reasonable to ignore the second term in Eq. (7.30) and estimate the influence of CQED effects on the clock transition from the Casimir term. For the clock transition one has then

$$\Delta\nu_C \sim \frac{c}{8\pi^3\epsilon_0} \frac{\Delta\alpha_S + \alpha_T}{r_0^4} \simeq 7 \cdot 10^{-11} \text{ Hz}, \quad (7.31)$$

where the static polarizabilities  $\Delta\alpha_S$  and  $\alpha_T$  from Sec. 7.3 where used. Even though the above estimate represents no rigorous treatment of the experimental situation, it gives confidence that cavity QED effects play no important role for the systematic uncertainty of the frequency standard.

## 7.8 Line Profile Asymmetry

An asymmetry in the line profile of the probe laser would lead to an asymmetric lineprofile of the atomic resonance observed in the experiment. Because the two trap systems share the same probe laser, such an asymmetry would not lead to an observable frequency difference in a trap comparison experiment if both systems are operated under identical conditions. For different values of the frequency modulation  $\delta$  (see Sec. 5.4) for the two servo systems an asymmetry of the line profile should lead to a frequency difference between the two servos. Tests were performed for frequency resolutions of 30 Hz, and 10 Hz. The frequency modulation was varied by 50% of its nominal value for one of the servos, and no significant frequency differences were observed for averaging times of a few hundred seconds. An upper limit for the contribution of a probe laser induced line profile asymmetry is thus given by the statistical uncertainty of the measurements with different frequency modulations in the two servos, which was approximately 0.5 Hz. This corresponds to a relative uncertainty of  $7 \cdot 10^{-16}$ .

The effect of a possible line profile asymmetry of the probe laser on the excitation spectrum is small, if the intrinsic laser linewidth is small compared to the width of the excitation spectrum. Effects of laser line asymmetries are therefore expected to be important mainly close to the resolution limit. The most likely source of an asymmetric probe laserline is the electronics involved in the frequency stabilization of the probe laser to the reference cavity. It is expected that any possible asymmetry caused by the electronics can be controlled, so that it does not limit the uncertainty of the frequency standard.

Another mechanism that could lead to a systematic frequency shift is an asymmetry in the servo system used to stabilize the probe laser frequency to the atomic transition. The frequency error due to an asymmetry of the servo system would likely be proportional to the linewidth  $\Delta\omega$  of the resonance. An asymmetry should therefore become observable in frequency comparisons with different durations of the probe pulses in the two systems. From Eq. (6.1) one finds that without dead times and for a Fourier limited excitation of the clock transition, the instability of the frequency standard is proportional to  $\sqrt{\Delta\omega}$ . This means that if the linewidth of the resonance for one trap system is increased with respect to the other trap system by a factor of  $N$ , the sensitivity to servo asymmetries increases as  $\sqrt{N}$  for a given averaging time. In the experiment this was done comparing first the center frequencies of 10 Hz resonances in both traps. The relative statistical uncertainty was in this case about  $\sigma_y(500s) = 7 \cdot 10^{-16}$  and no significant frequency difference between the trap systems was observed. Then the resolution in one trap was changed to 1 kHz. For the same averaging time of about 500 seconds, also no significant frequency difference between the two traps was observed after the change in resolution. This leads to an upper limit for the relative frequency error due to a servo asymmetry of  $1 \cdot 10^{-16}$  for the operation at

10 Hz resolution. As in the case of a probe laser asymmetry, it is expected that a possible servo asymmetry can be controlled sufficiently well, so that it will not limit the uncertainty of the frequency standard.

## 7.9 Uncertainty Budget

Table 7.1 summarizes the contributions to the systematic uncertainty of the  $^{171}\text{Yb}^+$  single-ion optical frequency standard that were discussed throughout the Chapter.

The largest contribution comes from the quadrupole shift, which dominates the total relative systematic uncertainty of  $1.0 \cdot 10^{-15}$ . Up to now, no strict limit for the magnitude of the quadrupole shift could be derived. The shift calculated from the estimate for the field gradient (Sec. 7.4.2) gives an upper bound for the quadrupole shift for the present state of the experiment, but the stray field gradients might change considerably over time. The trap comparison measurements described in Chapter 8 suggest that the stray field gradient may be weaker than expected from the measurements of the secular frequencies. A direct measurement of the quadrupole shift requires a good control over the direction of the magnetic field, as do the two methods discussed in Sec. 7.4.3 which allow to correct for the quadrupole shift. One of the methods was already implemented in the experiment, but due to the lack of magnetic shielding a suppression of the quadrupole shift by only a factor 4 to 15 was achieved so far. However, for the future suppression factors of more than 100 can be expected [64], reducing the contribution of the quadrupole shift to the relative systematic uncertainty to about  $1 \cdot 10^{-17}$ . As a side effect, the magnetic shielding will also allow the use of lower static magnetic fields which will reduce the quadratic Zeeman shift and will also reduce time-dependent magnetic stray fields to a negligible level.

The next limit for the uncertainty will then arise from the uncertainty in the determination of the blackbody AC Stark shift, which is at the moment in the range of  $1 \cdot 10^{-16}$ . While this systematic will pose no problem for the comparisons between two ytterbium standards that are operated at the same temperature, it will limit the uncertainty for comparisons with other atomic frequency standards. More precise measurements of the static polarizabilities and a better understanding of the slight discrepancy between theory and experiment for the static polarizabilities found in Sec. 7.3.1 will probably help to improve the precision of the calculations. It is expected that the blackbody AC Stark shift can be determined and corrected with an uncertainty of about one percent, leading to a relative uncertainty of about  $5 \cdot 10^{-18}$ . For the case that such a precision can not be achieved in the calculations, there is also the option to cool the trap apparatus to lower temperatures as for example in the case of the  $^{199}\text{Hg}^+$  single-ion frequency

standard, which is operated at the temperature of liquid helium [65]. Already at the temperature of liquid nitrogen, the blackbody AC Stark shift would become negligible.

Table 7.2 lists the projected systematic uncertainties of the  $^{171}\text{Yb}^+$  single-ion optical frequency standard accounting for the expected experimental improvements.

With the experimental improvements discussed above, it is expected that a  $^{171}\text{Yb}^+$  single-ion optical frequency standard can achieve a relative uncertainty of about  $1.0 \cdot 10^{-17}$  over the next years. A limiting factor for further improvement might be the instability of the standard. With the present instability of  $\sigma_y(t) \simeq 7.8 \cdot 10^{-15} t^{-\frac{1}{2}}$ , it would take about one week of continuous averaging to reach the  $10^{-17}$  level of statistical uncertainty and even at the minimal instability for the ytterbium standard estimated as  $\sigma_y(t) \simeq 2.7 \cdot 10^{-15} t^{-\frac{1}{2}}$  the time required would still be about two and a half days. Under such circumstances, systematic parameter studies will be time consuming and demand a high long-term reliability of especially all the lasers involved in the experiment. Also issues like long-term drifts of compensation voltages will become more important.

Table 7.1: Systematic frequency shifts of the clock transition and their contribution to the systematic uncertainty of the  $^{171}\text{Yb}^+$  single-ion optical frequency standard for the present state of the experiment.

Source of the systematic frequency shift	Absolute shift [Hz]	Relative shift	Correction	Relative uncertainty
<b>Second-order Doppler shift</b>				
Secular motion	$-2.1 \cdot 10^{-4}$	$-3.0 \cdot 10^{-19}$	-	$3.0 \cdot 10^{-19}$
Micromotion	$-2.6 \cdot 10^{-3}$	$-3.8 \cdot 10^{-18}$	-	$3.8 \cdot 10^{-18}$
<b>Second-order Zeeman shift</b>				
Static field $ \mathbf{B}  = 1 \mu\text{T}$	$+5.2 \cdot 10^{-2}$	$+7.6 \cdot 10^{-17}$	✓	$7.6 \cdot 10^{-19}$
50 Hz stray field	$+5.0 \cdot 10^{-3}$	$+7.3 \cdot 10^{-18}$	-	$7.3 \cdot 10^{-18}$
Blackbody field at $T = 297 \text{ K}$	$+1.0 \cdot 10^{-3}$	$+1.5 \cdot 10^{-18}$	-	$1.5 \cdot 10^{-18}$
<b>Second-order Stark shift</b>				
Secular motion	$-1.4 \cdot 10^{-4}$	$-2.0 \cdot 10^{-19}$	-	$2.0 \cdot 10^{-19}$
Micromotion	$-6.1 \cdot 10^{-3}$	$-1.0 \cdot 10^{-17}$	-	$1.0 \cdot 10^{-17}$
Blackbody field at $T = 297 \text{ K}$	-0.35	$-5.1 \cdot 10^{-16}$	✓	$1.0 \cdot 10^{-16}$
Probe laser light shift	$-2.5 \cdot 10^{-4}$	$-3.6 \cdot 10^{-19}$	-	$3.6 \cdot 10^{-19}$
<b>Quadrupole shift</b>				
Estimate from secular frequencies	$<1.4$	$+2.0 \cdot 10^{-15}$	-	$2.0 \cdot 10^{-15}$
Data scatter in trap comparison	$<0.7$	$+1.0 \cdot 10^{-15}$	-	$1.0 \cdot 10^{-15}$
<b>Cavity QED effects</b>				
	$7 \cdot 10^{-11}$	$1.0 \cdot 10^{-25}$	-	$1.0 \cdot 10^{-25}$
<b>Collisional shift</b>				
	$7.2 \cdot 10^{-4}$	$1.1 \cdot 10^{-18}$	-	$1.1 \cdot 10^{-18}$
<b>Laser frequency lock</b>				
	$<1 \cdot 10^{-2}$	$1.5 \cdot 10^{-17}$	-	$1.5 \cdot 10^{-17}$

Table 7.2: Projected systematic uncertainties of the  $^{171}\text{Yb}^+$  single-ion optical frequency standard.

Source of the systematic frequency shift	Absolute shift [Hz]	Relative shift	Correction	Relative uncertainty
<b>Second-order Doppler shift</b>				
Secular motion	$-2.1 \cdot 10^{-4}$	$-3.0 \cdot 10^{-19}$	-	$3.0 \cdot 10^{-19}$
Micromotion <sup>a</sup>	$-5 \cdot 10^{-4}$	$-7.6 \cdot 10^{-19}$	-	$7.6 \cdot 10^{-19}$
<b>Second-order Zeeman shift</b>				
Static field $ \mathbf{B}  = 0.1 \mu\text{T}$ <sup>b</sup>	$+5.2 \cdot 10^{-4}$	$+7.6 \cdot 10^{-19}$	✓	$7.6 \cdot 10^{-21}$
50 Hz stray field <sup>b</sup>	$+5.0 \cdot 10^{-4}$	$+7.3 \cdot 10^{-19}$	-	$7.3 \cdot 10^{-19}$
Blackbody field at $T = 297$ K	$+1.0 \cdot 10^{-3}$	$+1.5 \cdot 10^{-18}$	✓	$1.5 \cdot 10^{-19}$
Blackbody field at $T = 70$ K	$+3.1 \cdot 10^{-6}$	$+4.5 \cdot 10^{-21}$	-	$4.5 \cdot 10^{-21}$
<b>Second-order Stark shift</b>				
Secular motion	$-1.4 \cdot 10^{-4}$	$-2.0 \cdot 10^{-19}$	-	$2.0 \cdot 10^{-19}$
Micromotion <sup>a</sup>	$-2.4 \cdot 10^{-4}$	$-4.0 \cdot 10^{-19}$	-	$4.0 \cdot 10^{-19}$
Blackbody field at $T = 297$ K <sup>c</sup>	-0.35	$-5.1 \cdot 10^{-16}$	✓	$5.0 \cdot 10^{-18}$
Blackbody field at $T = 70$ K	$-2 \cdot 10^{-3}$	$-3 \cdot 10^{-18}$	✓	$3.0 \cdot 10^{-19}$
Probe laser light shift	$-2.5 \cdot 10^{-4}$	$-3.6 \cdot 10^{-19}$	-	$3.6 \cdot 10^{-19}$
<b>Quadrupole shift</b> <sup>b,d</sup>				
Estimate from secular frequencies	$< 1.4 \cdot 10^{-2}$	$+2.0 \cdot 10^{-17}$	-	$2.0 \cdot 10^{-17}$
Data scatter in trap comparison	$< 7.0 \cdot 10^{-3}$	$+1.0 \cdot 10^{-17}$	-	$1.0 \cdot 10^{-17}$
<b>Cavity QED effects</b>				
	$7 \cdot 10^{-11}$	$1.0 \cdot 10^{-25}$	-	$1.0 \cdot 10^{-25}$
<b>Collisional shift</b>				
	$7.2 \cdot 10^{-4}$	$1.1 \cdot 10^{-18}$	-	$1.1 \cdot 10^{-18}$
<b>Laser frequency lock</b> <sup>e</sup>				
	$< 1 \cdot 10^{-3}$	$1.5 \cdot 10^{-18}$	-	$1.5 \cdot 10^{-18}$

<sup>a</sup>Resolution of the imaging system increased by a factor 5.<sup>b</sup>with magnetic shielding<sup>c</sup>uncertainty of the polarizabilities  $\Delta\alpha_s, \alpha_T$  reduced to 1%<sup>d</sup>Implementation of orthogonal set of magnetic field axis with angle uncertainty  $1^\circ$ <sup>e</sup>improved lock algorithm and reduced laser frequency drift

# Chapter 8

## Agreement Between the Two Trap Systems

In the previous sections the systematic frequency shifts of the clock transition were investigated. From the uncertainty budget shown in Table 7.1 it can be expected that for a compensation of electric stray fields as described in Sec. 3.4 and without an applied static electric field gradient, the frequencies of the clock transitions realized by two ions stored in separate traps would agree on the hertz level or below. Fig. 8.1 shows the result of eight trap comparison measurements taken on two days separated by one week. Each data point represents the frequency difference  $\Delta f$  averaged over 500-700 s. In order to be sensitive to systematic effects that depend on the orientation of the magnetic field, measurements were done for the two sets of approximately orthogonal magnetic field orientations from Fig. 7.5 and for the orientation used in the measurement of the quadrupole moment of the  $^2D_{3/2}$  state in Sec. 7.4.1. The measurements 1 – 5 correspond to the data points shown as open symbols in Fig. 7.5. The weighted mean frequency difference of all eight measurements is 0.26 Hz and the mean statistical uncertainty of the individual measurements is 0.42 Hz. All data points include a correction for the quadratic Zeeman shift. The remaining systematic uncertainty due to the quadratic Zeeman shift here is about 50 mHz, while the combined uncertainty contributions of the quadratic Stark and second-order Doppler effect is below 10 mHz. The blackbody AC Stark shift is about  $-0.35$  Hz at  $T = 297$  K and should be equal to within 20 mHz for both traps. The total systematic uncertainty of the measurements not including the uncertainty for the quadrupole shift is then about 55 mHz, which is small compared to the statistical uncertainties of the measurements. The estimate for the uncertainty contribution of the quadrupole shift  $\Delta\nu_Q \leq 1.4$  Hz derived in Sec. 7.4.2 is large compared to the statistical uncertainty, but also less strict than the estimates for other systematic uncertainties. The measurements shown in Fig. 8.1 thus can be interpreted as a measurement of the typical quadrupole shift under normal operating conditions

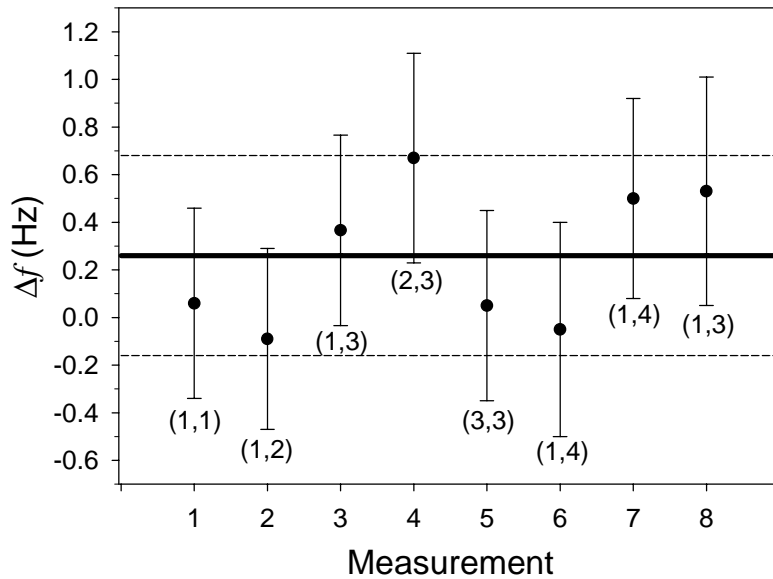


Figure 8.1: Frequency difference  $\Delta f$  in the absence of external perturbations. The magnetic field orientations are labeled as in Fig. 7.5 and (1,4) is the orientation used in the measurement of the quadrupole moment. The data were taken on two days and are displayed in temporal order. The solid line is the weighted average of the data, the dashed lines mark the average statistical uncertainty of the data points.

of the experiment. Assuming that the scatter of the data in Fig. 8.1 is only due to the orientation dependence of the quadrupole shift, one finds from the scatter of measurements 1–3 and 3–5 that the typical quadrupole shift under the above assumption is below 0.7 Hz. If it is further assumed that the magnetic field orientations 1, 2, 3 are exactly orthogonal for both traps, the frequency difference  $\Delta f_0$  between the traps in the absence of the quadrupole shift (and tensor quadratic Stark shift) is given by

$$\Delta f_0 = \frac{1}{3} (\Delta f_{11} + \Delta f_{12} - \Delta f_{13} + \Delta f_{23} + \Delta f_{33}), \quad (8.1)$$

where  $\Delta f_{ij}$  is the frequency difference measured for the combination of magnetic field orientations  $(i, j)$ . From the estimates of other systematic frequency shifts made above, one would expect  $\Delta f_0$  to be consistent with zero within the statistical uncertainty of the measurement. Using measurements 1–5 from Fig. 8.1 one finds  $\Delta f_0 = 0.1(6)$  Hz, which is consistent with the estimated systematic uncertainty. The uncertainty of  $\Delta f_0$  is dominated by the uncertainties in the mutual angles of the magnetic field orientations of  $20^\circ$  for trap 1 and  $10^\circ$  for trap 2 (see Sec. 5.3.2). The contribution of the angle uncertainties to the uncertainty of  $f_0$  was estimated



---

from numerical Monte Carlo simulations where the orientations of the magnetic fields were varied within the range of their uncertainties.

In order to analyze the data from Fig. 8.1 without any assumption on the origin of the scatter of the data, a  $\chi^2$ -test was performed for the hypothesis that the data sample represents one constant value equal to the mean of the data set. The result is  $\chi^2 = 3.4$ , which for seven degrees of freedom gives a probability of 84% that a random set of eight values with the same mean value and the same statistical uncertainty as the data would give the same or a higher  $\chi^2$ . Thus, within the statistical uncertainty of the measurements the data yield no evidence for frequency shifts of the clock transition that depend on the orientation of the magnetic field. For an uncertainty estimate on the observed mean frequency difference of 0.26 Hz, it therefore appears justified to regard the scatter of the data as random and the resulting statistical uncertainty of the mean would be  $0.42/\sqrt{8} = 0.15$  Hz. Nevertheless, as it is difficult to determine the contribution of the quadrupole shift to the scatter of the data and because the data sample is not sufficiently large to allow a significant statement on the distribution of the data points, the data is not assumed to represent one constant value. Instead, the data points are treated as measurements of eight independent and potentially different quantities. The uncertainty of the mean frequency difference can then be estimated as the mean statistical uncertainty of the individual measurements, which is 0.42 Hz. The relative frequency difference between the two trap systems is then  $3.8(6.1) \cdot 10^{-16}$ . This agreement is comparable to the best agreement found in a comparison of cesium fountain clocks [21], which are the most accurate clocks available at present.

# Chapter 9

## Outlook

In the experiments described in this work it could be demonstrated that in comparison to cesium fountain clocks a  $^{171}\text{Yb}^+$  single-ion optical frequency standard is competitive in its relative uncertainty and already superior in its relative instability.

The main experimental limit for the uncertainty is presently the insufficient control over the direction of the magnetic field as it is required for the control of the quadrupole shift. The implementation of a magnetic shielding will solve this problem and relative uncertainties in the range of  $10^{-17}$  will become achievable. In order to demonstrate such low uncertainties within reasonable measurement times, the instability of the standard has to be further improved. This can be done by reducing the dead time in the interrogation sequence and the number of invalid excitations, and by improving the quality of the excitation spectra at the resolution limit. Future frequency comparisons between the two trap systems with lower statistical uncertainty and better control over the magnetic field will also allow a direct quantitative measurement of the quadrupole shift due to the electric stray field gradient.

The development of more stable and accurate frequency standards is of great importance for physics. Not only are many precise tests of fundamental physics already directly or indirectly connected to frequency measurements, but an increased measurement precision also may open the way for experimental tests of new physics like theories of grand unification. The agreement between two frequency standards based on the same atomic transition in a single ion can be used as a precise test of the indistinguishability of two particles of the same kind, which is one of the fundamental assumptions of quantum mechanics. Since the relative uncertainties of the present free-space time and frequency transfer techniques are limited at about  $10^{-15}$ , the first applications of optical frequency standards will be in local laboratory measurements. However, especially single-ion standards offer also advantages for technical applications, because in contrast to cesium

standards their accuracy is (at least in the presence of gravity) not related to the size of the apparatus and thus in principle single-ion standards can be built very compact and transportable without losing their accuracy. In this respect the development of single-ion frequency standards will also profit from the experimental and technical progress of the many other kinds of ion trap experiments especially in the context of quantum computation [30–32, 118] and will vice versa itself continue to add to the progress of these experiments.

It is generally assumed that an unperturbed atomic transition frequency is itself an invariant quantity, because it is determined by fundamental constants. However, most theories attempting to unify the fundamental interactions allow or even imply variations of the coupling constants [13]. According to the inflationary model, dramatic changes of particle properties took place in the early evolution of the universe and it is conceivable that remnants of these changes are still observable today. If fundamental constants would vary, a fundamental assumption of metrology would turn out to be wrong. One of the most interesting applications of frequency standards is therefore in experiments that test the constancy of fundamental constants.

Variations of the constants have been searched for in various contexts [12, 14] and various predictions about the relative rate of change of different constants have been made [148–150]. One of the most important coupling constant in this context is the fine structure constant  $\alpha$  which, being a dimensionless quantity, can be determined without reference to a specific system of units. Together with the Rydberg constant, it determines the frequencies of optical atomic transitions. From astrophysical measurements of quasar absorption lines a relative change of the fine structure constant of  $\Delta\alpha/\alpha = (-0.54 \pm 0.12)$  was deduced over a time scale of about  $10^{10}$  years [151]. However, there is also another analysis of quasar absorption spectra where within a  $3\sigma$  uncertainty no change of  $\alpha$  was found [152], so the question if there is a significant experimental evidence for a cosmological variation of  $\alpha$  is still under debate. The most stringent limit on the present variation of the fine structure constant of  $\dot{\alpha}/\alpha = (-0.3 \pm 2) \cdot 10^{-15} \text{ yr}^{-1}$  was obtained by the comparison of optical transition frequencies in  $^{171}\text{Yb}^+$ ,  $^{199}\text{Hg}^+$  and hydrogen [54] and precise frequency comparisons have led also to constraints of other constants [41, 50, 53, 54], which demonstrates the potential of optical frequency standards not only for metrology but also for experiments in fundamental physics.

$^{171}\text{Yb}^+$  is probably one of the most interesting system to study the time variation of fundamental constants, because it offers three transitions suitable for the realization of a frequency standard. The  $^2S_{1/2}(F=0) \rightarrow ^2D_{3/2}(F=2)$  quadrupole transition investigated in this work and the  $^2S_{1/2}(F=0) \rightarrow ^2F_{7/2}(F=2)$  octupole transition currently investigated at NPL in the UK [44] have the largest known difference in sensitivity to a change of the fine structure constant

$\alpha$  [153, 154], thus allowing in principle the most sensitive test of a time variation of  $\alpha$ . This test could even be done within one ion, making the test less sensitive to systematic errors. Together with precise measurements of the ground state hyperfine splitting, which can be used as a microwave frequency standard as it was demonstrated at the CSIRO in Australia [106] and by comparisons with cesium clocks, also temporal variations of other constants like the Rydberg constant or the electron to proton mass ratio can be investigated with high precision.

The large selection of reference transitions combined with the long storage time achieved in radiofrequency traps, the simple cooling scheme and the possibility to generate all necessary optical wavelength from diode lasers, probably makes  $^{171}\text{Yb}^+$  presently the most versatile system for the realization of frequency standards of the highest precision.

# Appendix A

## Calculation of the Quadratic Stark Shift

The calculation of the quadratic Stark shift follows the calculations given in [136, 155]. In the following it is assumed that the quadratic Stark shift is small compared to the linear Zeeman shift of the investigated atomic transition. The quadratic Stark shift can then be determined from the matrix elements of  $H_S$  calculated in the same basis of states  $|\gamma J F m\rangle$  that diagonalizes the Zeeman Hamiltonian. The Stark Hamiltonian is

$$H_S = -\mathbf{d} \cdot \mathbf{E}, \quad (\text{A.1})$$

where  $\mathbf{d}$  is the electric dipole moment operator and  $\mathbf{E}$  is the electric field. Treating  $H_S$  by second-order perturbation theory in the  $(IJ)$  coupling approximation one finds that for an atom with nuclear spin  $I$  the quadratic Stark shift of the state  $|\gamma J F m\rangle$  is given by [136, 155]

$$\begin{aligned} h\Delta\nu_S(\gamma, J, F, m, \mathbf{E}) &= -(2\alpha_S(\gamma, J) + \alpha_T(\gamma, J, F) g(F, m, \beta)) \frac{|\mathbf{E}|^2}{4} \quad (\text{A.2}) \\ g(F, m, \beta) &= \frac{3m^2 - F(F+1)}{F(2F-1)} (3 \cos^2 \beta - 1), \end{aligned}$$

where  $\beta$  is the angle between the electric field vector and the orientation of the static magnetic field defining the quantization axis in the laboratory frame. The tensor electric polarizability  $\alpha_T(\gamma, J, F)$  can be written as

$$\alpha_T(\gamma, J, F) = (-1)^{I+J+F} K(J, F) \left\{ \begin{matrix} F & J & I \\ J & F & 2 \end{matrix} \right\} \alpha_T(\gamma, J), \quad (\text{A.3})$$

$$K(J, F) = \sqrt{\frac{F(2F-1)(2F+1)(2J+3)(2J+1)(J+1)}{(2F+3)(2F+1)J(2J-1)}}. \quad (\text{A.4})$$

Table A.1: Static polarizabilities of the  ${}^2S_{1/2}$  and  ${}^2D_{3/2}$  states of  ${}^{171}\text{Yb}^+$  for different sets of oscillator strength data

State	$\alpha_S [10^{-40} \text{ Jm}^2/\text{V}^2]$	$\alpha_T [10^{-40} \text{ Jm}^2/\text{V}^2]$	Atomic data reference
${}^2S_{1/2}$	10.1	-	[134]
	8.9	-	[137]
	9.8	-	[137, 156]
${}^2D_{3/2}$	18.0	-14.5	[134]
	14.1	-11.5	[137]

In the case of the  ${}^2D_{3/2}(F = 2, m = 0)$  state in  ${}^{171}\text{Yb}^+$ ,  $g(2, 0, \beta) = -(3 \cos^2 \beta - 1)$  and  $\alpha_T(D, 3/2, 2) = \alpha_T(D, 3/2)$ . For the interaction with a static electric field  $\alpha_S(\gamma, J)$  and  $\alpha_T(\gamma, J)$  can be written in terms of the oscillator strengths  $f_{\gamma J \gamma' J'}$ :

$$\alpha_S(\gamma, J) = \frac{4\pi\epsilon_0 e^2}{m_e} \sum_{\gamma' J' \neq \gamma J} \frac{f_{\gamma J \gamma' J'}}{\omega_{\gamma' J' \gamma J}^2}, \quad (\text{A.5})$$

$$\alpha_T(\gamma, J) = \frac{4\pi\epsilon_0 e^2}{m_e} K_2(J) \sum_{\gamma' J' \neq \gamma J} (-1)^{J-J'} \left\{ \begin{matrix} 1 & 1 & 2 \\ J & J & J' \end{matrix} \right\} \frac{f_{\gamma J \gamma' J'}}{\omega_{\gamma' J' \gamma J}^2}, \quad (\text{A.6})$$

$$K_2(J) = \sqrt{\frac{30J(2J-1)(2J+1)}{(2J+3)(J+1)}}.$$

Here  $m_e$  is the electron mass, and  $\omega_{\gamma' J' \gamma J} = \omega_{\gamma' J'} - \omega_{\gamma J}$  is the angular frequency of the transition from the state  $|\gamma J\rangle$  to the state  $|\gamma' J'\rangle$ . Table A.1 gives values for the static polarizabilities calculated in [138] and in this work for different sets of available oscillator strength data. The most reliable values are probably obtained from the data set in [137], which is the largest one available at present.

For an estimate of the light shift in Sec. 7.3.3 one needs to calculate the electric polarizabilities for the case that the electric field  $\mathbf{E}$  is not static but oscillates at the laser frequency  $\omega_L$ . This can be done by replacing

$$\omega_{\gamma' J' \gamma J}^2 \mapsto \omega_{\gamma' J' \gamma J}^2 - \omega_L^2 \quad (\text{A.7})$$

in the equations for  $\alpha_S(\gamma, J)$  and  $\alpha_T(\gamma, J)$ . For the clock transition one finds for  $\omega_L/2\pi \simeq 688$  THz using the oscillator strength data from [137]

$$\alpha_S^{AC}(S, 1/2) \simeq 22.2 \cdot 10^{-40} \frac{\text{Jm}^2}{\text{V}^2}, \quad (\text{A.8})$$

$$\alpha_S^{AC}(D, 3/2) \simeq 0.8 \cdot 10^{-40} \frac{\text{Jm}^2}{\text{V}^2}, \quad (\text{A.9})$$

$$\alpha_T^{AC}(D, 3/2) \simeq -4.1 \cdot 10^{-40} \frac{\text{Jm}^2}{\text{V}^2}. \quad (\text{A.10})$$

---

In order to calculate the polarizabilities for the case of the blackbody AC Stark shift taking into account the frequency dependence of the blackbody spectrum, one does a similar replacement as in Eq. (A.7) for the light shift and integrates Eq. (A.5), Eq. (A.6) over all frequencies of the blackbody spectrum given by Eq. (7.15). In [139] some analytical expressions are given for limiting cases of the integral, but in general the integration has to be done numerically. The result obtained in [138] is  $\Delta\alpha_S^{BB} = -5.1 \times 10^{-40} \text{ Jm}^2/\text{V}^2$ , which is somewhat larger than the value calculated for the static case  $\Delta\alpha_S = -4.4 \times 10^{-40} \text{ Jm}^2/\text{V}^2$ .

# Appendix B

## Calculation of the Quadrupole Shift

The calculation of the quadrupole shift follows the calculations given in [136]. In the following it is assumed that the quadrupole shift is small compared to the Zeeman shift of the investigated atomic transition. The quadrupole shift can then be calculated using perturbation theory from the matrix elements of  $H_Q$  in the same basis of states  $|\gamma J F m\rangle$  that diagonalizes the Zeeman Hamiltonian. The Hamiltonian for the quadrupole shift is

$$H_Q = \nabla \mathbf{E}^{(2)} \cdot \Theta^{(2)} = \sum_{q=-2}^2 (-1)^q \nabla E_q^{(2)} \Theta_{-q}^{(2)}. \quad (\text{B.1})$$

The tensor components  $\nabla E_q^{(2)}$  of the electric field gradient are defined as

$$\begin{aligned} \nabla E_0^{(2)} &= -\frac{1}{2} \frac{\partial E}{\partial z}, \\ \nabla E_{\pm 1}^{(2)} &= \pm \frac{1}{\sqrt{6}} \frac{\partial E_{\pm}}{\partial z} = \pm \frac{1}{\sqrt{6}} \partial_{\pm} E_z, \\ \nabla E_{\pm 2}^{(2)} &= \pm -\frac{1}{2\sqrt{6}} \partial_{\pm} E_{\pm}. \end{aligned} \quad (\text{B.2})$$

The components  $\Theta_q^{(2)}$  of the quadrupole operator are

$$\begin{aligned} \Theta_0^{(2)} &= -\frac{e}{2} \sum_j (3z_j - r_j^2), \\ \Theta_{\pm 1}^{(2)} &= -e \sqrt{\frac{3}{2}} \sum_j z_j (x_j \pm iy_j), \\ \Theta_{\pm 2}^{(2)} &= -e \sqrt{\frac{3}{8}} \sum_j (x_j \pm iy_j)^2. \end{aligned} \quad (\text{B.3})$$



The sums are taken over all electrons. In the principal axis frame denoted  $\{x', y', z'\}$ ,  $H_Q$  takes the simple form

$$H_Q = -2A\Theta_0^{(2)'} + \sqrt{\frac{2}{3}}\epsilon A \left( \Theta_2^{(2)'} + \Theta_{-2}^{(2)'} \right). \quad (\text{B.4})$$

The atomic states in the laboratory frame of reference  $|\gamma JF\mu\rangle$  where the  $z$ -axis is along the magnetic field are related to the ones in the principal axis frame  $|\gamma JFm\rangle'$  by rotation matrix elements  $D_{\mu m}^{(F)}(\boldsymbol{\omega})$  in the following way:

$$|\gamma JF\mu\rangle = \sum_m D_{\mu m}^{(F)*}(\boldsymbol{\omega}) |\gamma JFm\rangle', \quad (\text{B.5})$$

where  $\boldsymbol{\omega} = \{\alpha, \beta, \gamma\}$  denotes the set of Euler angles that relates the principal axis frame to the laboratory frame. Since the final rotation is about the laboratory  $z$ -axis, which is parallel to the magnetic field and therefore a symmetry axis, one can set  $\gamma = 0$ . Generalizing the result from [136] one finds for the matrix elements of  $H_Q$ :

$$\langle \gamma JF\mu' | H_Q | \gamma JF\mu \rangle = (-1)^{F-\mu} \begin{pmatrix} F & F & 2 \\ \mu' & -\mu & \mu - \mu' \end{pmatrix} (\gamma JF || \Theta^{(2)} || \gamma JF) A G_{\mu\mu'}(\boldsymbol{\omega}), \quad (\text{B.6})$$

with

$$G_{\mu\mu'}(\boldsymbol{\omega}) = \epsilon \sqrt{\frac{2}{3}} \left( D_{(\mu-\mu')-2}^{(2)*}(\boldsymbol{\omega}) + D_{(\mu-\mu')+2}^{(2)*}(\boldsymbol{\omega}) \right) - 2 D_{(\mu-\mu')0}^{(2)*}(\boldsymbol{\omega}). \quad (\text{B.7})$$

The reduced matrix element is in the  $(IJ)$  coupling approximation

$$(\gamma IJF || \Theta^{(2)} || \gamma IJF) = (-1)^{I+J+F} (2F+1) \begin{Bmatrix} J & 2 & J \\ F & I & F \end{Bmatrix} \begin{pmatrix} J & 2 & J \\ -J & 0 & J \end{pmatrix}^{-1} \Theta(\gamma, J). \quad (\text{B.8})$$

$\Theta(\gamma, J)$  is the quadrupole moment of the  $(\gamma, J)$  state, which is defined as

$$\Theta(\gamma, J) = \langle \gamma J J | \Theta_0^{(2)} | \gamma J J \rangle. \quad (\text{B.9})$$

The definition used here is the same as in [136, 155], which is commonly used for molecular quadrupole moments. This differs from the definition given in [157] by a factor of  $-\frac{1}{2}$  and from the one usually found in the literature for nuclear quadrupole moments by a factor  $-\frac{1}{2}e$  [124]. If configuration mixing in the  $(\gamma, J)$  state can be neglected, the quadrupole moment can be expressed as

$$\Theta(\gamma, J) = -\frac{q}{2} \cdot \frac{2J-1}{2J+2} \langle \gamma | r^2 | \gamma \rangle, \quad (\text{B.10})$$

where  $q$  is equal to  $-e$  for an electron and  $+e$  for a hole in a nearly completely filled electron shell. The relevant rotation matrix elements

$$\begin{aligned} D_{00}^{(2)*} &= \frac{1}{2} (3 \cos^2 \beta - 1) = \sqrt{\frac{4\pi}{5}} Y_{20}^*, \\ D_{1\pm 0}^{(2)*} &= \mp \sqrt{\frac{3}{2}} \sin \beta \cos \beta e^{\mp i\alpha} = \sqrt{\frac{4\pi}{5}} Y_{2\pm 1}^*, \\ D_{0\pm 2}^{(2)*} &= \sqrt{\frac{3}{8}} \sin^2 \beta e^{\mp i2\alpha} = \sqrt{\frac{4\pi}{5}} Y_{2\pm 2}^*, \end{aligned} \quad (\text{B.11})$$

are related to the spherical harmonics  $Y_{2m}$  for  $l = 2$ . From the matrix elements in Eq. (B.6) one finds for the first- and second-order quadrupole shift:

$$\begin{aligned} h \cdot \Delta\nu_Q^{(1)} &= \langle \gamma J F m | H_Q | \gamma J F m \rangle \\ &= \frac{-2A[3m^2 - F(F+1)](\gamma J F || \Theta^{(2)} || \gamma J F)}{\sqrt{(2F+3)(2F+2)(2F+1)2F(2F-1)}} (3 \cos^2 \beta - 1 - \epsilon \sin^2 \beta \cos 2\alpha) \end{aligned} \quad (\text{B.12})$$

$$\begin{aligned} h \cdot \Delta\nu_Q^{(2)} &= \sum_{n \neq m} \frac{|\langle \gamma J F n | H_Q | \gamma J F m \rangle|^2}{E_m - E_n} \\ &= \frac{1}{\Delta E_Z} \sum_{n \neq m} \frac{A^2 |\langle \gamma J F || \Theta^{(2)} || \gamma J F \rangle|^2}{m-n} \begin{pmatrix} F & F & 2 \\ n & -m & m-n \end{pmatrix} |G_{mn}(\boldsymbol{\omega})|^2 \end{aligned} \quad (\text{B.13})$$

where  $\Delta E_Z$  is the energy difference between adjacent Zeeman sublevels. For the potential generated by the Paul traps used in the experiments,  $\epsilon \simeq 0$  in Eq. (B.7). The second-order expression Eq. (B.13) then reduces to

$$\begin{aligned} h \cdot \Delta\nu_Q^{(2)} &\simeq \frac{12A^2 m |\langle \gamma J F || \Theta^{(2)} || \gamma J F \rangle|^2}{\Delta E_Z} \times \\ &\frac{|D_{1\pm 0}^{(2)*}|^2 (8m^2 + 1 - 4F(F+1)) + |D_{0\pm 2}^{(2)*}|^2 (-2m^2 - 1 + 2F(F+1))}{F(F+1)(2F-1)(2F+1)(2F+3)} \end{aligned} \quad (\text{B.14})$$

# Bibliography

- [1] Abbreviated translation of a passage in Plato's *Timaios*, ~360 B.C.
- [2] Translation of "*Zeit ist das, was man an der Uhr abliest*", attributed to A. Einstein.
- [3] D. N. Adams. *The Hitchhiker's Guide to the Galaxy*. Pan Books Ltd., London (1979).
- [4] Translation of "*Quid est ergo tempus? Si nemo ex me quaerat, scio; si quaerenti explicare velim, nescio*", Aurelius Augustinus, *Confessiones* XI, 14.
- [5] R. F. C. Vessot and M. W. Levine. *J. Gen. Rel. Grav.* **10**, 181 (1979).
- [6] R. F. C. Vessot et al. *Phys. Rev. Lett.* **45**, 2081 (1980).
- [7] A. Godone, C. Novero, and P. Tavella. *Phys. Rev. D* **51**, 319 (1995).
- [8] C. Braxmeier, H. Müller, O. Prادل, J. Mlynek, A. Peters, and S. Schiller. *Phys. Rev. Lett.* **88**, 010401 (2002).
- [9] A. Bauch and S. Weyers. *Phys. Rev. D* **65**, 081101(R) (2002).
- [10] C. Audoin and B. Guinot. *The Measurement of Time and Frequency*. Cambridge University Press, Cambridge (2001).
- [11] M. Niering et al. *Phys. Rev. Lett.* **84**, 5496 (2000).
- [12] J. P. Uzan. *Rev. Mod. Phys.* **75**, 403 (1990).
- [13] J. D. Barrow. *Astrophys. Space Sci.* **283**, 645 (2003).
- [14] S. G. Karshenboim and E. Peik, editors. *Astrophysics, Clocks and Fundamental Constants*. Springer, Heidelberg (2004).
- [15] A. Scheibe and U. Adelsberger. *Physikalische Zeitschrift* **37**(6), 38 (1936).

- [16] A. Scheibe and U. Adelsberger. *Physikalische Zeitschrift* **37**(6), 185 (1936).
- [17] A. Scheibe. *Zeitschrift für angewandte Physik* **V**(8), 307 (1953).
- [18] *Address to the Mathematical and Physical Sections of the British Association*, volume XL of *British Association Report*.
- [19] *Comptes rendus de la treizième Conférence Générale des Poids et Mesures*. Gauthier-Villars, Paris (1968).
- [20] T. P. Heavner, S. R. Jefferts, E. A. Donley, J. H. Shirley, and T. E. Parker. *IEEE Trans. Instrum. Meas.* **54**, 842 (2005).
- [21] S. Bize et al. *C. R. Physique* **5**, 829 (2004).
- [22] W. Paul, O. Osberghaus, and E. Fischer. *Ein Ionenkäfig*. Forschungsbericht Bd. 415, Wirtschafts- und Verkehrsministerium Nordrhein-Westfalen, Köln (1958).
- [23] H. Dehmelt. *Bull. Am. Phys. Soc.* **20**, 60 (1975).
- [24] H. Dehmelt. *IEEE Trans. Instrum. Meas.* **31**, 83 (1982).
- [25] W. Neuhauser, M. Hohenstatt, P. Toschek, and H. Dehmelt. *Phys. Rev. Lett.* **41**, 233 (1978).
- [26] W. Neuhauser, M. Hohenstatt, P. Toschek, and H. Dehmelt. *Phys. Rev. A* **22**, 1137 (1978).
- [27] D. J. Wineland and H. Dehmelt. *Bull. Am. Phys. Soc.* **20**, 637 (1975).
- [28] T. W. Hänsch and A. L. Schalow. *Opt. Comm.* **13**, 68 (1975).
- [29] E. Fischer. *Z. Physik* **156**, 1 (1959).
- [30] D. Leibfried et al. *Nature* **422**, 412 (2003).
- [31] F. Schmidt-Kaler et al. *Nature* **422**, 408 (2003).
- [32] B. B. Blinov, D. L. Moehring, L. M. Duan, and C. Monroe. *Nature* **428**, 153 (2004).
- [33] C. Monroe. *Nature* **416**, 238 (2002).
- [34] M. D. Barrett et al. *Nature* **429**, 737 (2004).
- [35] M. Riebe et al. *Nature* **429**, 734 (2004).
- [36] H. Dehmelt. *Bull. Am. Phys. Soc.* **18**, 1521 (1973).

- [37] P. Gill, editor. *Proceedings of the 6<sup>th</sup> Symposium on Frequency Standards and Metrology*. World Scientific, Singapore (2002).
- [38] A. A. Madej and J. E. Bernard. In *Frequency Measurement and Control, Topics in Applied Physics*, A. Luiten, editor, volume 79, p. 149. Springer, Berlin (2000).
- [39] J. Reichert, M. Niering, R. Holtzwarth, M. Weitz, Th. Udem, and T. W. Hänsch. *Phys. Rev. Lett.* **84**, 3232 (1999).
- [40] Th. Udem, R. Holtzwarth, and T. W. Hänsch. *Nature* **416**, 233 (2002).
- [41] S. Bize et al. *Phys. Rev. Lett.* **90**, 150802 (2003).
- [42] Th. Becker et al. *Phys. Rev. A* **63**, 051802 (2001).
- [43] G. P. Barwood, H. S. Margolis, G. Huang, P. Gill, and H. A. Klein. *Phys. Rev. Lett.* **93**, 133001 (2004).
- [44] P. Blythe et al. *Phys. Rev. A* **67**, 020501 (2003).
- [45] Chr. Tamm, T. Schneider, and E. Peik. In *Laser Spectroscopy*, volume XVI, p. 40. World Scientific (2004).
- [46] A. A. Madej, J. E. Bernard, P. Dubé, and L. Marmet. *Phys. Rev. A* **70**, 012507 (2004).
- [47] H. S. Margolis et al. *Science* **306**, 1355 (2004).
- [48] W. H. Oskay et al. In *Book of Abstracts of the 19<sup>th</sup> European Frequency and Time Forum*, p. 72 (2005).
- [49] Th. Udem et al. *Phys. Rev. Lett.* **86**, 4996 (2001).
- [50] H. Marion et al. *Phys. Rev. Lett.* **90**, 150801 (2003).
- [51] J. Stenger, Chr. Tamm, N. Haverkamp, S. Weyers, and H. R. Telle. *Opt. Lett.* **26**, 1589 (2001).
- [52] H. Schnatz, B. Lipphardt, C. Degenhardt, Ekkehard Peik, T. Schneider, U. Sterr, and Chr. Tamm. *IEEE Trans. Instrum. Meas.* **54**, 750 (2005).
- [53] M. Fischer et al. *Phys. Rev. Lett.* **92**, 230802 (2004).
- [54] E. Peik, B. Lipphardt, H. Schnatz, T. Schneider, Chr. Tamm, and S. G. Karshenboim. *Phys. Rev. Lett.* **93**, 170801 (2004).
- [55] J. Vanier and C. Audoin. *The Quantum Physics of Atomic Frequency Standards*. Hilger, Bristol (1989).

- [56] F. G. Major. *The Quantum Beat: The Physical Principles of Atomic Clocks*. Springer, New York (1998).
- [57] A. Bauch and H. R. Telle. *Rep. Prog. Phys.* **65**, 789 (2002).
- [58] T. Jones. *Splitting the Second: The Story of Atomic Time*. IOP Publishing, Bristol (2000).
- [59] G. D. van Rossum. *History of the Hour*. The University of Chicago Press, Chicago (1996).
- [60] R. A. Nelson, D. D. McCarthy, S. Malys, J. Levine, B. Guinot, H. F. Fliegel, R. L. Beard, and T. R. Bartholomew. *Metrologia* **38**, 509 (2001).
- [61] D. W. Allan. *Proc. IEEE* **54**, 221 (1966).
- [62] J. A. Barnes et al. *IEEE Trans. Instrum. Meas.* **20**, 105 (1971).
- [63] Chr. Tamm, D. Engelke, and V. Bühner. *Phys. Rev. A* **61**, 053405 (2000).
- [64] W. H. Oskay, W. M. Itano, and J. C. Bergquist. *Phys. Rev. Lett.* **94**, 163001 (2005).
- [65] R. J. Rafac, B. C. Young, J. A. Beall, W. M. Itano, and J. C. Bergquist. *Phys. Rev. Lett.* **85**, 2462 (2000).
- [66] W. Nagourney, N. Yu, and H. Dehmelt. *Opt. Comm.* **79**, 176 (1990).
- [67] N. Yu, X. Zhao, H. Dehmelt, and W. Nagourney. *Phys. Rev. A* **50**, 2738 (1994).
- [68] N. Yu, W. Nagourney, and H. Dehmelt. *Phys. Rev. Lett.* **78**, 4898 (1997).
- [69] M. Knoop, C. Champenois, G. Hagel, M. Houssin, C. Lisowski, and F. Vedel. *Eur. Phys. J. D* **29**, 163 (2004).
- [70] A. Kreuter et al. *Phys. Rev. A* **71**, 032504 (2005).
- [71] D. J. Wineland et al. In *Proceedings of the 2003 IEEE International Frequency Control Symposium and PDA Exhibition Jointly with the 17<sup>th</sup> European Frequency and Time Forum*, p. 68 (2004).
- [72] G. Wilpers, T. Binnewies, C. Degenhardt, U. Sterr, J. Helmke, and F. Riehle. *Phys. Rev. Lett.* **89**, 230801 (2002).
- [73] C. Oates, E. Curtis, and L. Hollberg. *Opt. Lett.* **25**, 1603 (2000).
- [74] T. Mehlstäubler, J. Keupp, A. Douillet, N. Rehbein, E. M. Rasel, and W. Ertmer. *J. Opt. B* **5**, 183 (2003).

- [75] H. Katori. In *Proceedings of the 6<sup>th</sup> Symposium on Frequency Standards and Metrology*, P. Gill, editor, p. 323. World Scientific, Singapore (2002).
- [76] H. Katori and M. Takamoto. *Phys. Rev. Lett.* **91**, 173005 (2003).
- [77] T. Ido and H. Katori. *Phys. Rev. Lett.* **91**, 053001 (2003).
- [78] M. Takamoto and H. Katori. *Phys. Rev. Lett.* **91**, 223001 (2003).
- [79] I. Courtillot et al. *Phys. Rev. A* **68**, 030501(R) (2003).
- [80] G. Ferrari et al. *Phys. Rev. Lett.* **91**, 243002 (2003).
- [81] T. Ido et al. *Phys. Rev. Lett.* **94**, 153001 (2005).
- [82] S. G. Parsev, A. Derevianko, and E. N. Fortson. *Phys. Rev. A* **69**, 021403(R) (2004).
- [83] R. G. Helmer and C. W. Reich. *Phys. Rev. C* **49**, 1845 (1994).
- [84] E. Peik and Chr. Tamm. *Europhys. Lett.* **61**, 181 (2003).
- [85] S. B. Utter et al. *Phys. Rev. Lett.* **82**, 505 (1999).
- [86] R. W. Shaw, J. P. Young, S. P. Cooper, and O. F. Webb. *Phys. Rev. Lett.* **82**, 1109 (1999).
- [87] V. V. Koltsov, T. E. Kuzmina, and D. N. Suglobov. In *49<sup>th</sup> Annual Conference on Nuclear Spectroscopy and Structure of Atomic Nuclei*, Yu. Oganessian and R. Kalpakceva, editors, p. 93. World Scientific, Singapore (1999).
- [88] E. Browne et al. *Phys. Rev. C* **64**, 014311 (2001).
- [89] C. R. Pollock, D. A. Jennings, F. R. Peterson, R. E. Drullinger, E. C. Beaty, and K. M. Evenson. *Opt. Lett.* **8**, 133 (1982).
- [90] H. Schnatz, B. Lipphardt, J. Helmcke, F. Riehle, and G. Zinner. *Phys. Rev. Lett.* **76**, 18 (1996).
- [91] J. Stenger, H. Schnatz, Chr. Tamm, and H. R. Telle. *Phys. Rev. Lett.* **88**, 073601 (2002).
- [92] P. Kubina et al. *Opt. Exp.* **13**, 904 (2005).
- [93] W. Paul. *Rev. Mod. Phys.* **62**(3), 531 (1990).
- [94] J. Meixner and F. W. Schäfke. *Mathieusche Funktionen und Sphäroidfunktionen*. Springer, Heidelberg (1954).

- [95] D. J. Bate, K. Dholakia, R. C. Thompson, and D. C. Wilson. *J. Mod. Opt.* **39**, 305 (1992).
- [96] P. Taylor. *Observation of an Ultra-High Q Resonance in a Single Ion of  $^{172}\text{Yb}^+$* . PhD thesis, University of Oxford (1996).
- [97] M. Roberts. *Spectroscopy of a Single Ytterbium Ion*. PhD thesis, Imperial College, University of London (1997).
- [98] Chr. Tamm, D. Schnier, and A. Bauch. *Appl. Phys. B* **60**, 19 (1995).
- [99] E. H. Pinnington, G. Rieger, and J. A. Kernahan. *Phys. Rev. A* **56**, 2421 (1997).
- [100] A. M. Mårtensson-Pendril, D. S. Gough, and P. Hannaford. *Phys. Rev. A* **49**, 3351 (1994).
- [101] Ch. Gerz, J. Roths, F. Vedel, and G. Werth. *Z. Phys. D* **8**, 235 (198).
- [102] D. Engelke. *Untersuchungen am 435 nm Quadrupol-Übergang eines Ytterbium-Ions*. PhD thesis, University of Hannover (1998). PTB Bericht PTB-Opt-57.
- [103] M. Roberts, P. Taylor, S. V. Gateva-Kostova, R. B. M. Clarke, W. R. C. Rowley, and P. Gill. *Phys. Rev. A* **60**, 2867 (1999).
- [104] M. Roberts, P. Taylor, G. P. Barwood, P. Gill, H. A. Klein, and W. R. C. Rowley. *Phys. Rev. Lett.* **78**, 1876 (1997).
- [105] S. A. Webster, P. J. Blythe, K. Hosaka, G. P. Barwood, and P. Gill. *Systematic shifts of the 467 nm electric octupole transition in  $^{171}\text{Yb}^+$* . NPL Report CBTLM 31, National Physics Laboratory, Teddington, Middlesex, UK (2004).
- [106] P. T. H. Fisk. *Rep. Prog. Phys.* **60**, 761 (1997).
- [107] S. Stenholm. *Rev. Mod. Phys.* **58**(3), 699 (1986).
- [108] D. J. Wineland and W. M. Itano. *Phys. Rev. A* **20**, 1521 (1979).
- [109] J. I. Cirac, R. Blatt, P. Zoller, and W. D. Phillips. *Phys. Rev. A* **46**, 2668 (1992).
- [110] V. Bühner. *Schmale Strukturen in der Resonanzfluoreszenz eines gespeicherten Atoms*. PhD thesis, University of Hannover (2001). PTB Bericht PTB-Opt-63.



- [111] D. J. Berkeland, J. D. Miller, J. C. Bergquist, W. M. Itano, and D. J. Wineland. *J. Appl. Phys* **83**, 5025 (1998).
- [112] F. Diedrich and H. Walther. *Phys. Rev. Lett.* **58**, 203 (1987).
- [113] E. Peik, J. Abel, Th. Becker, J. v. Zanthier, and H. Walther. *Phys. Rev. A* **60**, 439 (1999).
- [114] Chr. Tamm. Private communication.
- [115] E. C. Beaty. *J. Appl. Phys* **61**, 2118 (1987).
- [116] E. C. Beaty. *Phys. Rev. A* **33**, 3645 (1985).
- [117] N. Kjaergaard, L. Hornkaer, A. M. Thommesen, Z. Videsen, and M. Drewsen. *Appl. Phys. B* **71**, 207 (2000).
- [118] S. Gulde, D. Rotter, P. Barton, F. Schmidt-Kaler, R. Blatt, and W. Hoyer-vorst. *Appl. Phys. B* **73**, 861 (2001).
- [119] Ch. Schwedes. *Experimente zur Realisierung eines optischen Frequenznormals auf der Basis eines einzelnen Indium-Ions*. PhD thesis, Ludwig-Maximilians-University, Munich (2004).
- [120] M. Keller. *Quantenoptik mit gespeicherten  $^{40}\text{Ca}^+$ -Ionen*. PhD thesis, Ludwig-Maximilians-University, Munich (2004).
- [121] Chr. Tamm. *Appl. Phys. B* **56**, 295 (1993).
- [122] N. F. Ramsey. *Rev. Mod. Phys.* **62**(3), 541 (1990).
- [123] W. Itano et al. *Phys. Rev. A* **47**, 3554 (1992).
- [124] I. I. Sobel'man. *Introduction to the Theory of Atomic Spectra*. Pergamon Press Ltd., Oxford (1972).
- [125] E. Peik, T. Schneider, and Chr. Tamm. To be published.
- [126] S. A. Diddams, J. C. Bergquist, S. R. Jefferts, and C. W. Oates. *Science* **306**, 1318 (2004).
- [127] E. Riis and A. G. Sinclair. *J. Phys. B* **37**, 4719 (2004).
- [128] C. Champenois et al. *Phys. Lett. A* **331**, 298 (2004).
- [129] G. J. Dick. *Proceedings of the 19<sup>th</sup> Annual PTTI Applications and Planning Meeting*, p. 133 (1987).

- [130] C. Audoin, G. Santarelli, Ala'a Makdissi, and André Clairon. *IEEE Trans. Ultrason., Ferroelect., Freq. Contr.* **45**, 877 (1998).
- [131] G. Santarelli, C. Audoin, Ala'a Makdissi, Ph. Laurent, G. J. Dick, and André Clairon. *IEEE Trans. Ultrason., Ferroelect., Freq. Contr.* **45**, 887 (1998).
- [132] Ch. A. Greenhall. *IEEE Trans. Ultrason., Ferroelect., Freq. Contr.* **45**, 895 (1998).
- [133] B. C. Young, F. C. Cruz, W. M. Itano, and J. C. Bergquist. *Phys. Rev. Lett.* **82**, 3799 (1999).
- [134] B. C. Fawcett and A. Wilson. *Atomic Data And Nuclear Data Tables* **47**(4), 241 (1991).
- [135] J. R. P. Angel and P. G. H. Sandars. *Proc. Roy. Soc. A* **305**, 125 (1967).
- [136] W. Itano. *J. Res. Natl. Inst. Stand. Technol.* **105**, 829 (2000).
- [137] Z. S. Li, S. Svanberg, P. Quinet, X. Tordoir, and E. Biémont. *J. Phys. B* **32**, 1731 (1999).
- [138] R. B. Warrington. Private communication.
- [139] J. W. Farley and W. H. Wing. *Phys. Rev. A* **23**, 2397 (1981).
- [140] C. Cohen-Tanonoudji, J. Dupont-Roc, and G. Grynberg. *Atom-Photon Interactions*. John Wiley & Sons, New York (1992).
- [141] M. H. Cohen and F. Reif. In *Solid State Physics*, F. Seitz and D. Turnbull, editors, volume 5, p. 321. Academic Press Inc., New York (1957).
- [142] C. A. Schrama, E. Peik, W. W. Smith, and H. Walther. *Opt. Comm.* **101**, 32 (2001).
- [143] P. Dubé et al. To be published.
- [144] M. van Camp, T. Camelbeeck, and P. Richard. *Physicalia Magazine* **25**(3), 161 (2003).
- [145] N. Allard and J. Kielkopf. *Rev. Mod. Phys.* **54**, 1103 (1982).
- [146] W. Jhe. *Phys. Rev. A* **43**, 5795 (1990).
- [147] E. A. Hinds and V. Sandoghdar. *Phys. Rev. A* **43**, 398 (1990).
- [148] W. J. Marciano. *Phys. Rev. Lett.* **52**, 489 (1984).

- 
- [149] X. Calmet and H. Fritzsch. *Eur. Phys. J. C* **24**, 639 (2002).
- [150] P. Langacker, G. Segre, and M. J. Strassler. *Phys. Lett. B* **528**, 121 (2002).
- [151] M. T. Murphy, J. K. Webb, and V. V. Flambaum. *Mon. Not. R. Astron. Soc.* **345**, 609 (2001).
- [152] R. Srianand, H. Chand, P. Petitjean, and B. Aracil. *Phys. Rev. Lett.* **92**, 121302 (2004).
- [153] V. A. Dzuba, V. V. Flambaum, and J. K. Webb. *Phys. Rev. A* **59**, 230 (1999).
- [154] V. A. Dzuba, V. V. Flambaum, and M. V. Marchenko. *Phys. Rev. A* **68**, 022506 (2003).
- [155] J. R. P. Angel, P. G. H. Sandars, and G. K. Woodgate. *J. Chem. Phys.* **47**(4), 1552 (1967).
- [156] E. H. Pinnington, R. W. Berends, and Q. Ji. *Phys. Rev. A* **50**, 2758 (1994).
- [157] L. D. Landau and E. M. Lifschitz. *Lehrbuch der theoretischen Physik Band III: Quantenmechanik*. Akademie-Verlag, Berlin, 2nd edition (1966).

# Acknowledgements

The work on this project would not have been as enjoyable or successful as it was without many people that were involved in this work in academic and not so academic ways.

First of all I want to thank my supervisors Ekkehard Peik and Christian Tamm for giving me the opportunity to work on this exciting project and their always friendly and competent help and advice.

I thank Andreas Bauch, Dirk Piester, Stefan Weyers and Robert Wynands, who always had the time for questions and discussion not only about time.

Dieter Griebisch and Thomas Leder I want to thank for the always faultless mechanical construction work they provided for the experiment and for often being helpful in finding the technical solution to a physics problem.

The good atmosphere at the Kopfermann Bau at PTB made the work on the project all the more an enjoyable experience for which I am grateful also to Rolf Augustin, Martina Bäumlner, Jürgen Becker, Günter Neujahr, Thomas Polewka, Christof Richter and Roland Schröder. They not only cordially welcomed a foreigner from bavaria but were also always ready to help with any kind of problem.

Bruce Warrington has contributed significantly to the calculations of the black-body AC Stark shift and the electric polarizabilities and it was a great pleasure to work with him.

Finally I thank the Physikalisch-Technische Bundesanstalt and the Sonderforschungsbereich 407 for funding.

# List of Publications

## Articles in Refereed Journals

1. *Limit on the Present Temporal Variation of the Fine Structure Constant*  
E. Peik, B. Lipphardt, H. Schnatz, T. Schneider, Chr. Tamm, S. G. Karshenboim,  
Phys. Rev. Lett. **93**, 170801 (2004)
2. *Optical Frequency Measurements Using fs-Comb Generators*  
H. Schnatz, B. Lipphardt, C. Degenhardt, E. Peik, T. Schneider, U. Sterr, Chr.  
Tamm,  
IEEE Trans. Instrum. Meas. **54**, 750 (2005)
3. *Sub-hertz Optical Frequency Comparisons Between Two Trapped  $^{171}\text{Yb}^+$  Ions*  
T. Schneider, E. Peik, Chr. Tamm,  
Phys. Rev. Lett. **94**, 230801 (2005)

## Conference Proceedings

1. *Spectroscopy and Precision Frequency Measurement of the 435.5 nm Clock Transition of  $^{171}\text{Yb}^+$*   
Chr. Tamm, T. Schneider, E. Peik  
In: Proceedings of the 6. Symposium on Frequency Standards and Metrology,  
Ed.: P. Gill, World Scientific, Singapore 2002, p. 369-375
2. *Comparison of Two Single-Ion Optical Frequency Standards at the Hertz Level*  
T. Schneider, Chr. Tamm, E. Peik  
In: Proceedings of the 2003 IEEE Int. Frequency Control Symposium and the  
17th European Frequency and Time Forum, Ed.: J. R. Vig, IEEE 2003
3. *Comparison of Two Single-Ion Optical Frequency Standards at the Sub-Hertz Level*  
Chr. Tamm, T. Schneider, E. Peik  
In: Laser Spectroscopy XVI, Eds.: P. Hannaford, A. Sidorov, H. Bachor, K. Baldwin,  
World Scientific, Singapore 2004, p. 40-48  
arXiv: physics/0402120
4. *Trapped Ion Optical Frequency Standards for Laboratory Tests of Alpha-Variability*  
Chr. Tamm, T. Schneider, E. Peik  
In: Astrophysics, Clocks and Fundamental Constants, Lecture Notes in Physics  
Vol. 648, Eds.: S. G. Karshenboim, E. Peik, (Springer, Heidelberg, 2004), p.  
247-261.
5. *New Limit on the Present Temporal Variation of the Fine Structure Constant*  
E. Peik, B. Lipphardt, H. Schnatz, T. Schneider, Chr. Tamm, S. G. Karshenboim,  
In: Atomic Physics 19, Eds.: L. G. Marcassa, V. S. Bagnato, K. Helmerson,  
American Institute of Physics, Melville, 2005, p.103-111

# Curriculum Vitae

5.9.1975	Born in München Pasing as son of Sieglinde and Jakob Schneider
September 1981 - August 1985	Elementary school, Grundschule an der Grandlstrasse in München
September 1985 - July 1994	Grammar school, Louise-Schröder-Gymnasium in München
1.7.1994	Graduation, general qualification for university entrance
November 1994 - August 1995	civilian service at mobiler sozialer Hilfsdienst der Johanniter in Puchheim
November 1995 - January 2000	Physics studies at the Ludwig-Maximilians University in München
January 2000 - January 2001	Diploma thesis at the Max-Planck Institute for Quantum Optics in Garching
13.2.2001	Degree in Physics at the Ludwig-Maximilians University in München
April 2001 - June 2001	Employee of the Max-Planck Institute for Quantum Optics in Garching
1.9.2001	Begin of PhD thesis at the University of Hannover and the Physikalisch-Technische Bundesanstalt Braunschweig
September 2001 - September 2003	Employee of the Physikalisch-Technische Bundesanstalt Braunschweig
Since September 2003	Employee of the University of Hanover in the Sonderforschungsbereich 407